

DISSERTATION

EXPLORING THE IMPACTS OF NANOCONFINEMENT USING NUCLEAR MAGNETIC  
RESONANCE (NMR) SPECTROSCOPY

Submitted by

Samantha L. Miller

Department of Chemistry

In partial fulfillment of the requirements

For the Degree of Doctor of Philosophy

Colorado State University

Fort Collins, Colorado

Summer 2022

Doctoral Committee:

Advisor: Nancy Levinger

Amber Krummel

Debbie Crans

James Graham

Copyright by Samantha Miller 2022

All Rights Reserved

## ABSTRACT

### EXPLORING THE IMPACTS OF NANOCONFINEMENT USING NUCLEAR MAGNETIC RESONANCE (NMR) SPECTROSCOPY

The chemical reactivity of molecules is typically studied under bulk aqueous conditions in the research laboratory. Although this standard may be appropriate for processes destined to be scaled up for industrial purposes, it ignores the fact that a great deal of the chemistry underlying physiological reactions occur in confined environments, like cellular organelles, protein pockets, or porous interfaces.

The dissertation begins by describing the methodology for synthesizing size tunable reverse micelles, or surfactant enveloped nanodroplets. After physical perturbation, the ternary mixture of polar (usually aqueous), nonpolar, and amphiphilic surfactant self-assemble. Two small molecules, glucose and urea, were studied in these nano environments using a combination of analytical techniques including dynamic light scattering, differential scanning calorimetry, and molecular dynamics simulations that complemented the myriad nuclear magnetic resonance (NMR) spectroscopy studies. Quantification of single hydrogen exchange between glucose and water using exchange spectroscopy NMR in conjunction with custom MatLab code revealed that confinement of glucose and water within 8-10 nanometer reverse micelles slows the process of exchange by introducing a quantifiable energy barrier of  $\sim 75$  kJ/mol. Deuterium NMR spectroscopy provided evidence for hydrogen tunneling below 283 K, a surprisingly high temperature for this phenomenon.

The same robust methods of kinetic and structural analysis were used to characterize urea in water reverse micelles. Results showed that in addition to its well-known ability to denature proteins, urea can disrupt amphiphilic membranes and cause a ten-fold increase in the membrane surface area at low temperatures  $\sim 273$  K as a result of this destabilization. Finally, the use of fluorine NMR spectroscopy demonstrated that the reverse micelle nanodroplet environments could achieve higher ionic strengths ( $\sim 9.0$  M) with simple divalent salts than possible in standard bulk solutions ( $\sim 5.0$  M). Together, these results presented compelling evidence that utilization of reverse micelle nanodroplets could provide alternative environments to facilitate previously inaccessible, novel conditions.

## ACKNOWLEDGEMENTS

Thank you to my advisor and mentor, Dr. Nancy Levinger, who has provided me support, guidance, and mentorship throughout the entirety of the past five years. Nancy has been the perfect complement to my needs as a graduate student, and I feel I still have much to learn from her although our work together is coming to a close.

Additionally, I would like to thank each member of my thesis committee for committing time, energy, and expertise to the various steps along my PhD progress.

My friends and colleagues in the chemistry department who provided encouragement, levity, and companionship, especially fellow lab mate Fionna Samuels.

## DEDICATION

In memory of Christina Miller

## TABLE OF CONTENTS

ABSTRACT.....	ii
ACKNOWLEDGEMENTS.....	iv
DEDICATION.....	v
INTRODUCTION.....	1
CHAPTER 1: HYDROGEN EXCHANGE IN GLUCOSE LOADED REVERSE MICELLES...	3
1.1 The Reverse Micelle (RM) System.....	3
1.2 Preparation of Glucose in Reverse Micelles.....	5
1.3 Detection with NMR spectroscopy.....	6
1.3.1 Challenges of NMR spectroscopy.....	10
1.4 Complementary Measurement Techniques.....	12
1.4.1 Size evaluation with Dynamic Light Scattering .....	13
1.4.2 Phase behavior with Differential Scanning Calorimetry.....	14
1.5 The Kinetic Model and Fitting in MatLab .....	15
1.6 Kinetic Exchange Behavior.....	16
1.6.1 Evidence of Hydrogen Tunneling.....	22
1.7 Conclusion.....	27
CHAPTER 2: IMPACT OF UREA ON REVERSE MICELLES.....	29
2.1 Introduction.....	29
2.1.1 Urea in Reverse Micelles.....	30
2.2 Preparation of Urea in Reverse Micelles.....	32

2.3	Detection with NMR spectroscopy.....	33
2.3.1	EXSY pulse sequence description.....	33
2.3.2	2D <sup>1</sup> H-NOESY experiments.....	34
2.4	Observation of temperature-dependent size measurements.....	37
2.5	Kinetic Exchange Behavior.....	39
2.6	Disruption of Typical Surfactant Assembly.....	44
2.7	Conclusions.....	49
CHAPTER 3:	MEASUREING IONIC STRENGTH WITH <sup>19</sup> F-NMR SPECTROSCOPY.....	51
3.1.	Introduction.....	51
3.1.1	Implications of Ionic Headgroups.....	52
3.1.2	Fluorine NMR Spectroscopy.....	53
3.2	Preparation of Reverse Micelle System.....	54
3.2.1	Materials.....	54
3.2.2	Stock Solutions and Sample Preparation.....	54
3.2.3	Reverse Micelle Solutions.....	55
3.2.4	Dynamic Light Scattering (DLS) Experiments.....	55
3.3	Chemical Shift and Correlation with Ionic Strength.....	55
3.4	Behavior of Fluoride Probe in AOT-Reverse Micelle Systems.....	58
3.4.1	<sup>1</sup> H NMR of aqueous ionic solutions .....	61
3.4.2	<sup>19</sup> F NMR of nonionic reverse micelles.....	61
3.4.3	Impact of Ionic Strength on AOT Reverse Micelles.....	62
3.5	Behavior of Fluoride Probe in alternate Reverse Micelle Systems.....	63

3.6 Nanoconfinement's Impact on Ionic strength.....	65
3.6.1 Implications in Colloidal, Fuel Cell and Battery Chemistry.....	66
3.6.2 Implications in Biological Interfaces.....	68
3.7 Conclusions.....	68
CHAPTER 4: CHARACTERIZING NOVEL SURFACTANTS.....	70
4.1 Introduction.....	70
4.2 Ideal Surfactant Characteristics in Cosmetics.....	71
4.2.1 Cleansers.....	71
4.2.2 Emulsifiers.....	72
4.2.3 Solubilizers.....	72
4.2.4 Conditioners.....	72
4.2.5 Other Special Properties.....	72
4.3 Krafft Temperature of Surfactants.....	73
4.4 Characterization of Ceteth-10-Phosphate.....	74
4.5 Preliminary Ceteth-10-Phosphate Results.....	75
4.6 Discussion of Ceteth-10-Phosphate Results .....	84
4.6.1 Solution of 0.01% Ceteth-10-Phosphate Results.....	84
4.6.2 Solution of 0.02% Ceteth-10-Phosphate Results.....	85
4.6.3 Solution of 0.03% Ceteth-10-Phosphate Results.....	85
4.6.4 Summary of Disparate Results.....	86
4.7 Preliminary Dicapylphosphate Results.....	87
4.8 Discussion of Dicapylphosphate Results.....	94

4.8.1 Solution of 0.01% Dicylphosphate Results.....	94
4.8.2 Solution of 0.02% Dicylphosphate Results.....	95
4.9 Conclusions.....	95
CHAPTER 5: CONCLUSIONS.....	96
REFERENCES.....	98
APPENDIX 1: SUPPLEMENTAL INFORMATION- EXCHANGE DYNAMICS OF GLUCOSE IN REVERSE MICELLES.....	118
APPENDIX 2: SUPPLEMENTAL INFORMATION- EXCHANGE DYNAMICS OF UREA IN REVERSE MICELLES.....	129
APPENDIX 3: SUPPLEMENTAL INFORMATION- FLUORIDE PROBES IN REVERSE MICELLES.....	133
APPENDIX 4: CHARACTERIZING NOVEL SURFACTANTS.....	134
APPENDIX 5: GUIDE TO ABBREVIATIONS.....	135

## INTRODUCTION

The chemical reactivity of molecules is typically studied under bulk conditions in the research laboratory. Although this convention is appropriate for processes destined to be scaled up for industrial purposes, it ignores the fact that a great deal of the chemistry underlying biological functions occur in confined environments, like cellular organelles, granular materials, or porous interfaces.

As a polar molecule, water's bulk properties depend on the resultant hydrogen bond network. Hydrogen bonding accounts for a wide range of water's frequently cited "unique" properties, such as its high boiling point and density minimum at 4°C when in the solid phase. Water's omnipresence in life on Earth means it exists amid a variety of conditions. Local changes in salinity, pH, solute concentration, temperature, or pressure will change the behavior of the hydrogen bonding network.<sup>1-3</sup> Yet, current methodologies in literature does not capture the size of water's confined environment in places like organelles, which can be restricted to sizes as small as a couple of nanometers. Published chemical models usually increase concentrations or modify water's polarizability parameter as a way to control for the anticipated confinement effects, but it is crucial that we experimentally grapple with the scale of these intra-organelle spaces. Water's dynamic behavior in bulk systems suggests that confined behavior will necessitate even greater consideration of the structural and chemical perturbations at play.

Funding from the NSF, as well as teaching assistantships granted by the CSU chemistry department, provided the financial feasibility to study osmolytes in confinement while conducting graduate research in the Levinger research group. The study of these low molecular weight compounds whose presence in a solvent, usually water, typically alters expected

properties of the system's constituent fluid.<sup>4</sup> This body of work will summarize and explain the findings from three different osmolytes in nanoconfinement using reverse micelles: glucose, urea, and sodium fluoride. Multiple analytical techniques will be discussed and explained within the subsections of each chapter as they are relevant to the experiments conducted.

Each subsequent chapter, in addition to a chapter dedicated to detailing the findings of an ancillary collaborative project, will narrate how nanosized spaces continue to change the expected chemistry that is otherwise studied in bulk conditions.

## 1.1 The Reverse Micelle (RM) System

This project was initiated after the extensive pioneering work of a previous student, Dr. Benjamin Wiebenga-Sanford. It reflects the work published in the *Journal of Physical Chemistry B*. (Source: Miller S.L., Wiebenga-Sanford B.P., Rithner C.D., Levinger N.E. Nanoconfinement Raises the Energy Barrier to Hydrogen Atom Exchange between Water and Glucose. *J Phys Chem B*. 2021 Apr 8;125(13):3364-3373. doi: 10.1021/acs.jpcc.0c10681. Epub 2021 Mar 30. PMID: 33784460.)

Reverse micelles provide stable and relatively size tunable nano-environments for studying the effects of confinement.<sup>5,6</sup> After physical perturbation, the ternary mixture of polar (usually aqueous), nonpolar, and amphiphilic components self-assemble into droplets wherein the polar heads of the amphiphilic surfactant face inward around the polar droplet (figure 1.1).

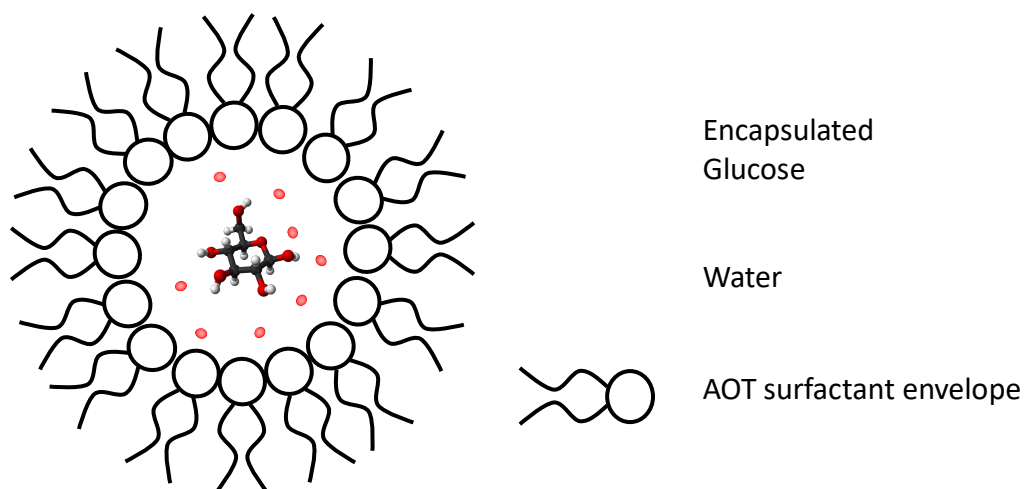


**Figure 1.1.** Illustration of the AOT reverse micelles prepared for studying hydrogen exchange between glucose and water.

In the experiments detailed here, the typical reverse micelle measures from five to twelve nanometers in hydrodynamic diameter. However, typical convention uses  $w_0$ , a unitless parameter to describe the size via the ratio of water to surfactant. This relationship is expressed in EQN 1:

$$w_0 = \frac{[water]}{[surfactant]} \quad (1)$$

Numerous characteristics make reverse micelles ideal as a model system for investigating confined spaces, including their thermodynamic stability over long periods, spontaneous formation, and transparent appearance. When prepared with the surfactant aerosol organic trapper (AOT), the reverse micelle headgroup contains the negatively charged sulfonate group accompanied by the positively charged sodium counter ion. Inexpensive and non-toxic, AOT is the amphiphile used in this study and is the most widely used surfactant when preparing reverse micelles.<sup>6,7,8</sup> AOT has the ideal cone-like geometry, forming reverse micelles with a wide range of non-polar solvents, including alkanes, haloalkanes, and aromatics<sup>5</sup>. Water, the most widely used polar solvent, serves as the polar phase in this study. If substituted with propylene glycol, ethylene glycol, or formamide, a microemulsion system can form as these molecules still exhibit polarity-related properties that are distinct from the non-polar phase. Previous studies have thoroughly characterized the kind of reverse micelles this study employs, that is, those prepared with isooctane, water, and AOT.

Surfactants can also have cationic headgroups like cetyltrimethylammonium bromide (CTAB) but may require an additional co-surfactant to achieve a stable reverse micelle. Non-ionic surfactants that have been employed also include Triton-X and igeal (figure 1.2). Finally, zwitterionic surfactants like phosphatidylcholines are also viable for reverse micelle formation. The geometry of a chosen surfactant plays a significant role in the formation of the reverse micelle

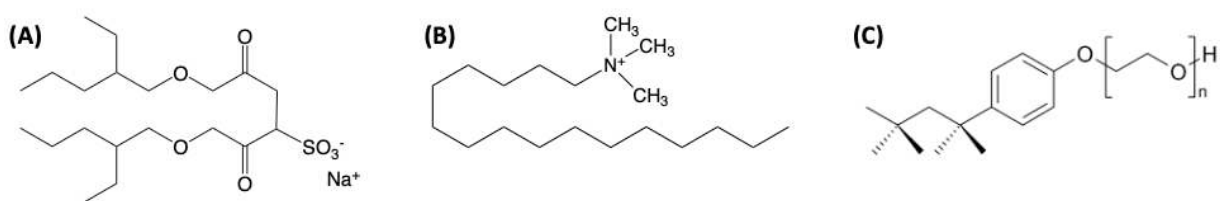


**Figure 1.2.** Chemical structures for various surfactants that may be used in the synthesis of reverse micelles: (A) Aerosol OT (B) Cetyltrimethylammonium (C) Triton X

## 1.2 Preparation of Glucose in Reverse Micelles

Initial efforts to insert glucose into reverse micelles were motivated by a desire to create a crowded sugary environment that mimicked the appropriate conditions for studying glucose-regulated proteins. Discovered in 1977, this class of proteins exist in the lumen of the endoplasmic reticulum<sup>9</sup>. Their known functions include refolding mutant proteins<sup>10</sup>, chaperoning the movement of small peptides, and stabilizing the expression of other proteins<sup>11</sup>. Glucose also mediates the synthesis of other polysaccharides that function as glycans in the cell. These glycans act as chemical markers that mediate cell to cell signaling as well as intracellular maintenance<sup>12,13</sup>. In aqueous solution, glucose exists as both the  $\beta$ -D-glucose anomer and  $\alpha$ -D-

glucose anomer (figure 1.3), though the beta anomer dominates two thirds of the time because of the thermodynamic stability of the equatorially positioned hydroxyl group at the first carbon.

When inserted into the polar core of the RM, glucose retains the ring-closed cyclic form.

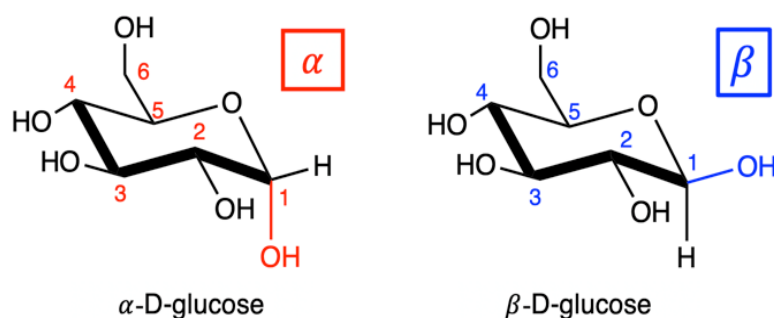


**Figure 1.3:** Chemical structures for the pyranose form of the two glucose anomers present in solution. Numbers refer to both the carbon and hydroxyl group, *e.g.*, hydroxyl group 2 is attached to carbon 2. Carbon 1 is the anomeric carbon, with the colored hydroxyl groups indicating the difference between  $\alpha$  (red) and  $\beta$  (blue) glucose anomers.

Reverse micelles were prepared from 0.1 M AOT stock solutions in isooctane.<sup>14</sup> Solid AOT was added gravimetrically to isooctane to achieve a 0.1 M concentration. Next, water was added to form the reverse micelle nanodroplets. All reverse micelles reported here were prepared to  $w_0=10$ . The reverse micelle solution was sonicated for 45 min. Glucose was loaded to achieve a 30:1 water:glucose mole ratio and further sonicated for 30 min until solid glucose was no longer detected.<sup>14</sup> The overall glucose concentration was 30 mM.

### 1.3 Detection with Nuclear Magnetic Resonance (NMR) spectroscopy

NMR spectroscopy is a highly sensitive method specific to the atomic nuclei within analytes. Nuclei with non-integer spin numbers are compatible for analysis in this technique. In the presence of a strong magnetic field, the excitation of nuclear spins with radio frequency

pulses promotes transitions between energy levels. These transitions and subsequent relaxations generate a free induction decay that can be Fourier transformed into a spectrum whose peak area and chemical shift are indicative of the chemical environment. Commonly used for structure determination, advances in the field have enabled NMR to study reaction kinetics as well through experiments such as exchange spectroscopy (EXSY) NMR. Pairing the EXSY NMR technique to study exchange in glucose loaded reverse micelles was demonstrated by Wiebenga-Sanford *et al.* when they showed that the kinetics of hydrogen exchange were significantly slowed when confined to nanosized reverse micelles (figure 1.4).<sup>14</sup>

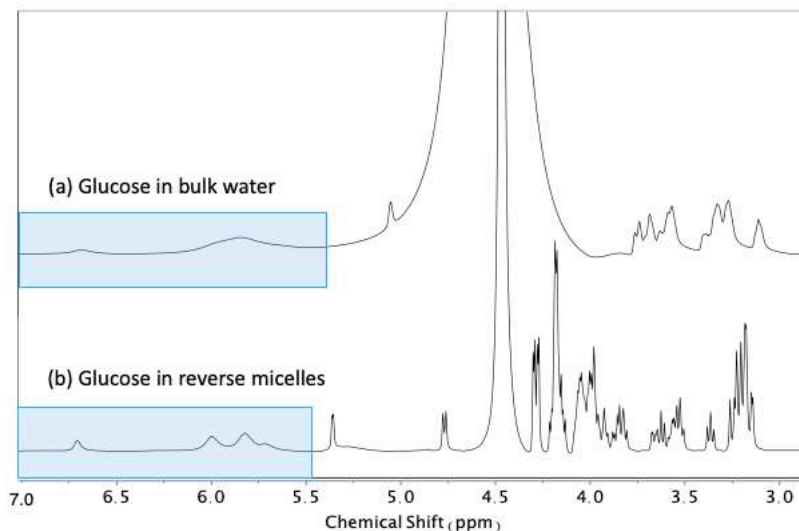


**Figure 1.4.** <sup>1</sup>H-NMR spectra obtained at 298 K of (a) 2 M glucose in bulk water compared to (b) nanoconfined 2 M glucose in a  $\omega_0=10$  reverse micelle with a 30:1 water to glucose ratio.

We use EXSY NMR, sometimes called the zz-exchange experiment,<sup>15</sup> to measure the physical migration of a proton of a hydroxyl group from water to glucose.<sup>14</sup> A cartoon of this exchange process is detailed in figure 1.5. The EXSY NMR experiment is a homonuclear experiment where coherence transfer between nuclear spins occurs through chemical exchange. It uses a pulse sequence identical to a NOESY experiment. We use this NOESY-based EXSY

NMR method<sup>16</sup> whose pulse scheme exploits the effects of magnetization transfer; when one spin generates a local magnetic field, that subsequently perturbs the spin on a nearby atom.<sup>17–19</sup> The EXSY NMR experiment involves physical exchange of excited water protons onto glucose hydroxyls. Pulse widths were set for each experiment to ensure water protons underwent a precise 90° spin flip into the observable xy plane. The hard  $\pi/2$  pulse was 5.6  $\mu\text{s}$ .

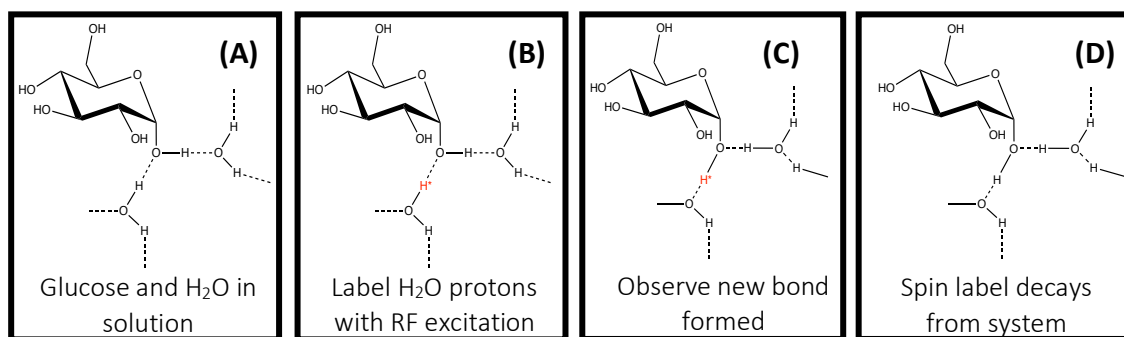


**Figure 1.5.** A chronologically ordered illustration of the exchange process occurring during the EXSY NMR experiment. **(A)** Initially, glucose and water reside in the core of the reverse micelle. **(B)** A radio frequency pulse excites protons on water as indicated by the proton marked with a red asterisk. For simplicity, the illustration highlights only one water proton as labelled. **(C)** A new bond is formed between the labelled proton and glucose during exchange. The former proton bonded to glucose has formed a new bond with another water molecule which is reflected in the growth of the glucose OH peaks downfield. **(D)** Spin decays out of the system as equilibrium is re-established.

NMR spectra, both the standard <sup>1</sup>H and EXSY, were collected using a 500 MHz spectrometer (Agilent Inova) operating at 11.75 T. In preparation for NMR spectra collection, reverse micelle mixtures were mixed with a cyclohexane-*d*<sub>12</sub> lock solvent (2% by volume). Spectra were collected at nine temperatures: 304, 298, 288, 283, 273, 268, 264, 258, and 252 K (31, 25, 15, 10, 0, -5, -9, -15, -21 °C).

Each experiment began with collection of a typical 1D  $^1\text{H}$ -NMR spectrum. Next, the 1D EXSY NMR spectra were collected. The 1D EXSY mixing times (in seconds) were assigned to the following values: 0.0, 0.002, 0.01, 0.05, 0.07, 0.1, 0.2, 0.4, 0.6, 0.8, 1.0, 1.5, 2.0, and 2.5. Because the exchange signal had completely decayed after 2.5 s, mixing times did not exceed this amount. The hard pulse excited hydrogen atoms on water molecules that subsequently exchange onto glucose during the mixing period; this results in the appearance of the glucose hydroxyl peaks. The mixing period, or exchange delay, follows the selective  $\pi$ -pulse that labels a frequency-defined spin across its full width half height frequency. The integrated intensity of the glucose hydroxyl peaks allows us to quantify the exchange rates as they are a direct result of the hydrogen's transition from water to glucose. We repeated this EXSY experiment for each temperature measured. Lowering the temperature changed the chemical shift of the water peak, requiring experimental adjustments to acquire reliable spectra at each temperature. A sample of stacked EXSY NMR plots is provided in figure 1.6. A more detailed description of the experiment as it is set up at the Varian 500 MHz console can be found in Appendix 1.

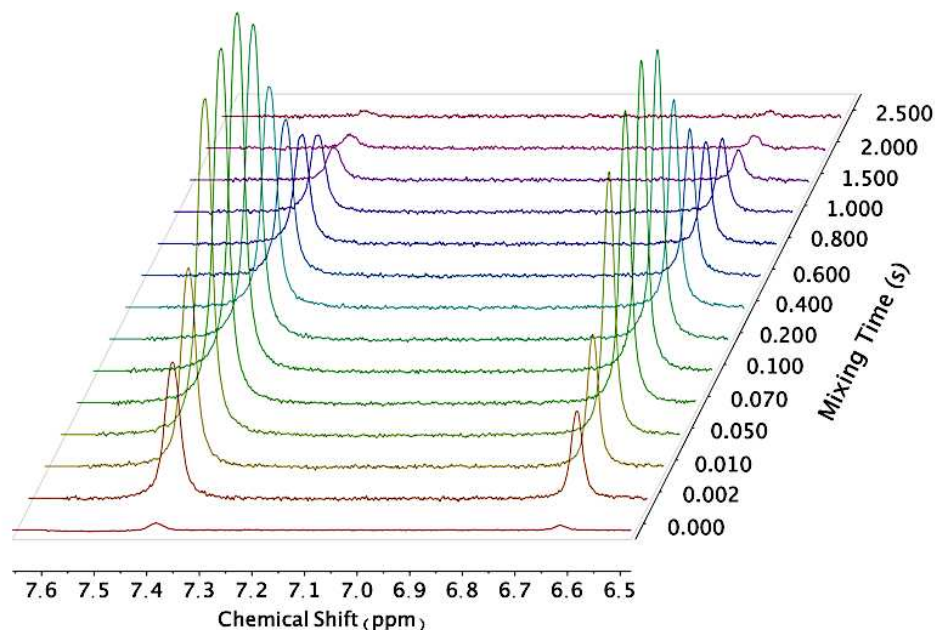


**Figure 1.6:** Stacked EXSY spectra collected at 298 K for glucose loaded AOT reverse micelles. Mixing time is indicated to the right of the spectra. The two peaks correspond to the anomeric hydroxyl hydrogens at the first carbon position for both anomers of glucose. The initial increase in the featured glucose OH peaks represents the swift process of exchange that begins to slow after reaching a maxim exchange rate around 200 ms.

### 1.3.1 Challenges of NMR Spectroscopy

NMR is well suited for the kinetic study of exchange. However, achieving a constant temperature can be challenging as the experiment begins to deviate from ambient room temperatures. Therefore, additional steps were taken to ensure that the digital readout on the console was consistent with the sample temperature within a standard 5 mm glass NMR tube. Temperature settings on the Varian NMR spectrometer's temperature controller were confirmed via methanol thermometer calibration.<sup>20</sup> This well-established calibration method consists of collecting 1D <sup>1</sup>H-NMR spectra to measure the distance,  $\Delta$ , between two peaks. This distance is directly indicative of the temperature in Celsius via EQN 2:

$$T = -23.832\Delta^2 - 29.46\Delta + 403.0 \quad (2)$$

Additionally, to ensure thermal stability of the NMR probe and sample, we equilibrated samples in the NMR spectrometer for 30 min before experiments were performed. A sample spectrum of a standard methanol-d<sub>4</sub> thermometer measurement is shown in figure 1.6. The sample

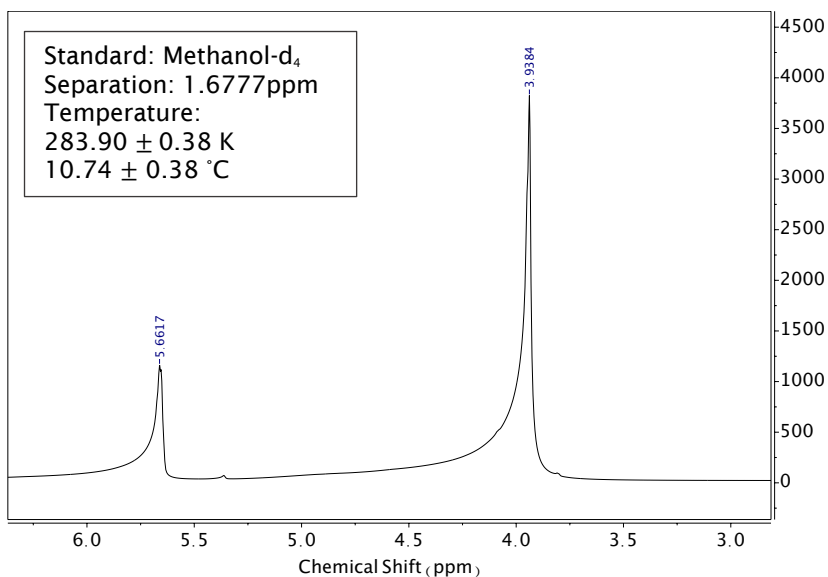


**Figure 1.6:** 1D <sup>1</sup>H-NMR spectrum obtained during methanol thermometer calibration using a 500 MHz Agilent Inova spectrometer operating at 11.75 T. Spectra were analyzed in MNOVA without smoothing functions. Peak picking was used to measure spectral distance and determine the resultant temperature reading as indicated in the text box provided.

The peaks appearing in an NMR spectrum are also temperature sensitive. Higher temperatures result in lower chemical shifts due to the change in magnetic susceptibility. This has important implications in setting up the EXSY NMR measurements which begin with the collection of a <sup>1</sup>H NMR spectrum to determine the frequency of the water peak for excitation during the EXSY pulse sequence. It also affects the chemical shift of the analyte peaks in the EXSY spectra.

Finally, the spectral range of <sup>1</sup>H nuclei is relatively small compared to other common nuclei such as <sup>13</sup>C, <sup>15</sup>N, or <sup>19</sup>F. This often leads to extensive peak overlap in multicomponent

samples such as the glucose loaded AOT reverse micelles described here. This complicates peak fitting during analysis but does not seriously jeopardize the quantitative power of the NMR spectroscopy technique.

#### 1.4 Complementary Measurement Techniques

Preparing and analyzing the glucose loaded AOT reverse micelles required additional means of evaluation in the form of dynamic light scattering (DLS) and differential scanning calorimetry (DSC). Accurately preparing for the DLS measurements required the collection of viscosity data (figure 1.7). The viscosity of 0.1 M AOT in isooctane solvent was measured using a Cannon-Fenske 9721-B74 (Cole Parmer) viscometer as a function of temperature. The setup included a temperature-controlled water bath accurate to 0.1 K as well as an electronic timer for measuring efflux through the glass tube. Each viscosity measurement was repeated in triplicate.

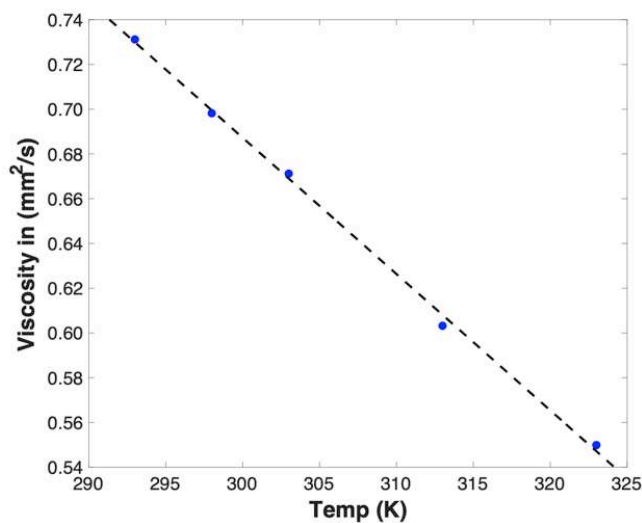


**Figure 1.7:** The relationship between the viscosity of 0.1 M AOT isooctane ( $\gamma$ ) and temperature ( $T$ ) can be expressed by the equation:  $\gamma = -0.0061T + 2.50$

### 1.4.1 Size evaluation with dynamic light scattering

We use dynamic light scattering (DLS) data collected on the Malvern Zetasizer Nano ZS in backscatter mode ( $173^\circ$ ) to evaluate glucose loaded AOT reverse micelle size as a function of temperature (figure 1.8). A table of size distributions may be found in figure S1.4.

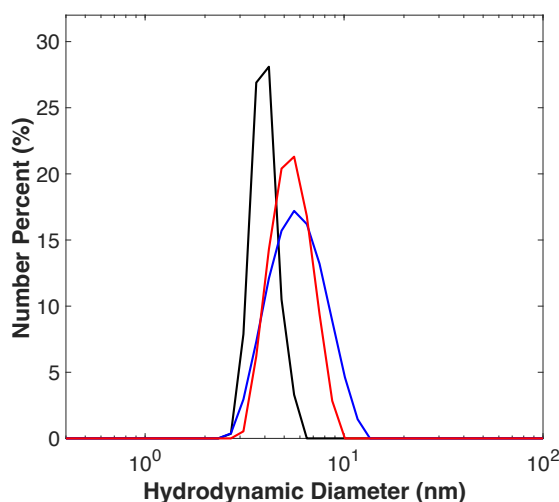


**Figure 1.8:** Particle number distribution vs. hydrodynamic diameter plots obtained from the DLS experiment for  $w_0=10$  reverse micelles loaded with glucose at a 30:1 water to glucose ratio.

Size measurements were averaged over three sets of data, each consisting of ten scans. We report sizes number distribution. Reverse micelle sizes were measured as a function of temperature to the lowest limit afforded by the instrument (275 K). The DLS data reveal that the glucose loaded AOT reverse micelles are approximately 6.0 nm in diameter, which is consistent with our expectations for glucose loaded  $w_0=10$  reverse micelles. The full width at half max of the distribution curves in figure 1.8 indicate that the sample was not perfectly monodisperse; A monodisperse sample would yield a narrower intensity distribution curve centered about a single value. Two-minute equilibration between measurements provided stable uniform temperature distribution in samples.

### 1.4.2 Phase behavior with differential scanning calorimetry

Given the range of temperatures probed in this experiment, we employed differential scanning calorimetry (DSC) to evaluate the possibility of a freezing event, which would clearly affect the kinetics of hydrogen exchange. Glucose loaded AOT reverse micelle mixtures were placed into Tzero hermetic aluminum pans (TA instruments) and fully sealed prior to collection. Sample mass did not exceed 50.00 mg. Temperature sweeps (10 °C/min) were performed over the range 238 K to 303 K, matching the range of temperatures probed in the 1D EXSY NMR experiments. Measurements were repeated in triplicate. Each of these experiments, as well as NMR studies, demonstrated reversible behavior for samples that did not require additional agitation to restore reverse micelle formation. The thermogram in figure 1.9 shows no evidence of a thermodynamic phase change. Any peaks in the spectrum that would disrupt the horizontal regions would indicate a release or uptake of heat in the system.

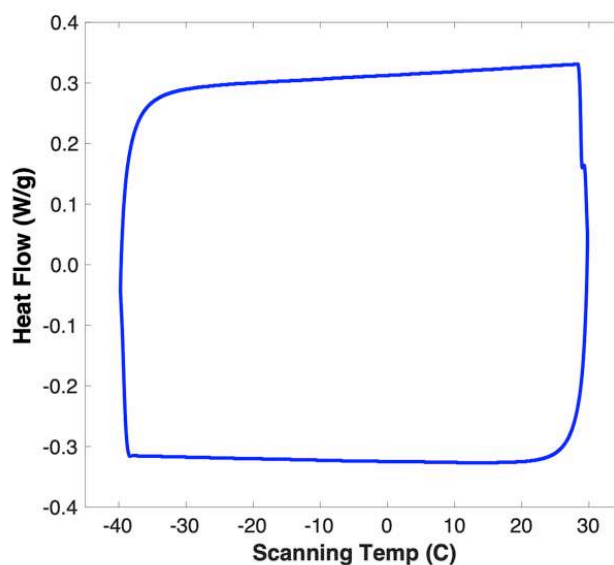
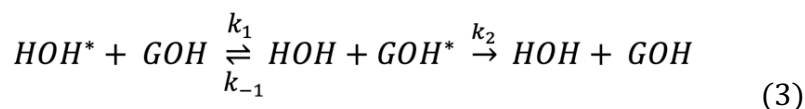


**Figure 1.9:** Differential scanning calorimetry thermogram showing no detectable phase change in the glucose loaded AOT reverse micelles. Initially, we scanned from high temperatures to low temperatures at a rate of 10 °C /min, then cycled back to room temperature by ramping up temperature from the subzero regime to account for hysteresis

## 1.5 The Kinetic Model and Fitting in MatLab

The goal of the study reported here is to determine the activation energy barrier to hydrogen atom exchange between water and glucose that arises from confinement in reverse micelles. We model this using the chemical equation provided in EQN 3:



HOH represents water, GOH represents a glucose hydroxyl, and HOH\* indicates a water molecule whose hydrogen has been energetically labelled with a radio frequency pulse during the EXSY NMR experiment. The transfer of the asterisk from the HOH to the GOH represents the exchange of the labile hydrogen of interest. The rate constant  $k_1$  quantifies the rate of hydrogen exchange from water to glucose while  $k_{-1}$  indicates the reverse process. We assume that  $k_1 \gg k_{-1}$  due to the high  $pK_a$  of glucose ( $pK_a \approx 12$ ).<sup>16</sup> The rate constant  $k_2$  indicates spin-lattice relaxation back to equilibrium. Rearranged to quantify the amount of labelled glucose, we arrive at EQN 4:

$$[GOH^*] = \frac{k_1}{k_2 - k_1} [GOH]_o (e^{-k_1 t} - e^{-k_2 t}) e^{-t/T_1} + C$$

We determined hydrogen exchange rates at each temperature specified from plots of integrated intensity (figure 1.10) as a function of mixing time after fitting to EQN 4 in custom MatLab code. The custom MatLab code is shared in Appendix 1.

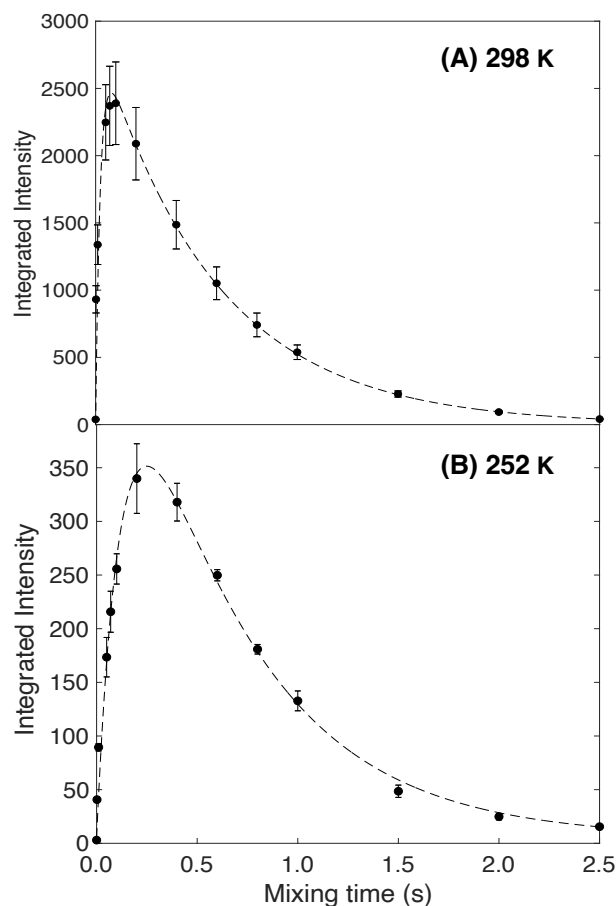


**Figure 1.10.** Integrated intensity of NMR peaks from EXSY experiments as a function of mixing time for the glucose  $1\alpha$  hydroxyl in glucose loaded  $w_0=10$  AOT reverse micelles at **(A)** 298 K (25 °C) and **(B)** 252 K (-21 °C). Error bars reflect standard deviation between three replicate measurements.

## 1.6 Kinetic Exchange Behavior

In addition to analyzing the exchange process for the  $1\alpha$  and  $1\beta$  anomeric hydroxyls, we also explored the rate of water hydrogen exchange with the four other glucose hydroxyl groups at carbons 2, 3, 4, and 6 (figure 1.3). Because the NMR signals for the anomeric hydroxyl groups are well separated from other protons, we can quantitatively evaluate their integrated intensities across the entire temperature range measured. At temperatures higher than 273 K, all the glucose hydroxyl peaks are sufficiently well-separated to determine exchange rates and rate

constants  $k_1$  and  $k_2$ . Figure 1.11 shows the exchange rate constants as a function of decreasing temperature in this high temperature regime. However, as the temperature drops, the signals associated with hydroxyl groups on carbons 2, 3, 4, and 6 broaden and merge, as figure 1.2 shows. This prohibits quantitative integrations to yield accurate rates. Table S1.2 in the associated appendix reports values for  $k_1$  and  $k_2$  extracted from the fitted curves for all temperatures investigated.

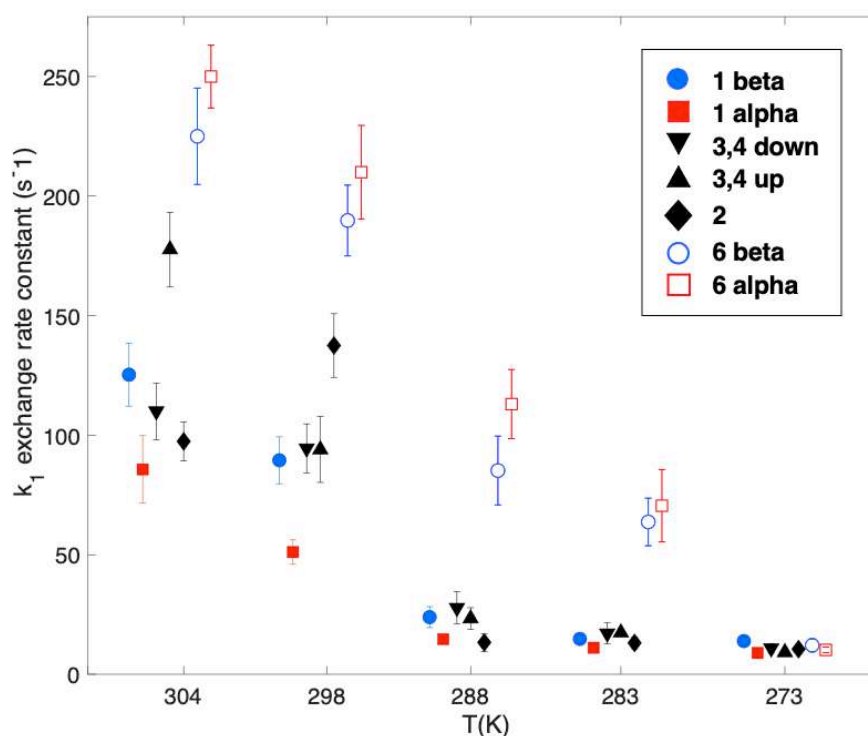


**Figure 1.11.** Rate constants for hydrogen atom exchange between water and glucose hydroxyl at each carbon position on the glucose ring as a function of decreasing temperature. Rate constants were measured for each hydroxyl at each labeled temperature but data points in each cluster are offset on the x-axis for clarity. Error bars reflect uncertainty propagated from three replicate measurements.

The  $k_1$  rate constants in figure 1.11 decrease with decreasing temperature as less thermal energy is available to the system to overcome the barrier to physical exchange. As the solution cools, the viscosity of the reverse micelle solution increases, leading to longer correlation times,

as expected. These longer correlation times result in shorter  $T_1$  times and thus higher relaxation rates. This faster relaxation at lower temperatures agrees with expected trends for longer correlation times for water.<sup>21,22</sup> The approximately two-fold change in the  $k_2$  relaxation rate constant over the temperature range we explored is substantially smaller than the >20-fold change in the exchange constant,  $k_I$ , when transitioning from the highest to lowest temperature.

To determine an activation energy for chemical exchange between water and glucose, we constructed Arrhenius plots using the rate constants obtained for each temperature. Arrhenius plots characterize the temperature dependent exchange for the  $1\alpha$  (figure 1.12A) and  $1\beta$  (figure 1.12B) hydroxyl groups on glucose in the reverse micelle according to the known Arrhenius equation shown in EQN 5 which can be rearranged into the equation for a linear line to extrapolate the activation energy from the value of the slope (EQN 6):

$$k = Ae^{\frac{-E_A}{RT}} \quad (5)$$

$$\ln(k) = \frac{-E_A}{RT} + \ln(A) \quad (6)$$

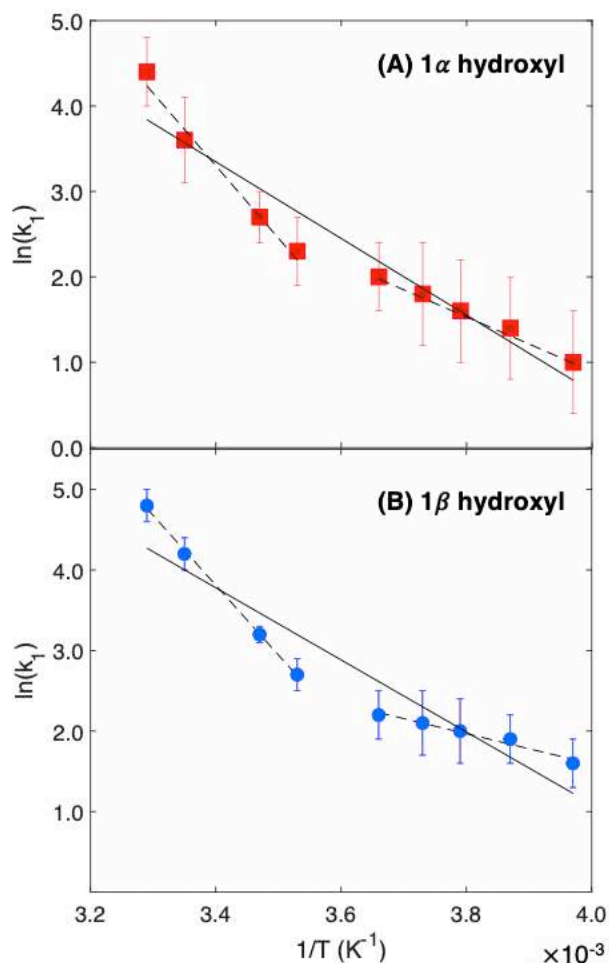


**Figure 1.12.** Arrhenius plots of proton exchange rate as a function of inverse temperature and fits to single linear fit (solid lines) and linear fits to high and low temperature regimes (dashed lines). **(A)**  $1\alpha$  hydroxyl **(B)**  $1\beta$  hydroxyl. Error bars represent the uncertainty from three measurements.

Each point represents the average  $k_1$  rate extracted from three individual EXSY NMR experiments of the same sample at the chosen temperature; error bars indicate the standard deviation between measurements. Fits shown in figure 1.12 reveal that a single linear fit does not accurately describe the data over the full temperature range measured, so we also performed linear fits to data in high and low temperature ranges. Systematic divergence of the data from the single line fit, as well as the  $R^2$  values, show that fitting the data to high and low temperature ranges is superior to a single linear fit (Table S1.3).

Using the Arrhenius equation (EQN 5), we obtained the activation energy,  $E_A$ , from the slopes of the fits. At temperatures above 285 K, we find the activation energies for exchange between water and glucose  $\alpha$  and  $\beta$  anomers are  $73.3 \pm 6.1$  kJ/mol and  $76.8 \pm 6.6$  kJ/mol, respectively. Below the 285 K threshold, the activation energies drop to  $11.8 \pm 2.7$  kJ/mol and  $31.5 \pm 6.9$  kJ/mol for  $1\alpha$  and  $1\beta$  hydroxyl groups, respectively.

Our EXSY NMR spectral data have a high signal-to-noise ratio and yield high precision in the high temperature regime, which degrades as temperature decreases. In this high temperature regime, the measured activation energies for  $1\alpha$  and  $1\beta$  hydroxyls are the same, within the calculated uncertainty. The good signal-to-noise achieved at higher temperatures allows us to analyze the exchange rate behavior of all glucose hydroxyl groups and thus determine the activation energy for exchange at each hydroxyl position on the glucose molecule, as shown in figure 1.13. All the measured exchange rates decrease with decreasing temperature.

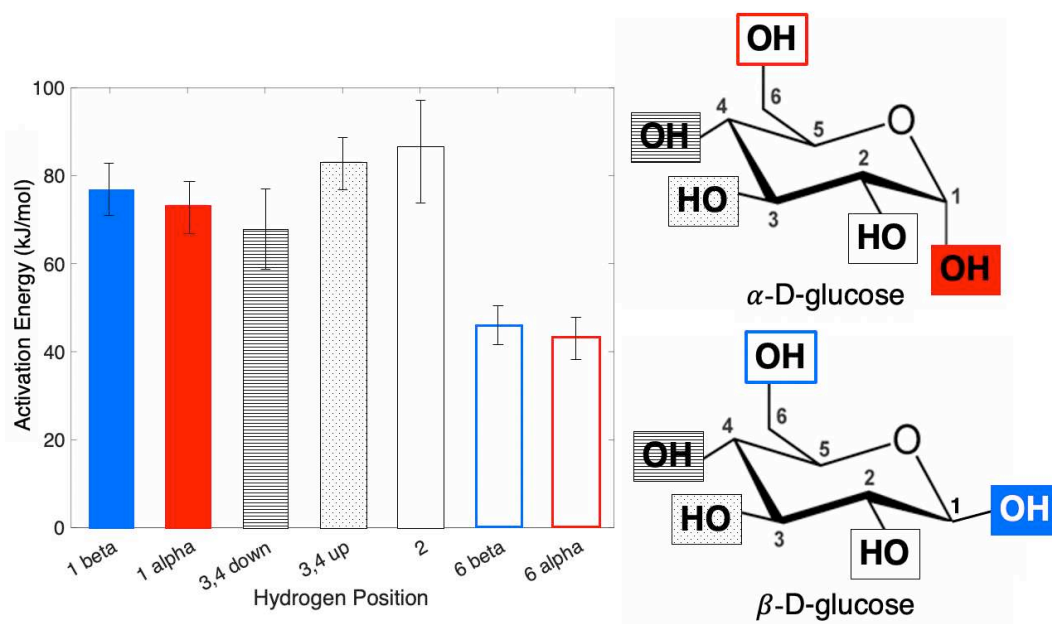


**Figure 1.13.** Activation energies for hydrogen atom exchange between water and glucose hydroxyl at each position on the glucose ring at temperatures above 285 K in kJ/mol. Structures of both anomers are provided to emphasize the differences relative to orientation in space.

The exchange of water hydrogen atoms to glucose molecules nanoconfined in reverse micelles happens much more slowly than the process occurs in bulk water, making it possible for us to measure the activation energy associated with chemical exchange.<sup>23–25</sup> Several explanations can account for how confinement affects each participant, that is, glucose and water, in the exchange process. The confinement presented by the reverse micelle structure can disrupt the water hydrogen bond network that normally facilitates the concerted exchange between water molecules and glucose hydroxyl groups.<sup>26</sup> Rather than forming an extended, inextricably linked network of water molecules constantly breaking and reforming hydrogen bonds, water must compete with the smothering presence of glucose and the AOT headgroups to complete the concerted exchange. In addition, water and/or glucose interactions with ions could disrupt the exchange process. For example, molecular dynamics simulations performed by Zhang *et al.* show how increased ion concentration slows the ability of water molecules to reorient and form new hydrogen bonds.<sup>27</sup> Crowding and direct interactions with ions present at the water-AOT interface may contribute to the energy barrier we measure here. We also considered the possibility of glucose stacking within the reverse micelles. Although glucose-glucose aggregation could block water from accessing glucose hydroxyl groups, reducing exchange rates, previous 2D NOESY NMR measurements showed no close interactions between glucose molecules that would support the existence of glucose aggregation.<sup>28</sup>

To interpret trends in the exchange rates between glucose positions (scatter plot shown in Fig. 1.11) and their associated activation energies, we consider two data cohorts: the 6 $\alpha$  and 6 $\beta$  hydroxyl groups, and all other hydroxyl groups. The first cohort, *i.e.*, 6 $\alpha$  and 6 $\beta$  hydroxyl groups, demonstrates consistently higher exchange rates than the latter cohort. At some temperatures, the difference is greater than a two-fold increase. At 304 and 298 K, the latter

cohort displays a broad distribution of exchange rates that collapse into one general rate at lower temperatures, within the error of the measurements. Within this second cohort, we observe no systematic trend except that the 1 $\alpha$  hydroxyl exchange rate remains consistently smaller relative to the others. Even this rate eventually falls within the average exchange rate by 283 K.

The higher exchanges rate for the 6 $\alpha$  and 6 $\beta$  hydroxyl position also correlates to the lowest barrier for exchange of all the hydroxyl positions on the glucose molecule (Figure 1.13). This could indicate a net orientation of the glucose molecule such that the “free arm” associated with the 6 $\alpha$  and 6 $\beta$  hydroxyl groups of glucose pyranose form protrudes inward toward the reverse micelle water core. In this orientation, the 6 $\alpha$  or 6 $\beta$  hydroxyl group could preferentially sample more bulklike water facilitating its exchange with water’s hydrogens. Interestingly, changing the anomeric hydroxyl group from 1 $\alpha$  to 1 $\beta$  is sufficient to increase the probability of exchange, as the exchange rate for the 1 $\alpha$  anomeric hydroxyl group is consistently smaller than the 1 $\beta$  anomer, though the activation energy for hydrogen exchange does not differ between these two positions. The cohort comprising the 6 $\alpha$  and 6 $\beta$  hydroxyl position has a significantly smaller barrier to hydrogen exchange, with an average of 44.5 kJ/mol, compared to the second cohort comprising the rest of the hydroxyl positions, which has an average exchange barrier of 77.5 kJ/mol. We attribute this 74% increase to the steric hindrance posed by hydroxyl groups that likely reside close to the surfactant/water interface and therefore cannot exchange as easily as the 6 $\alpha$  and 6 $\beta$  hydroxyl positions.

### *1.6.1 Evidence of Hydrogen Tunneling*

Reduced signal to noise and broadening of the signals in the low temperature regime (below 285 K), causes poor spectral separation and precludes quantitative integration for all but

the anomeric hydroxyls. Thus, we limited our low temperature analysis to the  $\alpha$  and  $\beta$  anomeric hydroxyl groups. Considering the trends observed in the high temperature regime, we expect the other hydroxyl groups demonstrate trends similar to the anomeric groups in the low temperature regime.

As the reverse micelles cool, the exchange rate decreases (figure 1.12). However, our differential scanning calorimetry results indicate that the decreased rate is not the result of a freezing event. Despite slower exchange rates than those in the high temperature regime, the Arrhenius plots in the low temperature regime display a significantly shallower slope associated with a lower activation energy. This difference suggests a different mechanism is responsible for the observed hydrogen exchange. We hypothesize that rather than overcoming the barrier to exchange, hydrogen atoms tunnel from water to glucose. Reports of hydrogen atom tunneling in related systems such as nano-water clusters and mono-layered water molecules.<sup>29,30</sup> show that nuclear quantum effects extend the hydrogen-oxygen bond, thereby delocalizing the hydrogens and leaving them susceptible to participate in hydrogen bonds with surrounding molecules.<sup>31</sup> Additionally, reports in the literature suggest that hydrogen bonds get stronger as temperature drops,<sup>32</sup> which can increase the probability of hydrogen tunneling and facilitate hydrogen atom exchange. Furthermore, the confined space created by the reverse micelle could facilitate hydrogen bond shortening, which is regarded as essential to initiate proton tunneling.<sup>33</sup>

To probe the possibility of a hydrogen atom tunneling mechanism, we attempted to test our hypothesis in  $^2\text{H}$  EXSY NMR experiments replacing  $\text{H}_2\text{O}$  with  $\text{D}_2\text{O}$ , deuterating glucose molecules, and following the OD signature with  $^2\text{H}$ -NMR. By substituting  $\text{D}_2\text{O}$  for  $\text{H}_2\text{O}$ , we expect the heavy isotope effect to suppress hydrogen tunneling and yield rate constants consistent with the steeper trend in the higher temperature regime. We deuterated the hydroxyl

hydrogens on glucose and prepared reverse micelles with D<sub>2</sub>O. However, unlike the case with H<sub>2</sub>O and protonated glucose, confinement of deuterated glucose with D<sub>2</sub>O in the reverse micelles did not result in observable OD peaks in the 1D <sup>2</sup>H-NMR spectrum (figure 1.14).

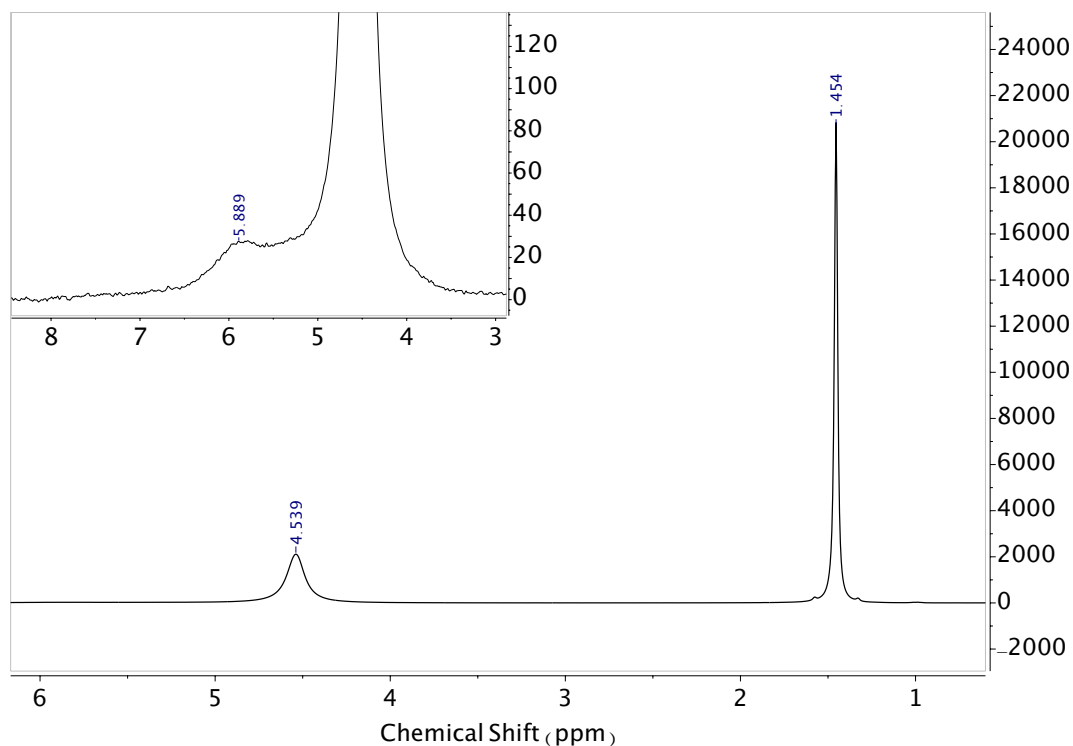


**Figure 1.14.** 1D <sup>2</sup>H-NMR spectra of deuterated glucose loaded AOT reverse micelles. The inset shows a small shoulder on the water peak representative of the deuterated glucose -OD groups. The appearance of this shoulder shows that the -OD groups have coalesced into a poorly resolved peak that is not analytically useful for the extraction of rate constants.

The usual challenges associated with <sup>2</sup>H-NMR such as an approximately seven fold decrease in sensitivity, lower resolution, and shorter T<sub>1</sub> times, precluded observation of OD peaks.<sup>34</sup> <sup>2</sup>H-NMR spectroscopy is always challenged by fast quadrupole relaxation due to the large quadrupole moment ( $2.86 \times 10^3$  barns) of the <sup>2</sup>H nucleus. The large quadrupole moment experiences significant interaction with the surrounding electric field gradients generated by both the solvent and the solute molecules, therefore making relaxation extremely efficient and

broadening the signal lineshapes.<sup>35</sup> Indeed, the challenges of adapting a  $^2\text{H}$ -NMR study to systems is well documented in the literature.<sup>36–38</sup> Thus, we could not measure the exchange in an  $^2\text{H}$ -EXSY NMR experiment to confirm the isotope effect. Still, we believe that hydrogen atom tunneling is a good possibility given its demonstrated presence in similar low temperature water systems.<sup>33,39</sup>

The barrier to hydrogen atom exchange as expressed by the calculated activation energies is more than 2.5 times higher for the  $1\beta$  hydroxyl compared to the  $1\alpha$  position. Given our interpretation of a net orientation for intramicellar glucose molecules from data in the high temperature regime, this lower barrier for the  $1\alpha$  position may indicate stronger hydrogen bonding as the temperature drops, conceivably with water molecules trapped between the glucose and the reverse micelle interface. It is possible that other factors could impact the exchange we measure in our reverse micelle samples. Our measurements of reverse micelle size display a modest increase in reverse micelle size with decreasing temperature. If reverse micelles become larger at lower temperatures, we expect an increase rather than a decrease in the exchange rate as larger water pool should provide increased access to water molecules and reduced water network disruption. Thus, the change in reverse micelle size does not provide a good explanation of the reduced barrier we observe in the low temperature regime.

We turned to separate experiments conducted by Suzuki *et al.* and Van Horn *et al.* to better understand our results and contextualize the lack of observed water shedding. Suzuki *et al.* recorded a noticeably smaller hydrodynamic radius of their  $w_0=10$  reverse micelles using a similar DLS method ( $2.8 \pm 0.1$  nm). To maintain the structural integrity of their smaller reverse micelles, they required a rapid cooling rate ( $\sim 6000$  K/min) for their experimental measurements. Based on their results, one might expect the formation of large ice crystals outside the micelle.

We explain the lack of ice formation by pointing out our reverse micelles are much larger than even their  $w_0=10$  reverse micelles, and thus preventing ice expulsion.<sup>40</sup> Van Horn *et al.* specifically cite 243 K as the threshold for ice formation, nine degrees below our lowest measurement. Although much of their experiment revolves around the encapsulation of ubiquitin, rendering direct comparison to our system impossible, they too used working hydrodynamic diameters much smaller than ours (3.64 nm).<sup>41</sup> Similar 1D <sup>1</sup>H-NMR experiments conducted by Klíčová demonstrated extracellular ice would completely eliminate the water peaks from the 1D <sup>1</sup>H-NMR scans we collected ourselves previous to the EXSY NMR experiments.<sup>42</sup> Since our ability to set up the EXSY NMR experiment depended on the identification of the water peak's frequency, ice formation was yet again ruled out. Furthermore, Klíčová note in their discussion that the formation of ice would cause irreversible damage to the sample, preventing the water from entering the micelle again and thus preventing the subsequent collection of quality 1D <sup>1</sup>H-NMR spectra at other, higher temperatures.

It is possible that lower temperatures could cause the intramicellar glucose molecules to experience a different environment from its location reverse micelles in the high temperature regime. In previous work, we hypothesized that glucose resides near the AOT headgroups where it could shield the positive sodium atoms from the negatively charged AOT headgroups.<sup>28,43</sup> The increase in reverse micelle size with decreasing temperature could indicate glucose moving away from the interface thus increasing reverse micelle volume. However, in this environment, we would again expect more facile exchange with increased access to the water pool. Likewise, a drop or rise in intramicellar pH should dramatically increase the exchange rate as the mechanism changes from concerted to charge transfer.<sup>25</sup>

The observation of two temperature regimes and subsequent proposition of hydrogen tunneling should give caution to the assumption that hydrogen exchange in confined biological spaces proceeds via a classical energy barrier. In fact, these data may indicate tunneling can occur at a relatively high temperature when water and glucose are in a nanoconfined space. The threshold temperature for the transition to tunneling may suggest that this phenomenon could occur more easily in biological systems than previously thought. We have reduced the rate of exchange with the relatively simple act of reducing the space available to the glucose and water pool. This same method of nanoconfinement could be used to introduce energy barriers that allow for the study of previously unobserved high energy intermediates or transition state structures. The occurrence of hydrogen tunneling as a result of the low barrier hydrogen bond (LBHB) has been extensively studied,<sup>44-46</sup> and numerous other studies have begun to link hydrogen tunneling to biological systems, mostly in enzymatic catalysis.<sup>47-50</sup> Our results encourage this continued re-examination of such processes to search for an energy barrier previously presumed negligible.

## 1.7 Conclusion

Confinement of glucose and water within a  $w_0=10$  reverse micelle retards the process of single hydrogen atom exchange, making the unobservable exchange process in bulk solution measurable with <sup>1</sup>H-EXSY NMR. For the first time, we report the value of this energy barrier to exchange. The unexpected departure from a single linear trend in the reported Arrhenius plot suggested differing mechanisms for hydrogen atom exchange at higher and lower temperatures.

Probing energy barriers present between water and other osmolytes extends beyond alternative carbohydrates like trehalose or fructose.<sup>51,52</sup> Because the preparation of reverse

micelles results in a size-tunable, isolated droplet, this methodology can be easily extended to produce other simplified model environments. This work most directly benefits the fields of biotechnology or pharmacology, as they necessitate that researchers understand more complex chemical reactions at interfaces or in sequestered, nanosized pockets of enzymes or other biomolecules.

## CHAPTER 2: IMPACT OF UREA ON REVERSE MICELLE SYSTEMS

### 2.1 Introduction

This project was initiated after the completion of the investigation of glucose in reverse micelles, whose progress was greatly aided by the foundational work of a previous student, Dr. Benjamin Wiebenga-Sanford. The findings here reflect the work published in the *Langmuir*. (Source: Miller S.L., Levinger, N.E. Urea Disrupts the AOT Reverse Micelle Structure at Low Temperatures. *Langmuir* 2022, 38, 24, 7413–7421)

Urea in aqueous solutions presents unique properties that are relevant to many different scientific communities. Aside from being highly water soluble,<sup>53</sup> urea has been shown to enhance the solubility of hydrocarbons in water,<sup>54–56</sup> cause proteins to denature,<sup>57,58</sup> and prevent micellar aggregation<sup>49,59</sup> by mediating the critical micelle concentration of various surfactants.<sup>60,61</sup> Because of these findings, numerous studies abound that examine how urea perturbs the local hydrogen bond network of water.<sup>62,63</sup>

Both simulations and experiments have spearheaded the effort to describe urea-in-water solutions. Within the biochemical community, urea is well known to be able to denature proteins,<sup>58,64</sup> and as an osmolyte, urea has a unique effect on the traditional hydrogen bonds in bulk urea-in-water solutions.<sup>63,65,66</sup> For example, molecular dynamics simulations have generally shown that an increasing urea mole fraction disrupts the elaborate three-dimensional tetrahedral framework of the water hydrogen bond network, leading to differences in solvation abilities.<sup>63,65</sup> Cabellero-Herrera *et al.* used molecular dynamics simulations to show that the denaturing effect of urea on proteins could be attributed to the decreased mobility of water in the presence of urea.<sup>66</sup> This simulation also reported an increase in water-peptide bonds as a result of urea's

presence, which destabilized the hydrogen bonds that would otherwise stabilize the  $\alpha$ -helix structures within the protein. Coupled with experimental neutron diffraction studies, molecular dynamics simulations show that urea readily inserts itself into water and can form hydrogen bonds at both the carbonyl and amine functional groups.<sup>67</sup> Further neutron diffraction investigations by Yasuo *et al.* found that such small intermolecular distances between oxygen atoms within the water hydrogen bond network confirmed the breakdown of the tetrahedral water network.<sup>68</sup>

Despite these studies that label urea as a structure breaker, others have suggested urea is actually a structure maker based on a Kirkwood-Buff analysis, that is, urea stabilizes the protein structure.<sup>69</sup> Investigations of urea and water solutions have also included spectroscopy studies, where both transient absorption and time resolved IR experiments show a sensitive response to the local solvent structure and its changes over time.<sup>70-73</sup>

### *2.1.1 Urea in Reverse Micelles*

Considering the rich network of studies describing urea-in-water solutions, we focus on changes brought to this system by nanoconfinement that mimic the intracellular spaces where urea is biologically active. It is well documented that nanoconfined water displays markedly different characteristics when compared to its bulk behavior.<sup>74,75</sup> Water confinement within nanosized spaces has been achieved through various means including carbon and lipid nanotubes,<sup>76-79</sup> silica-based pores,<sup>80-82</sup> and aerosolized particles.<sup>3,83</sup> As in chapter one, we achieve nanoconfinement using AOT reverse micelles, shown in figure 2.1. Reverse micelles are a popular choice for mimicking biological spaces with limited amounts of water such as intercellular and intra-organelle spaces, the interiors of macromolecular transport vesicles, or

transport proteins and aquaporins.<sup>84,85</sup> They also complement the emergent interest in nanofluidic devices.<sup>86</sup> The reverse micelle size is described by a unitless parameter  $w_0 = [H_2O]/[surfactant]$  that describes the water loading ratio relative to the amount of surfactant. In the work reported here, we prepared reverse micelles with AOT surfactant with  $w_0=10, 15,$  and  $20,$  which generally creates reverse micelles that are  $\sim 5-12$  nm in diameter. AOT is an attractive surfactant due to the ease of reverse micelle preparation, thermodynamic stability, as well as being inexpensive and non-toxic.

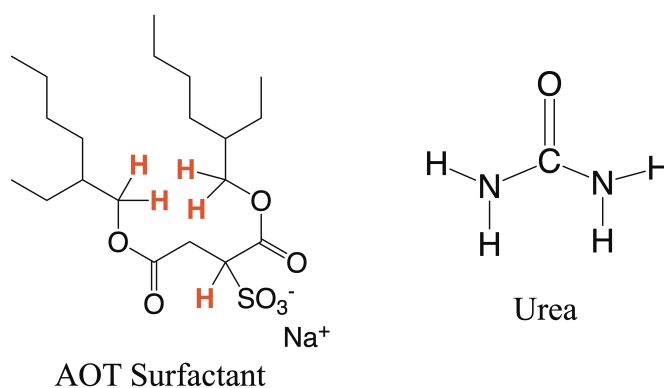


**Figure 2.1:** Labelled chemical structures of the AOT surfactant molecule and the planar urea molecule used in this study. 2D  $^1\text{H}$ -NOESY NMR experiments indicate the hydrogens explicitly shown in red interact with urea.

Previous experiments have studied urea in micelle and reverse micelle samples with varying results. For example, spectrofluorometer scattering data show that low concentrations ( $<1.0$  M) of urea appears to stabilize AOT reverse micelle structure; chemical structures of both molecules are shown in figure 2.1.<sup>59,87</sup> Ceraulo *et al.* has reported that urea interacts with the sulfonate headgroup through a hydrogen bond with urea's amino group and also showed that urea caused differentiation between the two hydrocarbon chains comprising the AOT surfactant which then had distinct solubilizing roles.<sup>88</sup> Caponetti *et al.* used small angle x-ray scattering and FT-IR to demonstrate that urea in AOT reverse micelles began to interact with the hydrophilic

headgroups of the AOT molecule and created greater disorder within the inner hydrogen bond network.<sup>89</sup>

To date, studies of urea in reverse micelles have not taken into consideration the effect of variable temperature, either on interaction of urea with the reverse micelle surfactant or inner water pool. By coupling techniques such as dynamic light scattering (DLS) as well as one and two dimensional NMR spectroscopies, we extend the current description of how nanoconfinement affects both the structure and dynamics of these rich systems. NMR techniques are extremely sensitive to changes in the chemical environment, making this union of technique and research question ideal. Urea is an attractive molecule for insertion into the reverse micelle water interior because the key analyte peaks do not overlap with the known resonances of either the surfactant or the non-polar solvent isooctane. Furthermore, knowledge of chemical shift, resonance linewidths, relaxation rates, and exchange rates can illuminate the mechanisms of transport occurring where nitrogenous waste is expelled via concentration gradients created within the vasculature of the kidneys.<sup>90</sup>

## 2.2 Preparation of Urea in Reverse Micelles

Urea (99.9%), aerosol OT (AOT, (bis-(2-ethylhexyl) sulfosuccinate sodium salt, 99.9%), 2,2,4-trimethylpentane (isooctane, 99.9%), and cyclohexane-*d*<sub>12</sub> (99.9%) were purchased from MilliporeSigma (Burlington, MA) and used as received. D<sub>2</sub>O (99.9%) was acquired from Cambridge Isotope Laboratories. We refer to 2,2,4-trimethylpentane as isooctane throughout this thesis. All water used in the experiment was Millipore filtered for 18 MΩ resistivity. Prior to use, all glassware, including NMR tubes, was acid washed with concentrated HNO<sub>3</sub>, copiously rinsed with Millipore filtered water, and thoroughly dried.

Samples of reverse micelles were prepared from 0.1 M AOT stock solutions in isooctane with subsequent additions of water, then urea. Solid AOT was added by mass to the isooctane solvent to achieve a 0.1 M concentration. Next, water was added to form the reverse micelle nanodroplets to the desired  $w_0$  value and sonicated. Urea was loaded by mass to achieve a 1:30 urea:water mole ratio and further sonicated for ~50 min until complete emulsification was achieved. Although the concentration of the urea within the reverse micelles was ~2 M, the overall urea concentration was 30 mM.

### **2.3 Detection with NMR spectroscopy**

All NMR spectra were processed in MNOVA (ver. 12.0.4-22023). The size of the direct NMR FIDs was 32,768 data points. T1 measurements totaled 8192 data points. All spectra were zero-filled to twice the number of data points and apodized with a 1.00 Hz exponential weighting function. Individual peaks were fitted with Lorentzian-Gaussian lineshapes using MNOVA software and subsequently integrated. Integrated intensities were used to follow chemical exchange between water and urea and were analyzed using custom written code in Matlab (MatLab ver. R2021b).

#### *2.3.1 EXSY pulse sequence description*

EXSY NMR experiments on the Varian Inova 500 MHz NMR spectrometer were initiated by collecting a 1D  $^1\text{H}$ -NMR spectrum to locate the water peak frequency rate. Next, the 1D EXSY NMR spectra were collected. The 1D EXSY experiment measures the physical exchange of excited water hydrogens to the labile urea hydrogens bonded to the nitrogen. Pulse widths were measured before each experiment to ensure the maximum signal to noise.

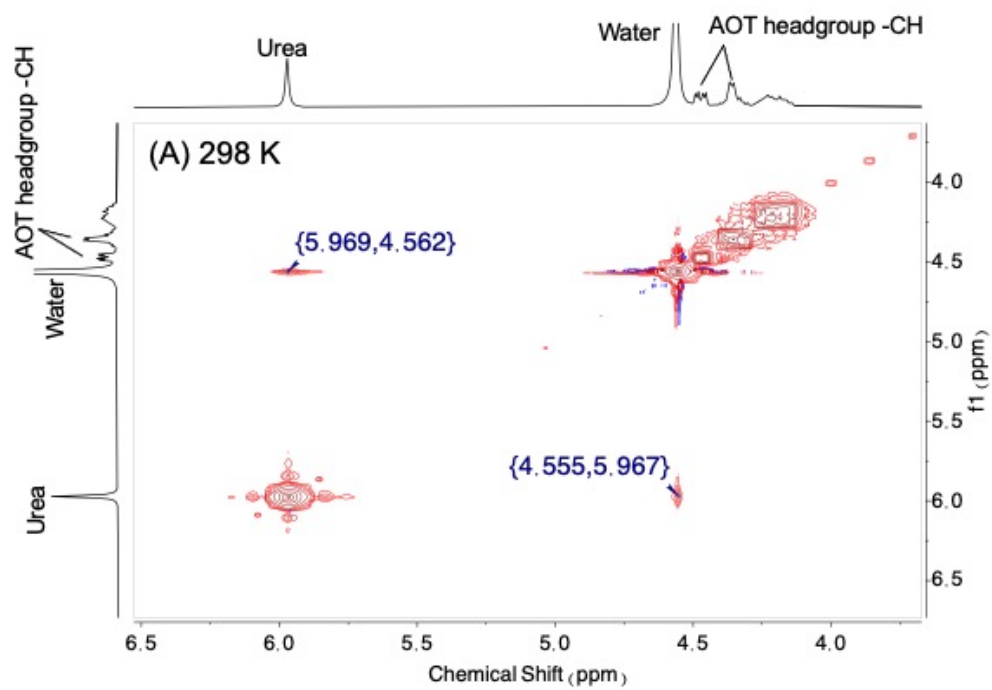
Homospoil pulses were used to dephase any residual transverse magnetization caused by imperfect  $\pi$  pulses. The 1D EXSY mixing times (in seconds) were assigned to the following values using a pre-set array command: 0.002, 0.01, 0.04, 0.08, 0.1, 0.5, 1.0, 1.5, 2.0, 2.5, 3.0, 3.5, 4.0, 4.5, 5.0, 6.0, 7.0, 8.0, 9.0, and 10.0 sec. The hard pulse labels hydrogen atoms on water molecules that subsequently exchange onto urea during the mixing period; this results in the appearance of urea NH peak around 6.0 ppm. The mixing period, or exchange delay, follows the selective  $\pi$ -pulse that labels a frequency-defined spin across its full width half height frequency. No presaturation or WATERGATE sequences were used to damp the water signal as water and urea peaks were sufficiently separated to avoid overlap that could cause difficulty in peak analysis.

The integrated intensity of the urea NH peaks allowed us to quantify the exchange rates as they are a direct result of the hydrogen's transition from water to urea. Measurements at each temperature were performed in triplicate. EXSY NMR spectra were collected at nine temperatures for the  $w_0=10$  reverse micelles: 303, 298, 288, 283, 273, 268, 264, 258, and 251 K (31, 25, 15, 10, 0, -5, -9, -15, -21 °C). Later replicates using the  $w_0=15$  and 20 reverse micelles were collected at just three different temperatures: 298, 273, and 253 K.

### 2.3.2 2D $^1\text{H}$ -NOESY experiments

2D  $^1\text{H}$ -NOESY NMR spectra were collected on a Bruker Neo 400 MHz NMR spectrometer at 275 K and 298 K for urea loaded  $w_0=10,15$ , and 20 reverse micelles to assess intermolecular interactions between urea and AOT. 2D  $^1\text{H}$ -NOESY spectra of the  $w_0=10$  reverse micelles shown in figure 2.2A and 2.2B predictably show cross peaks between urea NH protons at  $\sim 6$  ppm and water at  $\sim 4.5$  ppm at both temperatures measured. In figure 2.2B, additional cross

peaks appear at 275 K between the AOT headgroup CH peaks and the urea NH peak demonstrating that urea interacts with the AOT headgroup protons. These headgroups protons are shown explicitly in figure 2.1 using red highlighting. Figure S2.2 and figure S2.3 show the additional 2D  $^1\text{H}$ -NOESY NMR spectra collected for the other temperature dependent measurements of  $w_0=15$ , and 20 reverse micelles.



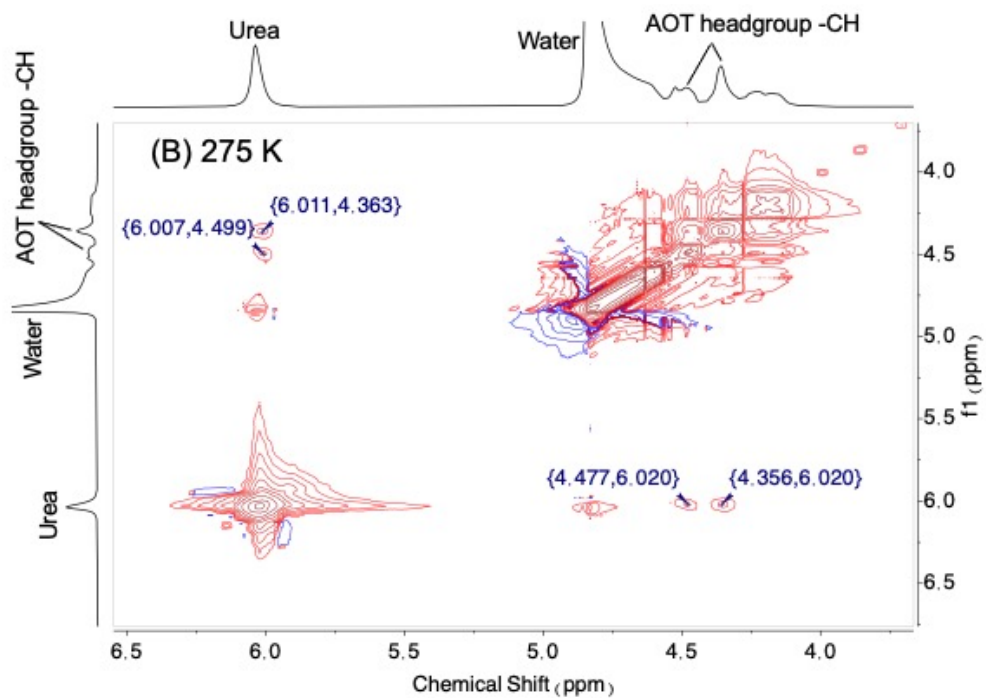


**Figure 2.2.** 2D <sup>1</sup>H-NOESY NMR spectra showing the region of interest for urea loaded  $w_0=10$  AOT reverse micelles (A) 298 K and (B) 275 K.

In contrast, only water-urea cross peaks appear in the 2D <sup>1</sup>H-NOESY spectra for  $w_0=15$  and 20 reverse micelles at both 275 K and 298 K with no cross peaks between urea and the AOT protons at any temperatures probed. We note that 1D <sup>1</sup>H-NMR spectral quality degrades with lowering temperature, as shown in figure 2.3.

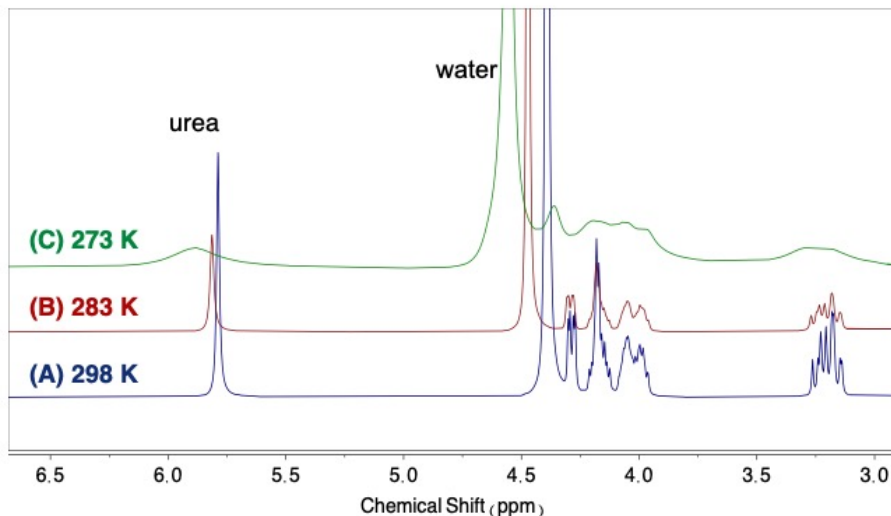


**Figure 2.3.** Stacked 1D  $^1\text{H}$ -NMR spectra of 2 M urea in  $w_0=10$  reverse micelles at (A) 298 K (B) 283 K and (C) 273 K showing that peak widths increase with decreasing temperature.

## 2.4 Observation of temperature-dependent size measurements

To ensure the stability of the urea loaded reverse micelles, additional measurements were conducted to evaluate the size dispersion of reverse micelle emulsions. Viscosity data crucial for extracting accurate size measurements of reverse micelle samples were collected as a function of temperature using a Cannon-Fenske 9721-B74 (Cole Parmer) viscometer. A temperature-controlled water bath accurate to 0.1 K and an electronic timer assisted the measured efflux through the Ubbelohde glass tube. Each of the five viscosity measurements of 0.1 M AOT was repeated in triplicate.

Size measurements were used to evaluate reverse micelle stability and the environment the encapsulated urea experiences (figure 2.4). Reverse micelle formation and sizes were evaluated as a function of temperature using dynamic light scattering (Malvern Zetasizer Nano ZS) in backscatter mode ( $173^\circ$ ). Measurements were performed in triplicate to extract average size across 30 scans. The lower temperature limit of the instrument precluded measurements

below 275 K, which prevented measurements that mirrored the lowest temperatures probed in NMR studies. The reported error of the internal thermometer was  $\pm 0.2$  K. A five min equilibration time between measurements ensured homogenous temperatures throughout the aqueous sample.

As temperature is initially ramped down to the lower limit of the instrument, we note that reverse micelles of all  $w_0$  values grow larger and more disperse with no hysteresis. That is, the size and polydispersity for individual reverse micelle samples is conserved regardless of whether the temperature was achieved via cooling or warming. For the smallest reverse micelles measured,  $w_0=10$ , DLS scans reveal a dramatic effect of low temperature on the samples; at the instrument's low temperature limit of 275 K, the reverse micelle size and polydispersity increase to the point where the solution contains reverse micelles as large as 50 to 100 nm, increasing from the size at room temperature by nearly an order of magnitude. In one experiment, a shoulder centered about 20 nm appeared during the temperature ramping period suggesting that the low temperature favors the formation of larger micelles.

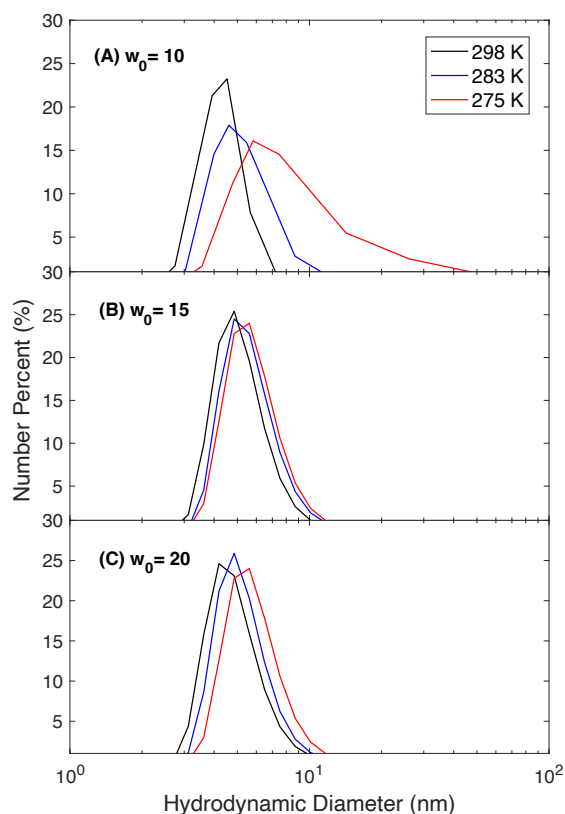
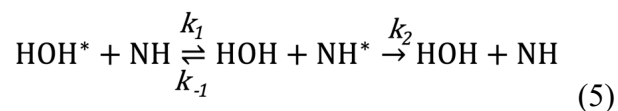


**Figure 2.4:** Dynamic light scattering of (A)  $w_0=10$  (B)  $w_0=15$  and (C)  $w_0=20$  AOT reverse micelles with 1:30 urea:water as a function of temperature: T = 299 K (black), 283 K (blue), and 275 K (red).

## 2.5 Kinetic Exchange Behavior

In previous experiments, we have measured the exchange between water and hydroxyl groups on sugars and sugar alcohols, noting a significant slowing down of the exchange when these molecules are encapsulated in reverse micelles.<sup>14,91</sup> We also found evidence for two different regimes wherein exchange between water and glucose follows expected Arrhenius behavior at higher temperatures but appears to tunnel at modestly low temperature, around 273 K. Here we explore chemical exchange between water and urea in bulk aqueous solution and in AOT reverse micelles. The planar urea molecule possesses four labile hydrogens that are bonded to the nitrogen of the primary amide groups flanking the central carbonyl, as shown in Scheme 1.

The urea protons are subject to exchange with water and appear consistently at  $\sim 6$  ppm in the NMR spectra. The exchange process between water and urea is described in EQN 5:



This equation mirrors EQN 3 in chapter 1 used to model the glucose in reverse micelle system described earlier, although here we use NH to describe the labile proton on the urea amide group. Using a range of mixing times in the EXSY-NMR pulse sequence allows us to measure the time dependence of the exchange process, which is longer than that of the confined glucose system.

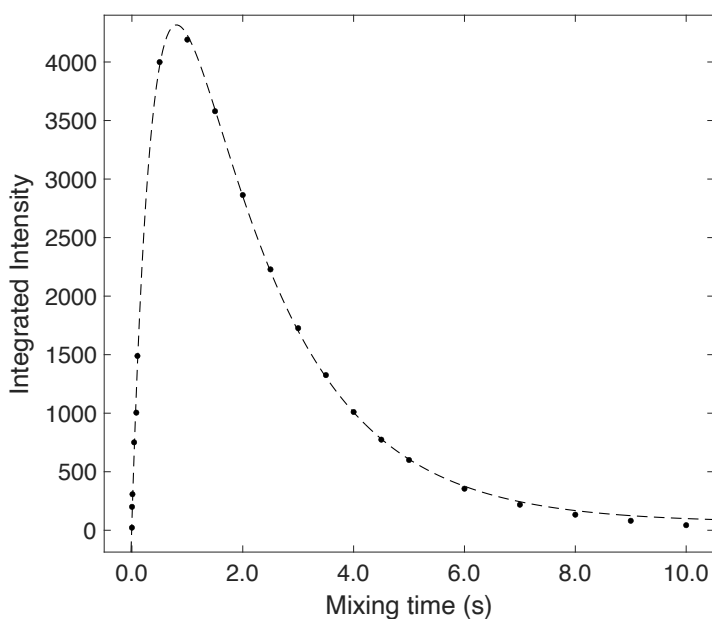


**Figure 2.5:** Integrated intensity of the EXSY-NMR peaks as a function of mixing time (points) and fit to eqn 2 (dashed line) at 298 K (25 °C) for  $w_0=10$  reverse micelles containing 2 M urea.

A sample of the raw EXSY-NMR data collected for the urea in water systems examined can be found in figure S2.1. Figure 2.3 shows representative data of the integrated intensity of the urea  $\text{NH}^*$  signal as a function of mixing time determined from EXSY-NMR spectra of  $w_0=10$  AOT reverse micelles with a 1:30 urea:water mole ratio collected at 298 K. The initial rise in the data points in figure 2.5 indicates the rapid exchange of hydrogen atoms; it is followed by relaxation to chemical equilibrium that occurs for both bulk and nanoconfined urea solutions. We fit these data to EQN 6 to obtain values for rate constants.

$$[\text{NH}^*] = \frac{k_1}{k_2 - k_1} [\text{NH}]_o (e^{-k_1 t} - e^{-k_2 t}) e^{-t/T_1} + C \quad (6)$$

Values for  $k_1$  exchange constants for all temperatures and  $w_0$  values are given in table 2.1. The exchange rates between water and urea in bulk aqueous solution and in  $w_0=20$  reverse micelles are the same within our error, with slightly lower rates for  $w_0=15$ . At high temperatures, the chemical exchange between water and urea is significantly slower for  $w_0=10$  reverse micelles but surprisingly, the rates increase with decreasing temperature. Additional extracted parameters such as the  $k_2$  constant are provided in table 2.1.

**Table 2.1:** First order exchange rate constants,  $k_1$ , measured by EXSY-NMR spectroscopy at various temperatures.

<b>T (K)</b>	<b><math>w_0=10</math> RMs</b>	<b><math>w_0=15</math> RMs</b>	<b><math>w_0=20</math> RMs</b>	<b>Bulk 2 M urea</b>
303	2.1( $\pm$ 0.4)			
298	2.3 ( $\pm$ 0.3)	4.7 ( $\pm$ 2.0)	11.9 ( $\pm$ 2.0)	15.3 ( $\pm$ 3.1)
293	2.3 ( $\pm$ 0.3)			
288	2.5 ( $\pm$ 0.6)			
283	3.0 ( $\pm$ 0.5)			
273	3.2 ( $\pm$ 0.7)	3.9 ( $\pm$ 0.6)	7.8 ( $\pm$ 0.8)	8.6 ( $\pm$ 1.1)
268	3.5 ( $\pm$ 0.8)			
263	4.3 ( $\pm$ 0.7)	2.0 ( $\pm$ 0.4)		
252	6.0 ( $\pm$ 1.1)		4.6 ( $\pm$ 0.9)	3.5 ( $\pm$ 0.8)

After conducting EXSY-NMR experiments at 298 K, we sought to measure the energy barrier to the water-to-urea chemical exchange. For each  $w_0$  value, 10, 15 and 20, we measured EXSY-NMR experiments over a range of temperatures for bulk aqueous urea (2 M) to construct an Arrhenius plot. After collecting the  $k_1$  exchange constant at these varying temperatures, we used the Arrhenius equation to extract  $E_A$  as shown in figure 2.6. Each point on the Arrhenius plot represents the average  $k_1$  exchange constant collected from three experiments.

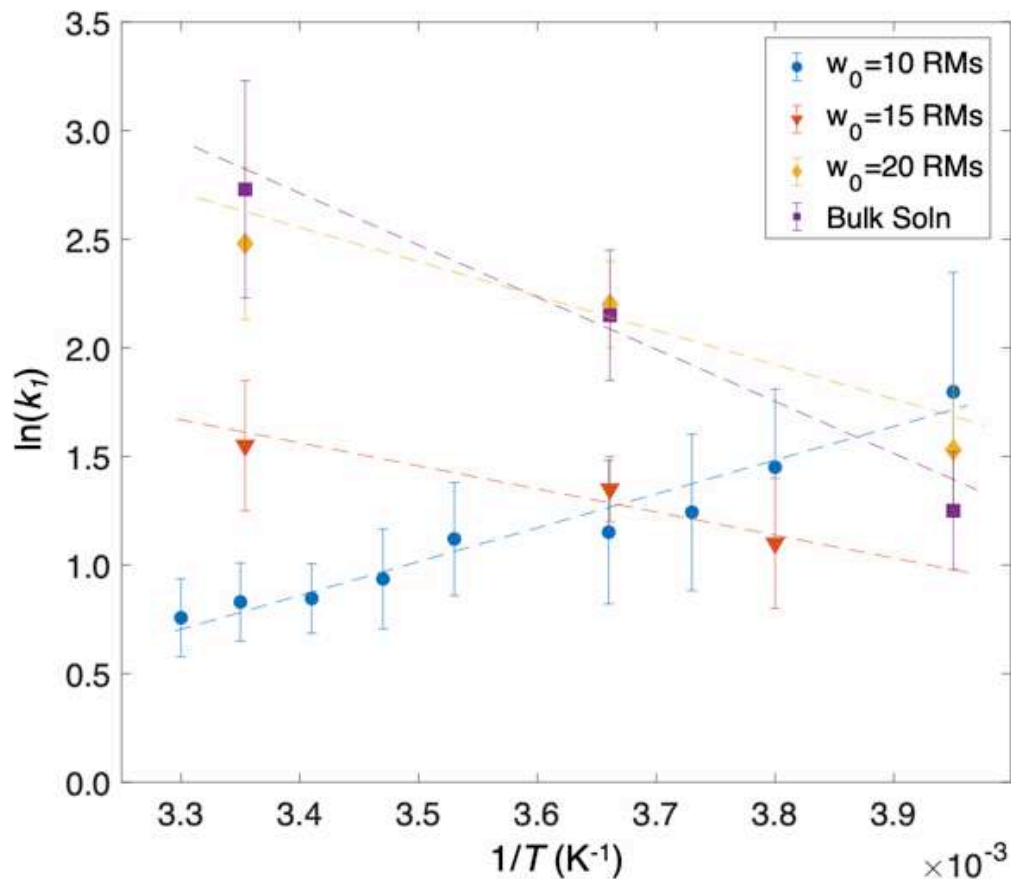


**Figure 2.6:** Arrhenius plots showing the hydrogen atom exchange rates between water and urea as a function of inverse temperature for AOT reverse micelles with  $w_0 = 10$  (blue), 15 (orange), 20 (gold) and bulk solution (purple). Dashed lines represent linear fits to the data. Error bars represent the standard deviation from three measurements of the same sample.

Activation energy values are provided in table 2.2. The measured activation energies of exchange between water and urea are highest for bulk aqueous urea solution and decrease as reverse micelle size decreases.

**Table 2.2:** Activation energy values obtained from Arrhenius plots ( $\ln k_1$  as a function of  $1/T$ ). Reported error was calculated from the error in slope of the linear fit. The apparent negative  $E_A$  value marked with an asterisk (\*) is interpreted in the discussion section.

$w_0$ value	$E_A$ (kJ/mol)
10	-12.4 ( $\pm 1.9$ )*
15	7.6 ( $\pm 1.9$ )
20	12.9 ( $\pm 3.6$ )
Bulk 2 M urea	20.0 ( $\pm 2.5$ )

## 2.6 Disruption of Typical Surfactant Assembly

The proximity of urea molecules to the AOT headgroups at 273 K in the  $w_0=10$  reverse micelles, as indicated by the 2D  $^1\text{H}$ -NOESY data, could cause an increase in the apparent surface area of the surfactant interface. The tight intercalation of the urea molecules with the AOT headgroups could cause the largely cone shaped geometry of the AOT surfactant molecules to become more cylindrical as the nested urea molecules create more bulk at the headgroup. This additional girth at the headgroup region could lead to an increased overall reverse micelle volume. This change in geometry is modeled in figure 2.7, which demonstrates how overlap of cone shaped surfactant cylinders forces the expansion of a larger overall water pool. Additionally, we note that analysis of particles by DLS assumes a relatively spherical geometry, which is almost certainly a simplification of the true reverse micelle shape at any instant in time.<sup>92</sup> It is likely that the larger average apparent hydrodynamic radius measured at lower temperatures indicates a change in morphology that does not perfectly scale with a spherical geometry and would also account for the vast increase in polydispersity.

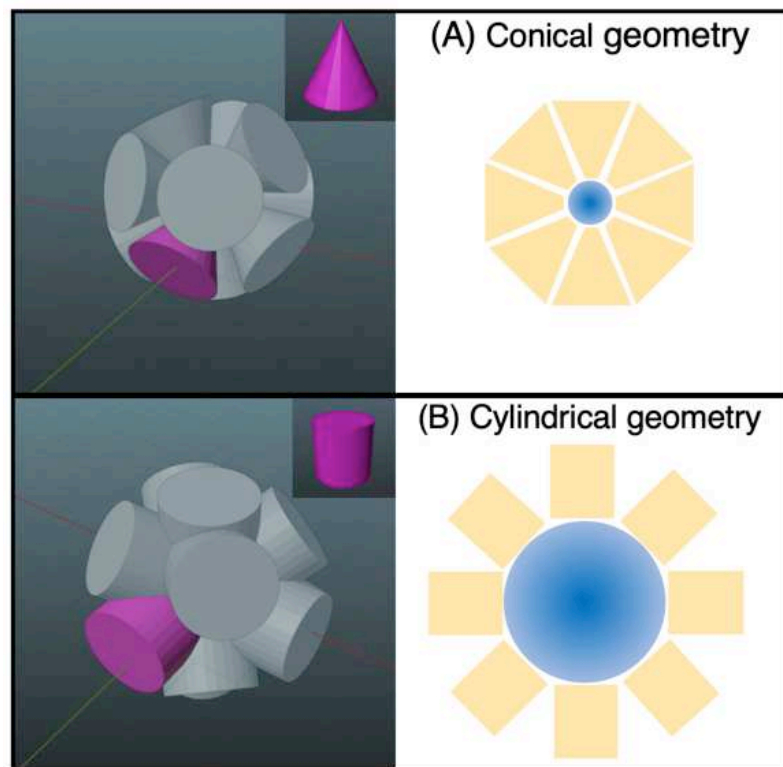


**Figure 2.7:** 2D and 3D models representing the AOT surfactant molecule as **(A)** cones and **(B)** cylinders. The cone shaped geometry permits tight packing of the surfactant around a small inner volume. However, as the 3D model in the bottom left shows, a switch to cylinders of the same height would create overlap that is physically impossible and therefore results in an expanded inner water pool as shown in the 2D illustration.

The EXSY-NMR data collected can provide a measure of the relative number of urea molecules exchanging protons with water. If urea molecules insert between the AOT headgroups at low temperatures such that the NH moieties interact with AOT headgroup protons as indicated by the 2D  $^1\text{H}$ -NOESY NMR (see figure 2.2A and figure 2.2B), then those NH groups would not be available to exchange with water molecules and would decrease the pool of urea molecules available for exchange. This should depress the overall area of the urea peak relative to the water peak observed in the EXSY-NMR spectra. Because these embedded urea molecules no longer participate exchange, they are not detected by the EXSY-NMR experiment. To provide quantitative evidence to support this hypothesis, we evaluate the ratio of the integrated urea peak

to the water peak intensity in the EXSY-NMR spectra. A low urea to water peak intensity ratio indicates less urea available for exchange; a high urea to water ratio indicates more urea available for exchange. Table 2.3 presents a summary of this ratio analysis with the standard deviations provided calculated from the residual errors in line fitting.

With a fraction of the urea molecules removed from the exchange process, only the urea molecules remaining in the water pool will exchange with water. With a much larger water pool, the urea molecules could access a more bulklike environment leading the exchange rate we measure to increase with decreasing temperature. The water pool for  $w_0 = 10$  reverse micelles grows as a fraction of the urea molecules embed in the interface, therefore providing a larger water pool for urea molecules remaining water environment. The urea molecules remaining in the water pool display a faster exchange rate.

Table 2.3 shows that the ratio of the EXSY NMR peak intensity for urea to water is consistently larger at 298 K than it is at 273 K for all  $w_0$  sizes at a mixing time of 1.0 s. This indicates more hydrogen exchange between water and urea is occurring at higher temperatures. For  $w_0 = 10$  reverse micelles the ratio of urea peak intensity to water peak intensity at 273 K decreases by more than a factor of ten, supporting our hypothesis that significantly less urea is available for hydrogen exchange. The values indicated in table 3 also demonstrate that although  $k_1$  and  $k_2$  vary across the different  $w_0$  sizes, the urea-to-water peak ratios at maximum intensity are nearly identical. This confirms that any interference from the instantaneous rate of exchange does not arise from the kinetic behavior of the system as a whole.

**Table 2.3.** Ratio of urea peak integrated intensity to water peak integrated intensity from EXSY-NMR measurements determined at a mixing time of 1.0 s for AOT reverse micelles containing 1:30 urea:water as a function of  $w_0$  and temperature. Ratios represent an average over the EXSY-NMR mixing times associated with the highest intensities where exchange occurs with highest probability. Standard deviations provided in parentheses.

$w_0$ value	urea:water peak intensity ratio	
	298 K	273 K
10	0.10 ( $\pm 0.012$ )	0.009 ( $\pm 0.0014$ )
15	0.11 ( $\pm 0.012$ )	0.032 ( $\pm 0.0046$ )
20	0.10 ( $\pm 0.012$ )	0.029 ( $\pm 0.0042$ )

Our interpretation of urea insertion into the AOT reverse micelle interface is also consistent with the observation of cross peaks in the 2D  $^1\text{H}$ -NOESY NMR spectra that indicate urea has inserted itself into the interfacial region amongst the AOT surfactant headgroups. In contrast, for  $w_0 = 15$  and 20 reverse micelles the ratio in the integral of urea to water EXSY-NMR peaks decreases by only a factor of  $\sim 3$  as temperature drops from 298 K to 273 K. Lower temperatures also result in a lower S/N ratio; this adds uncertainty to the smaller urea peak more than the consistently intense water peak. However, the residual values shown in table S2.2 demonstrate that highly accurate integrations were still obtained. It is possible that the urea molecules begin to embed in the interface as temperature drops for all reverse micelle samples measured; this could account for the slight increase in size observed for  $w_0 = 15$  and 20 reverse micelles at lower temperatures. In this case, we might expect to observe cross peaks between the AOT headgroups and urea in the 2D  $^1\text{H}$ -NOESY spectra collected at low temperatures for  $w_0 = 15$  and 20, but spectra show no hint of this interaction in these systems.

However, low S/N would likely preclude the small signals from observation in the low temperature 2D NOESY spectra. Most critically, comparing the much more dramatic decrease of the urea-to-water peak ratio for the  $w_0 = 10$  reverse micelles at low temperatures to the other  $w_0 = 15$  and  $20$  reverse micelles further supports our proposition that the higher exchange rates we measure at low temperatures for the  $w_0 = 10$  reverse micelles is caused by urea molecules residing in the water pool available for enhanced exchange while many embed in the interface where they do not exchange.

Another explanation for an increased exchange rate could be from a change in intramicellar pH. At high and low pH values, the concerted H atom exchange mechanism prevalent near neutral pH changes to a charge transfer mechanism, which can be orders of magnitude faster.<sup>25</sup> Previous studies have hypothesized that if the pH of the aqueous phase in AOT reverse micelles diverges from neutral, the interfacial region can be significantly more acidic or basic than the water core.<sup>93</sup> If urea affects the intramicellar pH and it resides at the interface, we might expect faster exchange to occur. However, when the charge transfer mechanism is active, it also affects the NMR spectrum, pulling urea and water peaks nearer to each other and eventually merging these peaks.<sup>94</sup> Though we do not observe merging peaks, the apparent rate constants we measure agree well with water-urea proton exchange studies reported by Stabinska *et al.* using water exchange (WEX) NMR spectroscopy. They measured both acid and base catalyzed exchange rates for aqueous urea solutions but could not measure exchange for the concerted mechanism. Their findings suggest that cooling the temperature of  $w_0 = 10$  reverse micelles and therefore destabilizing the nanostructure of the enclosed space may be akin to titrating pH so that exchange becomes acid or base catalyzed.<sup>95</sup>

A change from concerted to an acid/base catalyzed mechanism could also account for the decreasing values of  $E_A$  from bulk aqueous solution to the reverse micelles. However, this mechanism does not explain the increasing rates observed with decreasing temperature or the larger sizes measured for all reverse micelles as a function of temperature. Our results demonstrate urea's destabilizing effect observed in other studies that involve more complex biological environments. For instance, urea's disruption of AOT reverse micelle aggregation shares similarities with observation of denaturation of a bovine serum albumin begins when urea localized at the protein surface leads to a repulsion between urea and charged residues.<sup>96</sup> It appears that the urea in our AOT reverse micelle systems follows a similar pattern of localization at a surface that can initiate significant structural changes.

## 2.7 Conclusions

Experiments showed that restriction to nano-sized reverse micelles has a modest effect on hydrogen exchange behavior between water and urea relative to bulk behavior. However, the experiments demonstrate that small reverse micelle values,  $w_0=10$ , at low temperatures show significant differences in the interaction of urea with the surfactant interface leading to dramatic changes in the reverse micelle size. Specifically, urea appears to embed itself into the interfacial area in  $w_0=10$  reverse micelles at temperatures at and below water's freezing temperature.

This dramatically enlarges the reverse micelle apparent hydrodynamic diameter and allows the remaining urea molecules in the reverse micelle water core to display bulklike exchange behavior because all the urea molecules that are exchanging experience a large intramicellar water pool. This effect was not observed for larger  $w_0=15$  or 20 sizes. These results may have important biomedical implications because they indicate unique urea interactions

could occur within the confined environment of cellular mitochondria. Closer examination of single hydrogen transfer may help elucidate the mechanisms fundamental to physiological homeostasis.

### 3.1. Introduction

The project outlined in this section was jointly conducted by Ernestas Gaidamauskas and Ataf Ali Altaf, students of collaborator and PI Debbie C. Crans. The NMR data contributions are explicitly credited in the appropriate sections and Appendix 4. A final manuscript is in progress, which we plan to submit to the Journal of the American Chemical Society.

The initial aim of the project was to use reverse micelles loaded with NaF to use the  $\text{F}^-$  ion to indicate ionic strength in AOT based reverse micelles. The presence of ions in liquid solution can modulate the structure and reactivity of biomolecules with important roles in chemical and life sciences.<sup>97,98</sup> In solution, ionic strength is defined in EQN 7:

$$I = \frac{1}{2} \sum_i c_i z_i^2 \quad (7)$$

where  $c_i$  is the concentration of the charged species and  $z_i$  is the charge of that species. Ionic strength can strongly influence chemistry occurring in aqueous systems.<sup>99-102</sup> Measurement of ionic strength in bulk solution is quite routine using electrochemical methods, yet the measurement, and even the concept, of ionic strength in nanoscale environments presents a significant challenge. Here we utilize  $^{19}\text{F}$  NMR spectroscopy of the fluoride ion,  $\text{F}^-$ , as a method to measure ionic strength *in situ* within the nanoconfined environments of reverse micelles. When restricted to minuscule proportions, the location and impact of ions can play a strong role in the chemistry occurring and can mediate that chemistry.<sup>103-105</sup> Reverse micelles are self-assembled droplets of polar solvent stabilized in nonpolar solvent by amphiphile. They present a commonly used and easily prepared way to create nanoconfined environments.<sup>1,91,106-108</sup> They have also been used as models for biological systems.<sup>109,110</sup> For this study, we prepared reverse

micelles using the most commonly used surfactant , AOT ((bis-(2-ethylhexyl) sulfosuccinate sodium salt).

### 3.1.1 Implications of Ionic Headgroups

Simulations of AOT reverse micelles predict that counterions reside near the negatively charged surfactant headgroups.<sup>111</sup> The ions reside largely at the interface due both to Coulombic attraction with the sulfonate headgroup but also because the minuscule amount of water within the reverse micelles cannot screen charges from multiple cations from each other within the reverse micelle water core.<sup>112-114</sup> This can be interpreted in terms of the Debye screening length,<sup>115</sup> which describes how far the electrostatic effect of a charge persists in solution. The Debye length is defined in EQN 8:

$$\kappa^{-1} = \sqrt{\frac{\epsilon_0 \epsilon_r k_B T}{2N_A e^2 I}} \quad (8)$$

where  $\epsilon_0$  is the permittivity of free space,  $\epsilon_r$  is the dielectric constant,  $k_B$  is the Boltzmann constant,  $T$  is the temperature (K),  $N_A$  is Avogadro's number,  $e^2$  is the elementary charge squared, and  $I$  is the ionic strength of the solution. For short Debye distances, the electrostatic effect of ions in solution does not extend far into the solution. A larger calculated Debye distance means that an ion's effects are felt farther away from the ion in solution. The Debye length in a 1.0 M ionic strength solution is approximately  $\kappa^{-1} \sim 0.3$  nm.<sup>116</sup> Thus, the concept of ionic strength in a reverse micelle presents a conundrum as the interior water pool has a similar dimension to the screening length. Indeed, the presence of additional ions in the reverse micelle interior has been shown to contract the reverse micelle size.<sup>117,118</sup> Although simulations predict a preponderance of surfactant counterions residing at the inner interface of the reverse micelles, and time-resolved

IR studies show evidence for bulk-like water that develops in AOT reverse micelles with increasing size suggesting that ions are at the interface,<sup>119</sup> no experimental measurement has confirmed this hypothesis nor measured the ionic strength inside the reverse micelles.

### 3.1.2 Fluorine NMR Spectroscopy

The diamagnetic nucleus of the fluoride ion,  $^{19}\text{F}^-$ , makes it a sensitive reporter of its environment.<sup>120,121</sup> For example, slight temperature changes of only a few degrees Celsius cause  $^{19}\text{F}^-$  chemical shifts to vary several ppm,<sup>122,123</sup>  $\text{F}^-$  also displays exquisite sensitivity to ionic strength of aqueous solutions, which suggests its utility as a probe of ionic strength.<sup>124</sup> Here, we report  $^{19}\text{F}$  NMR spectroscopy of the fluoride ion in AOT reverse micelles to measure the intramicellar ionic strength and also investigate if ionic strength is changed in reverse micelles prepared with the nonionic surfactant, Igepal CO-520 (Figure 3.1).

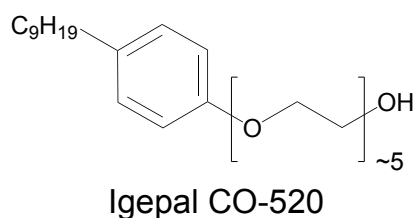


**Figure 3.1:** Chemical structure of Igepal CO-520

AOT contains a sulfate headgroup with a sodium anion, and introducing the  $\text{F}^-$  into AOT reverse micelles reports its local environment through peak position in the  $^{19}\text{F}$  NMR spectra. We measure the ionic strength as a function of reverse micelle size ( $w_0$ ) and compare results to bulk aqueous solution. We also follow the  $^1\text{H}$  NMR signal of water in the reverse micelles and correlate the  $\text{F}^-$  and  $\text{H}_2\text{O}$  signals to understand the role of water in the reverse micelles. In large AOT reverse micelles, the ionic strength appears similar to bulk water but as reverse micelle size

decreases below  $w_0 < 10$ , the ionic strength increases. For the smallest AOT reverse micelles measured, the ionic strength appears much higher than we can achieve in bulk aqueous solution.

## 3.2 Preparation of the Reverse Micelle System

### 3.2.1 Materials

Reagent grade NaF, NaNO<sub>3</sub>, NaBr, Na<sub>2</sub>SO<sub>4</sub> and isooctane (2,2,4-trimethylpentane) were purchased from Sigma-Aldrich Chemical Co. and used without further purification. AOT (bis-(2-ethylhexyl) sulfosuccinate sodium salt, supplier?) was purified to remove an acidic contaminant as described previously.<sup>125</sup> Deuterium oxide (Cambridge Isotope Laboratories, 99.9%), NaOD (Merck & Co., 98 atom %D), cyclohexane (Aldrich, anhydrous, 99.5%), igepal CO-520 (Merck & Co.), and DCl (Sigma Aldrich, 99.5 atom % D) were used as received. Deionized water (17.9 MΩ·cm) was used to prepare all aqueous solutions.

### 3.2.2 Stock solutions and Sample Preparation

Stock solutions of sodium fluoride (NaF) in H<sub>2</sub>O (or in D<sub>2</sub>O) were prepared at the indicated salt concentration. To prepare concentrated stock solutions of NaNO<sub>3</sub>, NaBr, and Na<sub>2</sub>SO<sub>4</sub>, solutions were heated until solids completely dissolved. After cooling to ambient temperature, solutions were further diluted with D<sub>2</sub>O to the desired <sup>19</sup>F<sup>-</sup> and salt concentration (100 or 25 mM). To prepare stock solution with acidic pH, we added DCl and measured pH (Corning 140 pH meter equipped with a combination microelectrode) until the pH remained constant at ambient temperature (300 ± 1 K).

### 3.2.3 Reverse Micelle Solutions

The 0.20 M AOT stock solution was prepared in 2,2,4-trimethylpentane (isooctane) and the 0.3 M Igepal CO-520 stock solution was prepared in cyclohexane. The reverse micelle solutions were prepared in glass vials by mixing of 0.20 M NaF aqueous solution (pH 6.9) and respective surfactant stock solutions. The size of reverse micelles ( $w_0 = [\text{H}_2\text{O}]/[\text{surfactant}]$ ) was controlled by the ratio of 0.20 M NaF aqueous solution and the concentration of surfactant solution in isooctane. After mixing, samples were vortexed in closed vials until clear solutions were obtained, ensuring the formation of reverse micelles. If phase separation occurred, samples were gently warmed until a single clear phase was observed and cooled back to room temperature. Only clear and non-opalescent solutions were used for NMR spectroscopy and DLS.

### 3.2.4 Dynamic Light Scattering (DLS) Experiments

DLS (Malvern Zetasizer ZS, model ZEN3600) measurements were performed on the reverse micelle samples containing  $\text{F}^-$  and the corresponding control samples containing only the millipore filtered water. Prior to data acquisition, samples were equilibrated in the DLS instrument for 90 s at 25 °C. Scans were averaged from 30 scans in backscatter mode (173°).

## 3.3 Chemical Shift and Correlation with Ionic Strength

*The following results presented were collected with the combined efforts of Ernestas Gaidamauskas and Ataf Ali Altaf, former research scientist and student of Debbie C. Crans and collaborators who pioneered this project. They contributed to this work by preparing samples*

*and running samples on the NMR spectrometer. The subsequent figures relating to this part of data collection are also a result of their work.*

Before demonstrating the efficacy of  $^{19}\text{F}^-$  as a probe in nanoconfined environments, data were collected to demonstrate that the  $^{19}\text{F}^-$  is a sensitive probe of ionic strength in bulk aqueous solution. Figure 3.2 shows the  $^{19}\text{F}$  NMR spectra for  $^{19}\text{F}^-$  in a series of bulk aqueous solutions acquired at 25 °C. We measure a  $^{19}\text{F}^-$  chemical shift of 2.9 ppm for a NaF at 0.01 M solution; this marks the fluoride response in a solution with an ionic strength that is essentially zero. All other solutions measured were prepared with 0.2 M NaF. Ionic strength was increased using  $\text{NaNO}_3$ . Adjusting the solution pH to 6.9, far from the  $\text{pK}_a$  value for HF of 3.2,<sup>126</sup> ensures that measurements probed only the signal arising from  $^{19}\text{F}^-$  and not HF. As we increase the ionic strength of an aqueous solution, the  $^{19}\text{F}^-$  peak shifts upfield (towards increasingly negative values), indicating greater shielding of the fluoride ion. At the highest ionic strength that we could attain, 7.0 M, the  $^{19}\text{F}^-$  peak appears at -5.5 ppm, representing an overall change of more than 10 ppm over the ionic strength range measured.

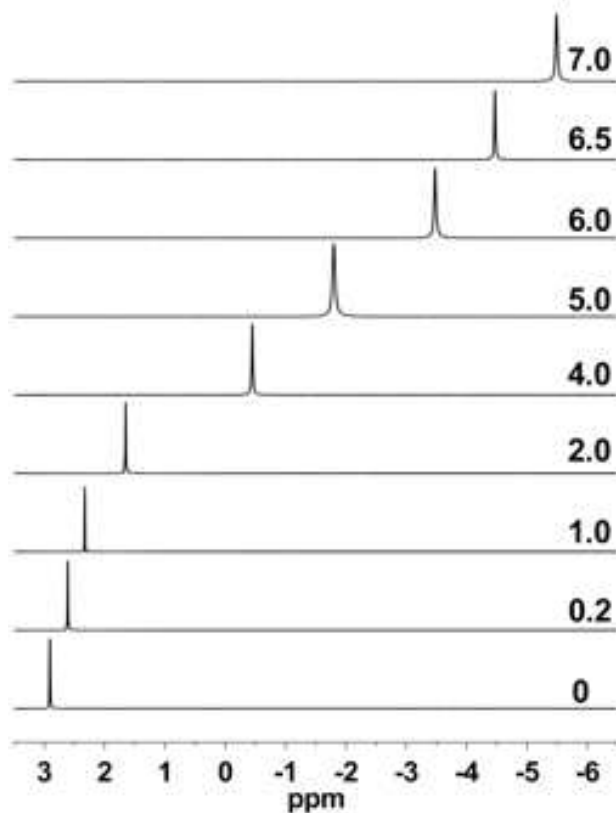


**Figure 3.2:**  $^{19}\text{F}$  NMR spectra of NaF in bulk aqueous  $\text{NaNO}_3$  solution as a function of increasing ionic strength. Numbers to the right side indicate the ionic strength based on the  $\text{NaNO}_3$  molar concentration. Spectra were acquired at  $25\text{ }^\circ\text{C}$  and all solutions prepared to  $\text{pH} = 6.9 \pm 0.1$ . Chemical shifts of the  $^{19}\text{F}^-$  peak were referenced by substitution against the  $0.01\text{ M NaF}$  in  $\text{D}_2\text{O}$  ( $\text{pH} 12.0$ ) without frequency lock.

Additionally, Figure 3.3 shows the resultant  $^{19}\text{F}^-$  chemical shift as ionic strength was adjusted by adding various salts including NaBr,  $\text{NaNO}_3$  and  $\text{Na}_2\text{SO}_4$ . The  $^{19}\text{F}$  NMR chemical shift depends only on the  $\text{Na}^+$  ion concentration. Changing the anion from nitrate to bromide or sulfate (accounting for divalency) has no impact on the  $^{19}\text{F}^-$  chemical shift. These data suggest that we can map out the ionic strength by measuring the  $^{19}\text{F}$  NMR chemical shift of  $^{19}\text{F}^-$  in these solutions.

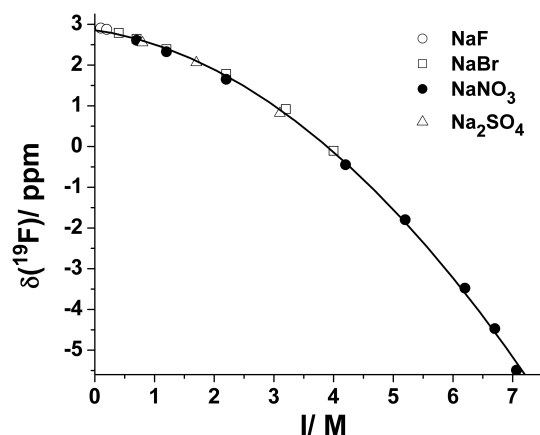


**Figure 3.3:**  $^{19}\text{F}$  NMR chemical shift as a function of  $\text{Na}^+$  ionic strength in aqueous solutions of NaF (○), and NaF binary mixtures with NaBr (□),  $\text{NaNO}_3$  (●), and  $\text{Na}_2\text{SO}_4$  (△). The points have been connected by a line as a guide to the eye. The  $\text{F}^-$  concentration in binary salt mixtures was 0.20 M. The solution pH was  $6.8 \pm 0.3$ .

### 3.4 Behavior of Fluoride Probe in AOT-Reverse Micelle Systems

When we introduce  $^{19}\text{F}^-$  to the AOT reverse micelles, the  $^{19}\text{F}$  NMR chemical shift is similarly responsive, shown in Figure 3.4. Generally, as reverse micelle size, i.e.,  $w_0$  value, decreased, the chemical shift also decreased. Between  $w_0 = 10$  and  $w_0 = 20$ , the chemical shift remains relatively constant at approximately 1.8 ppm. As the reverse micelle size decreases, the chemical shift rapidly decreases to about -9.1 ppm for the smallest reverse micelle measured,  $w_0 = 3$ . This chemical shift value within the smallest reverse micelles appears at a significantly more negative value than -5.5 ppm, which is what we measure for the most concentrated bulk aqueous ionic solutions, 7.0 M.

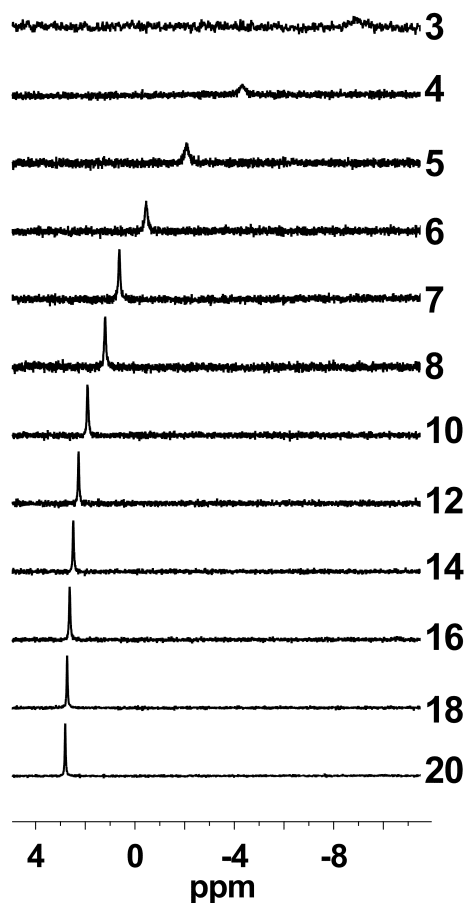


**Figure 3.4:** The  $^{19}\text{F}$  NMR spectra for  $\text{F}^-$  in AOT reverse micellar solutions with various  $w_0$  sizes labeled on right of spectrum. Samples were prepared volumetrically from aqueous 0.2 M NaF solution (pH 6.9) and 0.2 M AOT in isooctane. All spectra were acquired at 25°C. Chemical shift is referenced by substitution against the 0.01 M NaF in  $\text{D}_2\text{O}$  (pH 12.0) without frequency lock.

To compare and contrast trends in bulk aqueous solution and reverse micelles, figure 6 plots both bulk ionic strength (left y-axis) and reverse micelle size, *i.e.*,  $w_0$  (right y-axis), as a function of fluoride chemical shift. Figure 3.5 shows that the chemical shift measured for the largest reverse micelle ( $w_0 = 20$ ) is 2.95 ppm, which is the same value as the  $^{19}\text{F}^-$  chemical shift measured in 0.01 M NaF bulk aqueous solution with no added sodium salt. This suggests that the fluoride ion in the  $w_0 = 20$  reverse micelle senses a similar ionic strength as the bulk aqueous solution conditions at the lowest concentration measured. As shown in figure 3.5, decreasing reverse

micelle size or increasing ionic strength of the bulk aqueous sample each cause a decrease in the  $^{19}\text{F}^-$  chemical shift to increasingly negative values. This graph provides a visual guide to intuit the intramicellar ionic strength. Between  $w_0 = 8$  and 10, the fluoride ion begins to sense ions in its vicinity; by  $w_0=6$ , the local ionic strength is similar to 4 M aqueous  $\text{NaNO}_3$ . The chemical shift of  $^{19}\text{F}^-$  in  $w_0 = 4$  reverse micelles has a peak position similar to a 6.75 M bulk aqueous solution. The maximum concentration of bulk aqueous  $\text{NaNO}_3$  achieved was 7.0 M, where the  $^{19}\text{F}^-$  peak appears at -5.5 ppm. In  $w_0 = 3$  reverse micelles, the chemical shift achieved was even more negative value of -9.1 ppm suggesting an environment with an ionic strength higher than 7.0 M.

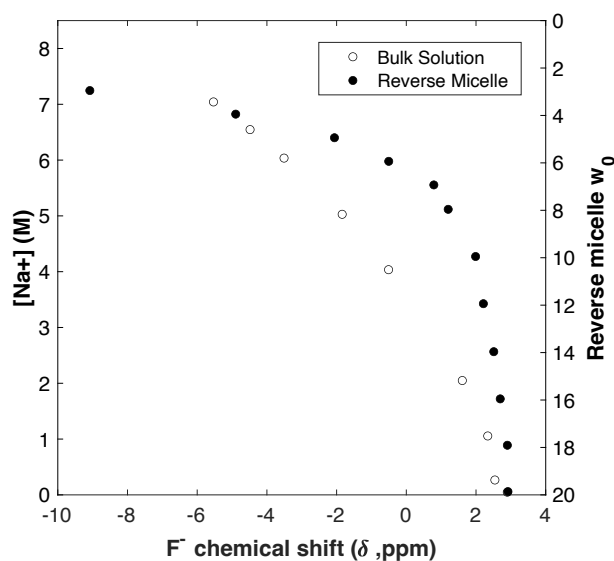


**Figure 3.5:** Comparison of  $^{19}\text{F}$  NMR chemical shift values from bulk aqueous solutions and AOT reverse micelle samples. The left axis refers to bulk aqueous values while right axis reports size values via the  $w_0$  parameter.

### 3.4.1 $^1\text{H}$ NMR of aqueous ionic solutions

We further characterized the AOT reverse micelle samples using  $^1\text{H}$  NMR spectroscopy, particularly the nature of the intramicellar water in reverse micelles prepared with 0.2 M NaF. Sample  $^1\text{H}$  NMR spectra showing the regions of interest appear in the supplementary information (Figure S3.1). The chemical shift for HOD as a function of  $w_0$  shown in figure 3.7 displays a smooth but nonlinear downfield shift from 4.02 ppm for the smallest reverse micelle,  $w_0 = 3$ , to 4.50 ppm for the largest reverse micelle size,  $w_0 = 20$ . In bulk aqueous solution, the HOD chemical shift moves upfield as the NaCl concentration increases.<sup>127</sup>

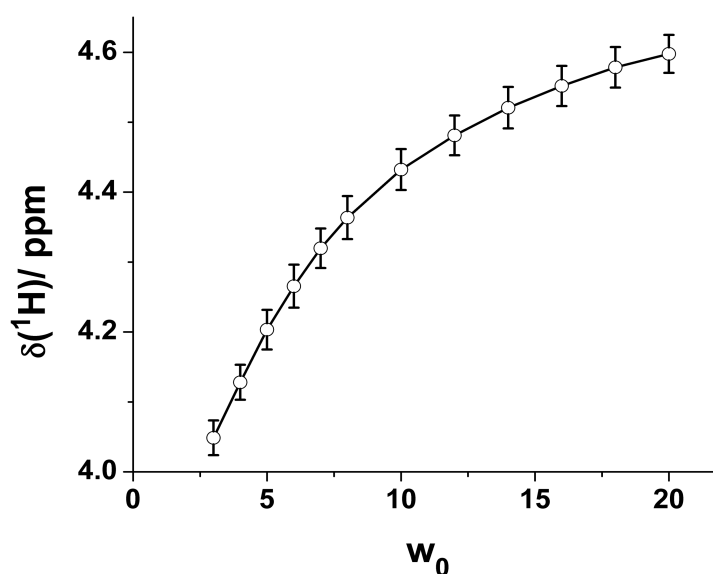


**Figure 3.6:** Water chemical shift as a function of  $w_0$  in AOT reverse micelles prepared with 0.2 M NaF. Samples were prepared from aqueous 0.2 M NaF solution (pH 6.9) and 0.2 M AOT solution in isooctane. Error bars show standard deviation of three replicates.

### 3.4.2 $^{19}\text{F}$ NMR of nonionic reverse micelles

To explore the role of the added NaF to the reverse micelles, we also measured  $^{19}\text{F}$  NMR chemical shifts in reverse micelles prepared with the nonionic surfactant igepal CO-520. Figure

3.7 reports the  $^{19}\text{F}$  NMR chemical shift observed for 0.2 M NaF in igepal CO-520 reverse micelles in comparison with the trend for AOT reverse micelles. For larger igepal CO-520 reverse micelles,  $w_0 = 10 - 20$ , the chemical shift remains constant within 0.1 ppm. Below  $w_0 = 10$ , the  $^{19}\text{F}$  NMR chemical shift decreases but significantly less than observed in AOT reverse micelles, and never reaching negative values. The decreased chemical shift value for igepal CO-520 reverse micelles  $w_0 < 10$  reports the effect of confinement on the NaF introduced into the system, which is minuscule compared to the effect of the ions present at the inner surface of AOT reverse micelles.

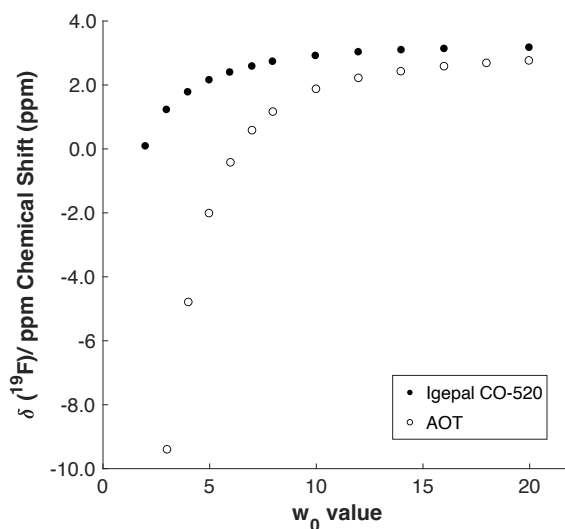


**Figure 3.7:** Comparing the chemical shift of  $^{19}\text{F}^-$  is shown as a function of  $w_0$  in both igepal CO-520 RM solutions (●) and AOT RM solutions (○). Samples were prepared from aqueous 0.2 M NaF solution (pH 6.9), and 0.3 M igepal CO-520 solution in cyclohexane, and 0.2 M AOT solution in isoctane.

### 3.4.3 Impact of ionic strength on AOT reverse micelle size

Because preparing reverse micelles with solutions of high ionic strength has been demonstrated to affect reverse micelle particle size,<sup>117,124</sup> we measured the AOT reverse micelle particle sizes prepared with water and with 0.2 M NaF using dynamic light scattering (DLS)

shown in Figure 3.8. For  $w_0 \leq 3$  reverse micelles the presence of  $^{19}\text{F}^-$  appears to have no impact on the resulting hydrodynamic radius. However, the presence of  $^{19}\text{F}^-$  causes the hydrodynamic radius to begin to diverge at  $w_0 = 4$  from comparably prepared reverse micelles with just water. At  $w_0 = 8$ , the size of the reverse micelles as a function of  $w_0$  becomes significantly less dramatic, appearing to almost plateau compared to the reverse micelles containing water. The size difference is similar to observations when salts are added to AOT reverse micelles.<sup>117,124</sup>

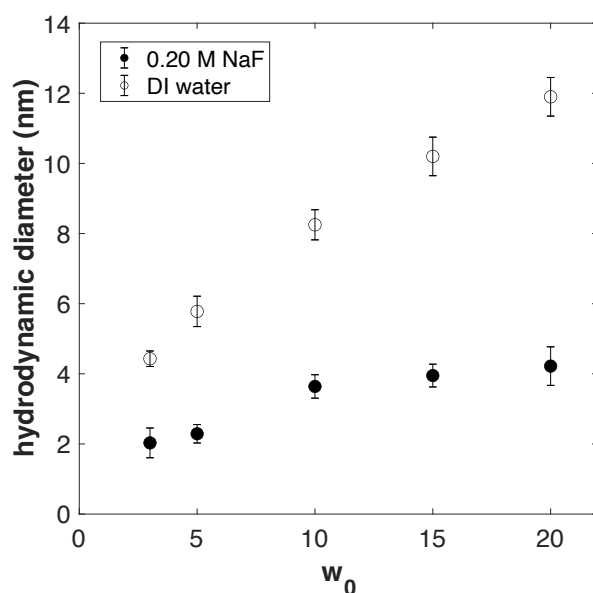


**Figure 3.8:** The hydrodynamic diameter of reverse micelles in 0.20 M AOT in isoctane is shown as a function of  $w_0$ . The reverse micelle solutions were prepared from DI water (○), and aqueous 0.20 M NaF solution (●). Errors shown are standard deviations of three measurements.

### 3.5 Behavior of Fluoride Probe in alternate igepal CO-520 reverse micelles

When  $^{19}\text{F}^-$  is introduced to reverse micelles made from igepal CO-520, we also observe a shift in the  $^{19}\text{F}$  NMR chemical shift that resembles the trend plotted for AOT reverse micelles (Figure 3.9a). Once again, as  $w_0$  value decreased, the chemical shift also decreased. Between  $w_0 = 10$  and  $w_0 = 20$ , the chemical shift did not deviate beyond 0.1 ppm. Below  $w_0 = 10$ , the  $^{19}\text{F}$  NMR

chemical shift decreased but did not reach negative values. The change in chemical shift of water with varying ionic strength in the Igepal CO-520 reverse micelles measured by  $^1\text{H}$  NMR spectroscopy occurred over a similar range to the AOT reverse micelles, approximately 0.6 ppm, but this range occurred more downfield, from approximately 4.4 ppm to 4.8 ppm rather than 4.0 ppm to 4.6 ppm (Figure 3.9b). Sample  $^1\text{H}$  NMR spectra showing the peaks of interest for the Igepal CO-520 reverse micelles may be found in the Appendix (figure S3.1).

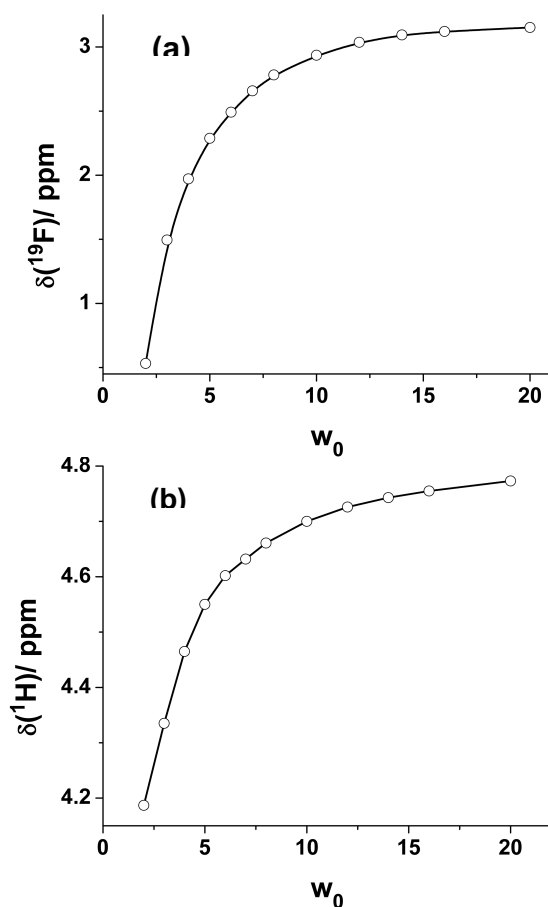


**Figure 3.9:** a) The chemical shift of  $\text{F}^-$  is shown as a function of  $w_0$  in Igepal CO-520 RM solutions. Samples were prepared from aqueous 0.2 M NaF solution (pH 6.9), and 0.3 M Igepal CO-520 solution in cyclohexane. b) The chemical shift of water in reverse micelles as a function of  $w_0$ . Samples were prepared from aqueous 0.2 M NaF solution (pH 6.9), and 0.3 M Igepal CO-520 RM solution in cyclohexane.

### 3.6 Nanoconfinement's Impact on Ionic Strength

The most remarkable observation of this study is that the  $^{19}\text{F}$  NMR spectroscopy of fluoride introduced into AOT reverse micelles mirrors the effect of increasing ionic strength with sodium salts in bulk aqueous solutions. In the largest reverse micelles prepared, the  $^{19}\text{F}$  NMR chemical shift of the fluoride ion indicates an environment near the fluoride ion with low ionic strength despite the significant presence of ions at the nearby surfactant interface. For reverse micelles with  $w_0 > 10$ , the fluoride ion senses an environment like that of bulk water in the absence of ions. The water pool in the reverse micelle with  $w_0 > 10$  is sufficient to screen the fluoride ion from the presence of ions in the reverse micelle interior. This suggests that the fluoride resides at or near the center of the reverse micelle water pool. Similarities between the  $^{19}\text{F}$  NMR chemical shift of the fluoride ion in AOT and in igepal CO-520 reverse micelles indicates well developed water pools in both systems.<sup>128</sup> As the reverse micelles decrease in size, the fluoride  $^{19}\text{F}$  NMR chemical shift reports increasing presence of ions. In AOT reverse micelles, the fluoride is close enough to become sensitive to the surfactant ions for  $w_0 < 10$  reverse micelles, reporting an ionic strength  $> 2$  M. To achieve a similar result in igepal CO-520 reverse micelles requires substantially lower water content,  $w_0 = 5$ . These results show that the fluoride ion provides an effective way to measure intramicellar ionic strength.

The nanosized reverse micelle environment can present an ionic strength higher than we could attain in bulk aqueous solution. The environment in the smallest sized AOT reverse micelles thus presents a very high ionic strength. Interestingly, in reverse micelles prepared with the nonionic igepal CO-520 surfactant, we observe a fluoride chemical shift consistent with a concentration between 1-2 M, an order of magnitude higher than the solution from which the reverse micelles were prepared, 0.2 M. This suggests that both  $\text{Na}^+$  and  $\text{F}^-$  ions are confined to

the reverse micelle and that the small extent of the reverse micelle interior causes the fluoride to sense its partner sodium ion in close proximity.

Importantly, results presented here demonstrate that the ions associated with AOT remain largely bound to the reverse micelle inner interface. This is consistent with the work of Piletic, *et al.*, who report that in  $w_0=10$  reverse micelles, with  $\sim 4$  nm diameter, approximately half of the water in interacts with the interface and the rest forms a bulk-like water core.<sup>119</sup> In the interior of small reverse micelles, the counterions at the interface are within a Debye radius. Therefore, conventional prediction would suggest a resultant high ionic strength. We calculate a Debye radius of 0.3 nm for a 1.0 M solution of NaF in H<sub>2</sub>O. If we adjust this calculation to reflect the concentration of NaF used in his study, the Debye radius shortens to 0.06 nm. The shortened Debye radius suggests less shielding of the charged surface from the bulk water pool.

### *3.6.1 Implications in Colloidal, Fuel Cell and Battery Chemistry*

If the core of the reverse micelle is in fact relatively devoid of ions as suggested by results reported here, this has important implications in colloidal chemistry and nanoparticle synthesis. Literature experiments have shown that microstructures found within the microemulsions used to synthesize metal organic frameworks (MOFs) directly controlled the resultant morphology of the MOF.<sup>129</sup> This tunability is critical tune MOFs to their eventual applications like gas storage and separation, sensing, and targeted catalysis.<sup>130</sup> Chemists have already found that salinity is a key part of nanoparticle synthesis,<sup>131</sup> and our results suggest that chemists could utilize a fluoride probe to measure the approximate size of a synthesized batch of nanoparticles to avoid more costly forms of analysis like TEM or SEM.

The measured ionic strength as well as trends in chemical shift suggest that an ion gradient occurs in these nanoconfined spaces. The uneven distribution of ions throughout the pocket has implications in ion mobility, a key consideration in battery chemistry.<sup>132,133</sup> Our findings may open new possibilities for exploiting the well-known properties of Nafion, a commercially widespread choice for a membrane material that facilitates hydrogen transport in fuel cells, sensors, batteries, metal-ion recovery, and other electrochemical devices.<sup>134,135</sup> Consisting of a Teflon backbone with a sulfonated pendant group, Nafion's was initially modeled as a cluster channel where sulfonated ion clusters formed a fluorocarbon lattice that explained its transport properties.<sup>136</sup>

Nafion closely resembles our AOT reverse micelles; both have sulfonate headgroups with sodium counterions that interact with an associated water pool.<sup>137</sup> The data we present provides a targeted approach to measuring localized ion concentrations within the confined spaces of the Nafion films using <sup>19</sup>F NMR spectroscopy. Moreover, our technique is especially useful to Nafion systems since our measurements are carried out in reverse micelles of known hydrodynamic diameter, allowing relationships to be drawn between water pool size and ionic strength. Previous studies in the Nafion literature have noted variability in the molecular weight of a Nafion unit,<sup>136</sup> resulting in assembled structures whose sizes and shape are difficult to precisely characterize. Again, our study fills a critical gap in knowledge because our reverse micelle model system can be used extrapolate the size of Nafion units based on chemical shift data.

More recently, in 2019, Saito *et al.* showed increased tortuosity in the path of a mobile cation in a polypropylene pore decreases ion mobility and thus resulting in decreased battery performance.<sup>138</sup> Although the pore diameters tested by Saito (0.5  $\mu\text{m}$ ) exceed the diameters of

the reverse micelles used here, our results suggest that engineering battery materials with nanosized spaces for ion storage could increase the achievable concentration of ions in miniaturized devices. This would aid in the efficient intercalation in and out of a battery material due to the more dramatic charge gradient present.

### *3.6.2 Implications in Biological Interfaces*

The concentrated presence of ions at the interface resembles numerous biological cases such as neuron polarization during the process of signal conduction in the nervous system or the accumulated charge separation formed during cellular respiration across the mitochondrial matrix.<sup>139</sup> By conducting experiments with surfactants with both an ionic headgroup (AOT) and a nonionic headgroup (Igepal CO-520), we demonstrate the tendency to create a localized charge gradient near the interface within the reverse is not simply a result of an ionic surfactant. Rather, we again point to another example of how nanoconfined environments affect the properties of water.<sup>91,140,141</sup>

## **3.7 Conclusions**

In addition to showing that <sup>19</sup>F NMR spectroscopy can be used to measure ionic strength, we also show confining water in nanosized reverse micelles can achieve ionic strengths higher than what is possible in conventional bulk solutions. By using the <sup>19</sup>F<sup>-</sup> chemical shift as an indicator of the local environment inside the reverse micelles, we demonstrate the extended use of <sup>19</sup>F NMR for applications outside protein conformations, dynamics, and ligand interactions. Additionally, due to the ease of reverse micelle preparation, we demonstrate a convenient way to

evaluate ion gradients, which can be spatially mapped using the fluoride ion, in commercially relevant materials such as Nafion.

## CHAPTER 4: CHARACTERIZING NOVEL SURFACTANTS

### 4.1 Introduction

This project was undertaken with the joint instruction of PI Nancy Levinger and Dr. David Osborne. Dr. Osborne approached our group with a collaboration proposal based on his preliminary measurements of the approximate Krafft temperature of the two surfactants later discussed in this chapter.

Surfactant molecules are of widespread interest because of their ability to reduce the surface tension of a liquid, especially water.<sup>142</sup> Surfactants are amphiphilic molecules with both hydrophobic and hydrophilic properties.<sup>143</sup> The hydrophilic head and hydrophobic tail makes it an ideal compound to sit at the interface of an oil and water interface. Surfactant headgroups may be charged, eliciting the characterization of that molecule an ionic surfactant with an associated counterion. Depending on the stability of the mixture, they may be termed emulsions or microemulsions, which implies a thermodynamically stable system. Emulsions and microemulsion systems are subject to intense study since they form a variety of structures to prevent the contact of the hydrophilic and hydrophobic (water and oil, respectively) phases.<sup>144</sup> The size of the resultant structures are generally on the nanometer scale, and therefore remain clear and transparent. The simplest of structures usually formed are termed micelles, which are roughly spherical droplets of oil in water or reverse micelles which are roughly spherical droplets of water in oil. Characterizing surfactant behavior in water is a crucial step to their use in a host of applications such as cosmetics and ointments,<sup>145-149</sup> drug delivery,<sup>150</sup> and pharmacology.<sup>151,152</sup>

## 4.2 Ideal Surfactant Characteristics in Cosmetics

The cosmetics industry takes interest in four key uses of surfactants: cleansing, emulsification, solubilization, and conditioning (Table 4.1).<sup>151</sup> Useful properties of common surfactants are also herein discussed in the following sections:

**Table 4.1:** Examples of common surfactants incorporated into consumer goods

Surfactant	Purpose
Sodium lauryl sulfate (SLS), (Ammonium lauryl sulfate (ALS)	Cleansers, foaming agents
Sodium stearate	Soap
Stearic acid	Deodorants, antiperspirants
Cetyl alcohol and stearyl alcohol	Thickening agent
Cetrimonium chloride	Hair conditioners
Sodium Lauriminodipropionate Disodium Lauroamphodiacetate	Cleansing agent for sensitive skin
Cocamidopropylamine oxide	Foaming agent
Polysorbate ester	Solubilizing agent

### 4.2.1 Cleansers

Surfactants are effective cleansers because they help suspend oily material in water. Applying an aqueous solution of surfactant solution will help the oil material migrate to the center of the water-filled micelle and therefore draw it away from hair or skin surfaces.<sup>142</sup> Certain surfactants also help to create foam, which forms as a result of trapped air. This bubbling effect is generally expected by consumers as an indicator of effectivity, though foaming is not related to the ability of a product to clean.

#### *4.2.2 Emulsifiers*

While some cosmetics are meant to remove oil or other small particles, other products are meant to add oily materials, *e.g.* lotions or moisturizers. Emulsifiers can also help blend and stabilize complex formulations so it remains on the skin long enough to be absorbed.

#### *4.2.3 Solubilizers*

Emulsions may sometimes produce opaque solutions that need to reach commercial shelves as clear solutions. Using surfactants that spontaneously solubilize oils in nanoscale droplets are ideal for this application. Solubilizing fragrances or other organic ingredients into formulations makes surfactants critical.

#### *4.2.4 Conditioners*

Surfactants are naturally discussed in relation to the two different hydrophilic and hydrophobic phases they join. Surfactants act as conditioners because their oily component improves the look and feel of skin and hair surfaces.<sup>153</sup> To be effective and desirable, the surfactant needs to be partially left behind and non-irritating. Cetyl alcohol, a common surfactant incorporated for its conditioning properties, clings to hair or skin through static attraction. Its slight positive charge attracts the slight negative charge of hair or skin.<sup>154</sup>

#### *4.2.5 Other Special Properties*

Some surfactant molecules are valued for their antimicrobial effects.<sup>155</sup> Cationic surfactants in particular are the prime example of antimicrobial surfactants, most notably alkyldimethylbenzylammonium chloride (ADBAC). When applied to a surface at an alkaline or neutral pH, these kinds of surfactants absorb and penetrate a microbial cell wall, react with the cytoplasmic membrane, leak low molecular weight material, degrade proteins and nucleic acids, and cause eventual cell lysis and death.<sup>156</sup>

### 4.3 Krafft Temperature of Surfactants

The Krafft temperature describes the temperature at which the surfactant solubility increases dramatically and allows for the formation of micelles in solution.<sup>157</sup> Described another way, it describes the minimal temperature required to achieve micellization. Measuring this temperature or the complementary indicator known as the critical micelle concentration can be done with isothermal titration calorimetry,<sup>158,159</sup> surface tensiometry,<sup>160</sup> nuclear magnetic resonance spectroscopy,<sup>161–163</sup> conductometry,<sup>164</sup> or dynamic light scattering.<sup>162,165,166</sup> Defining the Krafft temperature of a surfactant is important for its eventual inclusion into topical creams, lotions, detergents, or other transdermal drug delivery system to ensure product stability and effectiveness. Figure 4.1 demonstrates the relationship between the Krafft temperature and the critical micelle concentration.

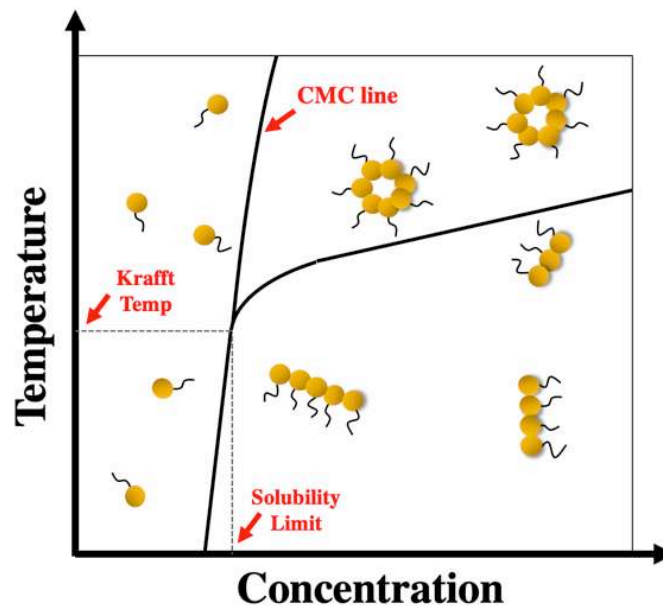


**Figure 4.1:** A schematic graph showing how temperature and concentration affects surfactant behavior. Below the Krafft temperature, no micelles will form; single molecules of surfactant will remain in disorder. Below the critical micelle concentration (CMC), only lamellar phase arrangements will form in solution.

#### 4.4 Characterization of Ceteth-10-Phosphate and Dicetylphosphate

Ceteth-10-phosphate and dicetylphosphate were received from Tolmar pharmaceuticals with instruction to identify the Krafft temperature using dynamic light scattering (DLS). Solutions of these surfactants were prepared in Millipore filtered water at concentrations of 0.01, 0.02, and 0.03% (v/v). Figure 4.2 provides the chemical structures of these two surfactants.

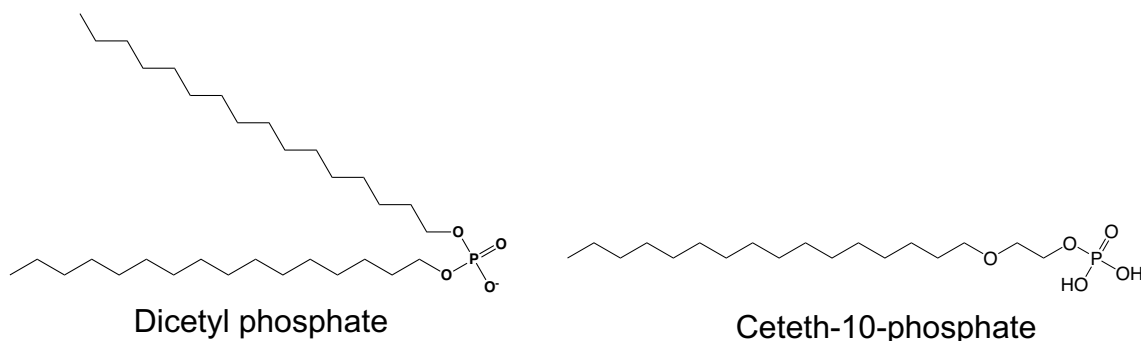


**Figure 4.2:** Chemical structures of the two surfactants of interest. Each demonstrates the typical hydrocarbon tail and hydrophilic head typical of a surfactant molecule

Size measurements were collected with dynamic light scattering (DLS, Malvern Zetasizer Nano). DLS measures a particle's hydrodynamic diameter by measuring light scattered by Brownian motion. Bombardment by solvent molecules within a cuvette results in the random, fluctuating motion of the solvated particle. The velocity of this motion is called the translational diffusion coefficient. This property is related to the size of the particle through the Stokes-Einstein equation<sup>167</sup> given in EQN 9:

$$d(H) = \frac{kT}{3\pi\eta D}$$

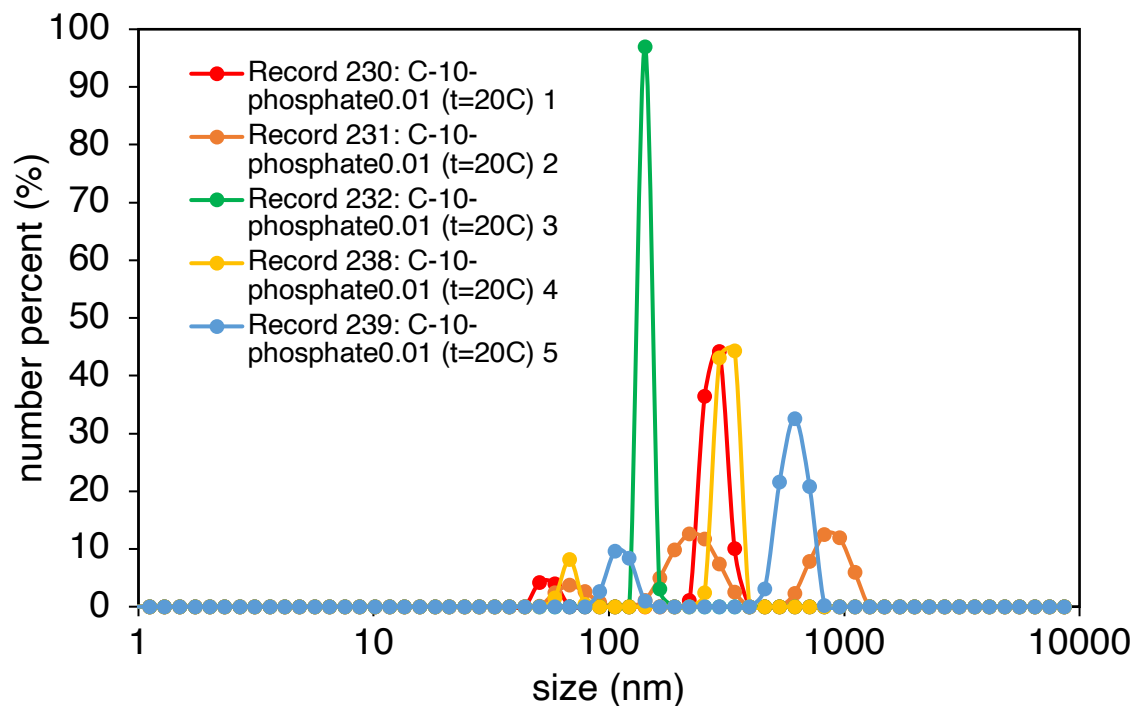
$d(H)$  = hydrodynamic diameter  
 $k$  = Boltzmann constant  
 $T$  = temperature  
 $\eta$  = viscosity  
 $D$  = translational diffusion coefficient

As the intensity of scattered light fluctuates in time, the instrument calculates a correlation function to determine if the incident signal is the result of scattering from the same particle. If the analyte particles are large, the signal in the correlogram will decay slowly because correlation is sustained for a longer period of time. The presence of comparatively small particles, which move more quickly, will cause a quick decay in signal on the correlogram. For this study, approximately 1.0 mL of the aqueous ceteth-10-phosphate or dicetyl phosphate was loaded into 1.0 cm glass cuvettes. Micelle formation and size were evaluated as a function of temperature in backscatter mode (173°). Measurements were repeated five times for ceteth-10-phosphate solutions; ten total scans comprised each individual trace. Measurements were repeated 3 times for the dicetylphosphate solutions. Dicetylphosphate measurements were conducted by Mia Halliday. Again, ten total scans comprised each individual trace. The reported error of the internal thermometer was  $\pm 0.2$  K. A 15 min equilibration time between measurements ensured homogenous temperatures throughout the aqueous sample.

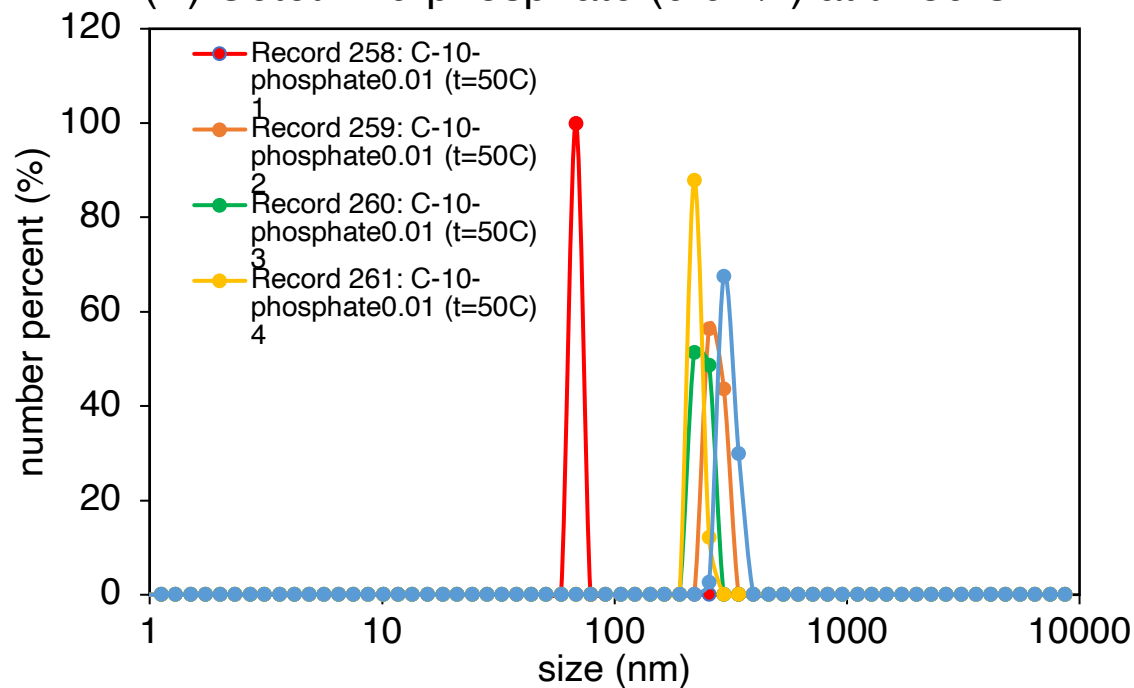
#### **4.5 Preliminary Ceteth-10-Phosphate Results**

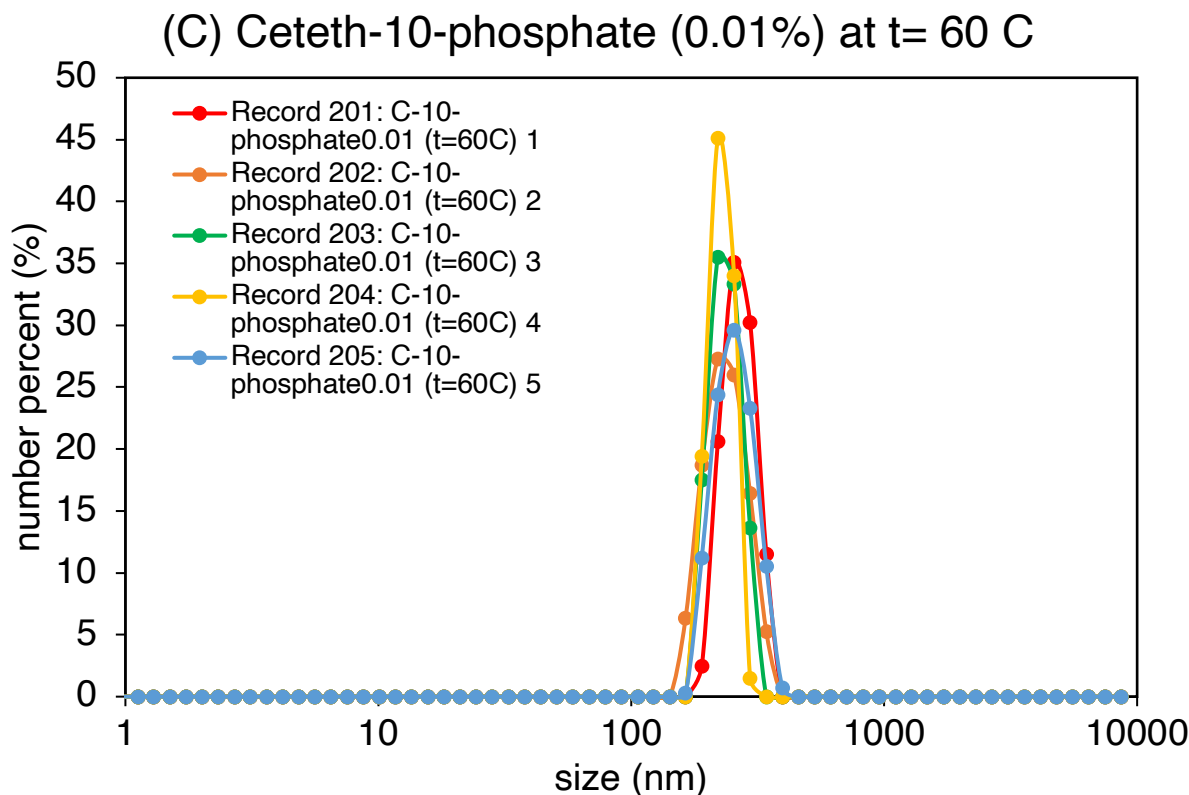
A preliminary temperature ramp from 20 °C to 60 °C was conducted to evaluate micelle formation below and above 50 °C. Figure 4.3a, 4.3b, and 4.3c show the DLS results of this set of scans across these three temperatures. At 20 °C, the solution of 0.01% ceteth-10-phosphate contains particles of disparate sizes across the set of five experimental traces. At 50 °C, this same solution contains a more uniform distribution of particle sizes (~420 nm). At 60 °C, all 5 experiments yielded size distributions whose average size was 420 nm. Experiments varied slightly in the size ranges, but overall, particle size uniformity was achieved by 60 °C.

(A) Ceteth-10-phosphate (0.01%) at t= 20 C



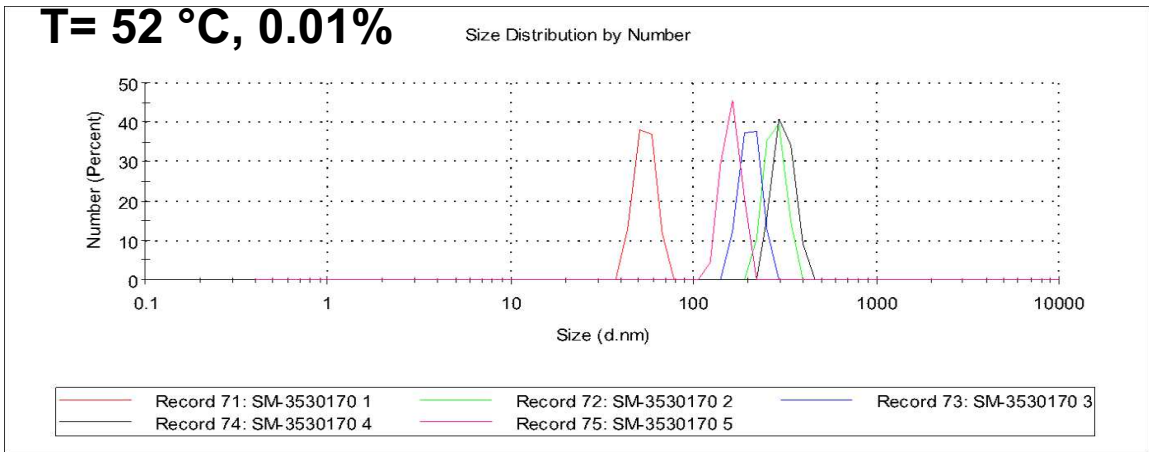
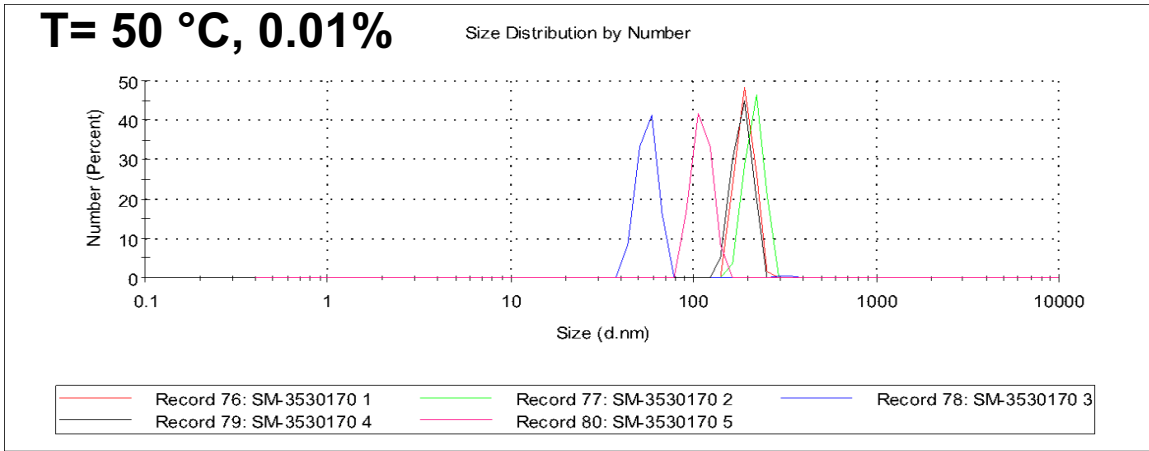
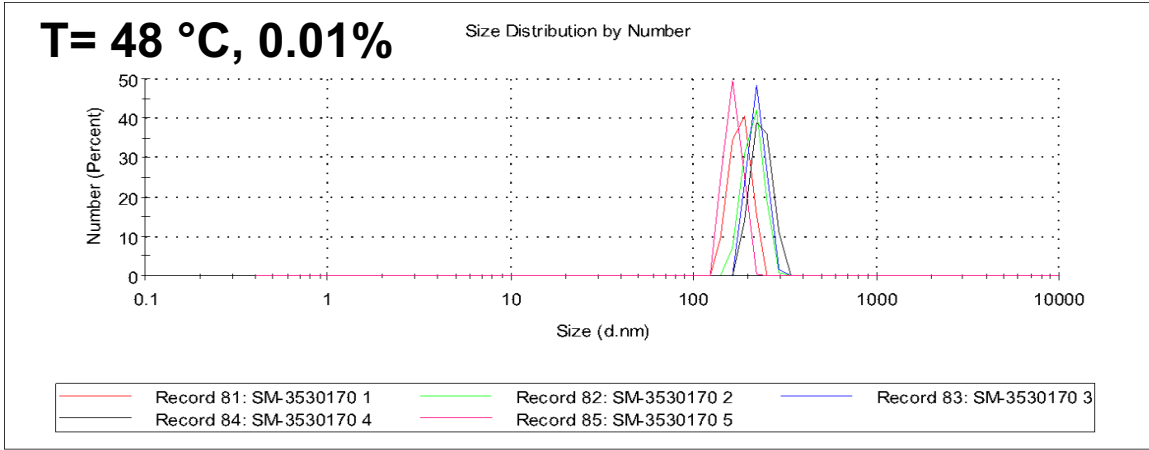
(B) Ceteth-10-phosphate (0.01%) at t= 50 C





**Figure 4.3:** Particle sizes in a solution of 0.01% ceteth-10-phosphate as indicated by dynamic light scattering results at (A) 20 °C (B) 50 °C and (C) 60 °C.

As a result of the preliminary scans, more granular temperature points (48, 50, 52, 54, 56, and 58 °C) were selected to measure the Krafft temperature more precisely. Additionally, two extra solutions of 0.02% and 0.03% ceteth-10-phosphate were prepared to evaluate the effect of concentration. Figure 4.4 contains a set of 6 raw spectra collected that reflects the size distributions across these six additional temperatures for 0.01% ceteth-10-phosphate. Figure 4.5 groups the raw data collected for the six additional temperatures for 0.02% ceteth-10-phosphate solutions and Figure 4.6 for the 0.03% ceteth-10-phosphate solutions. These spectra were collected during the pandemic, and the lack of access to the original experiments encumbers the ability to replot them.



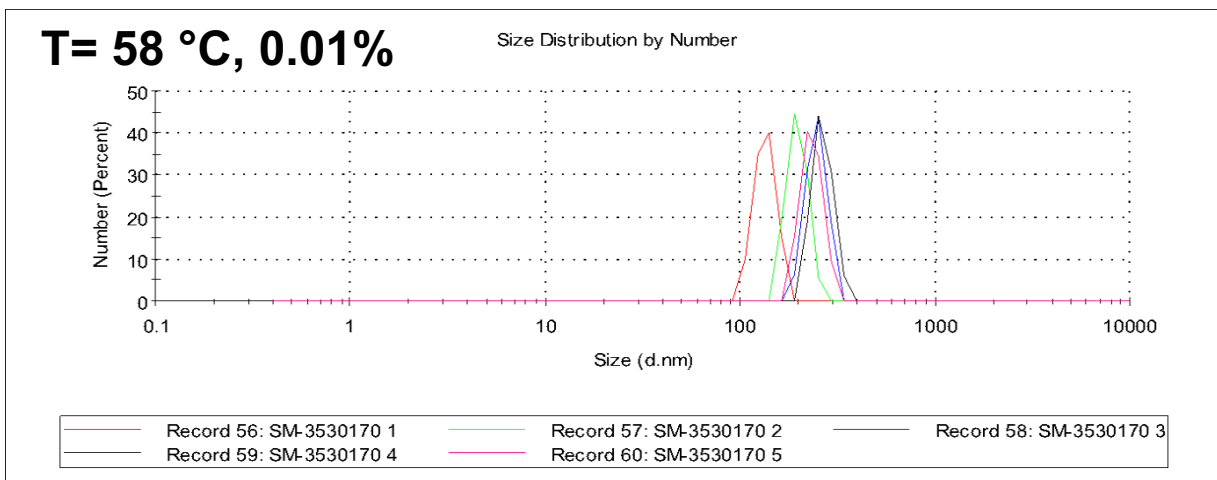
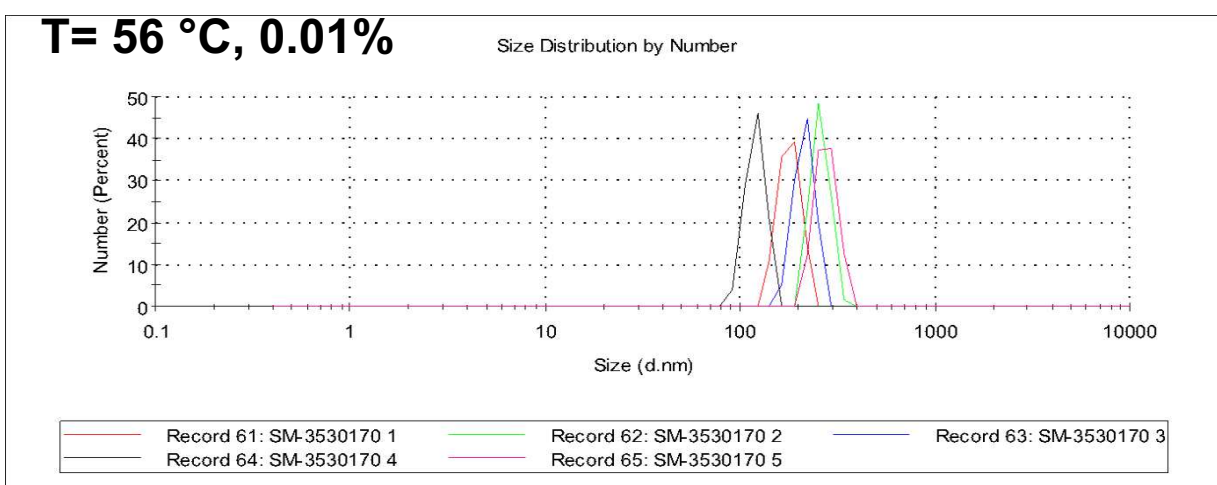
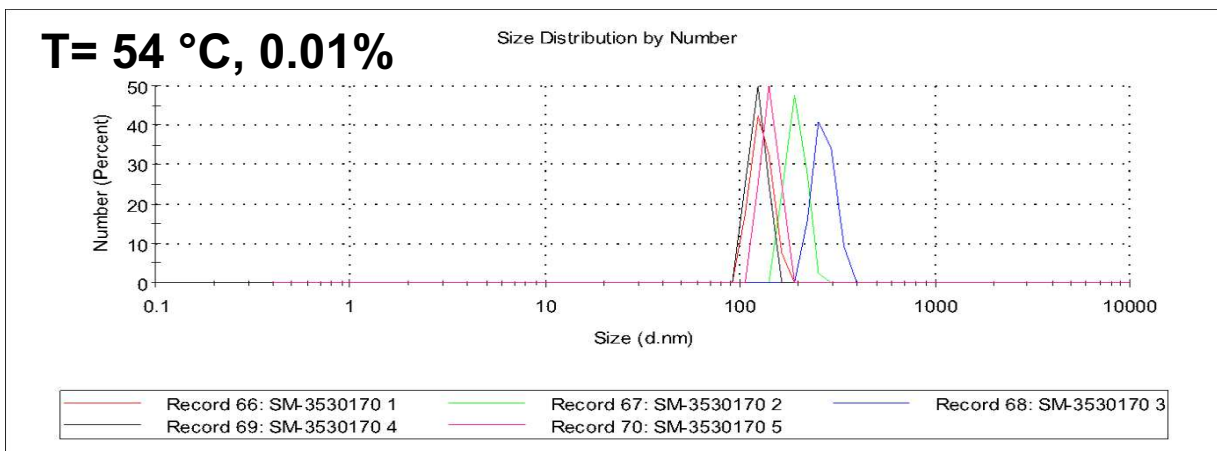
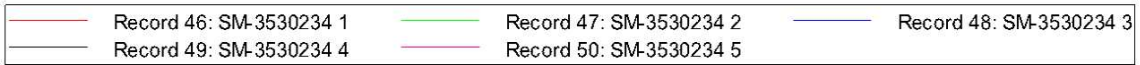
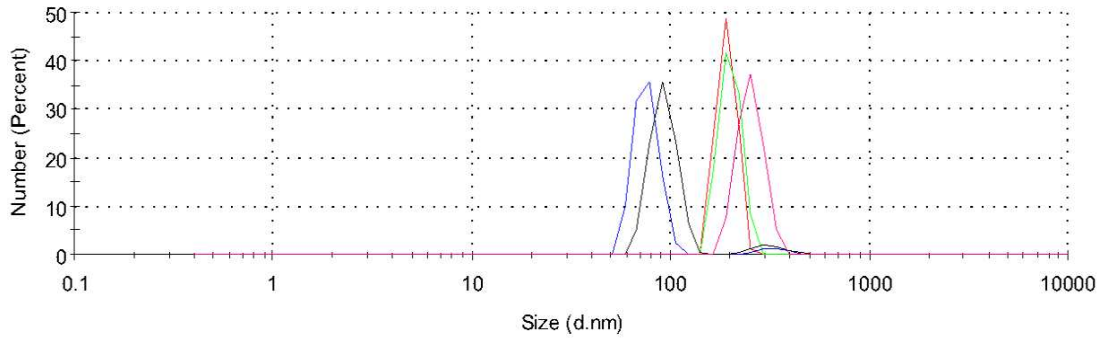


**Figure 4.4:** Dynamic light scattering results for a solution of 0.01% ceteth-10-phosphate solutions at 48, 50, 52, 54, 56, and 58 °C.

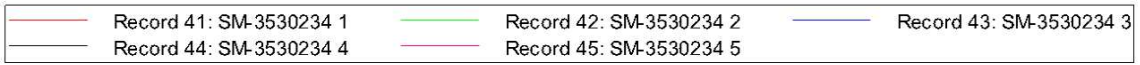
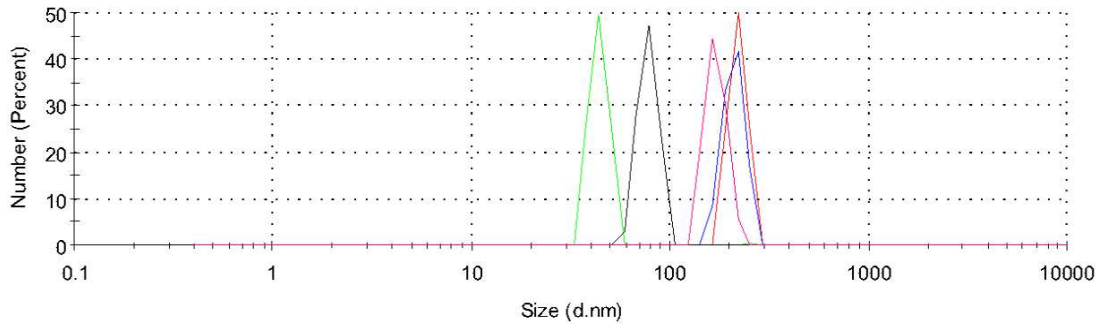
**T= 48 °C, 0.02%**

Size Distribution by Number



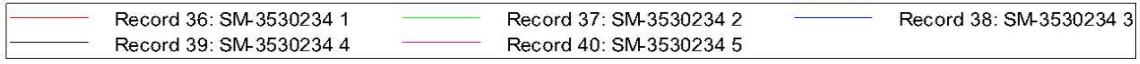
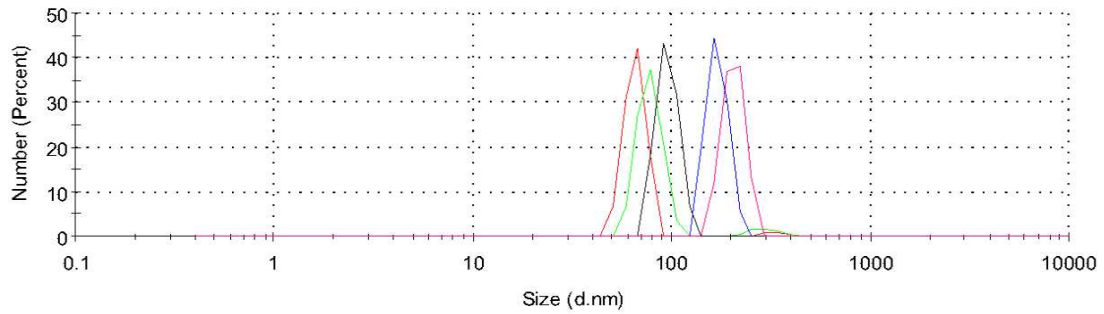
**T= 50 °C, 0.02%**

Size Distribution by Number



**T= 52 °C, 0.02%**

Size Distribution by Number



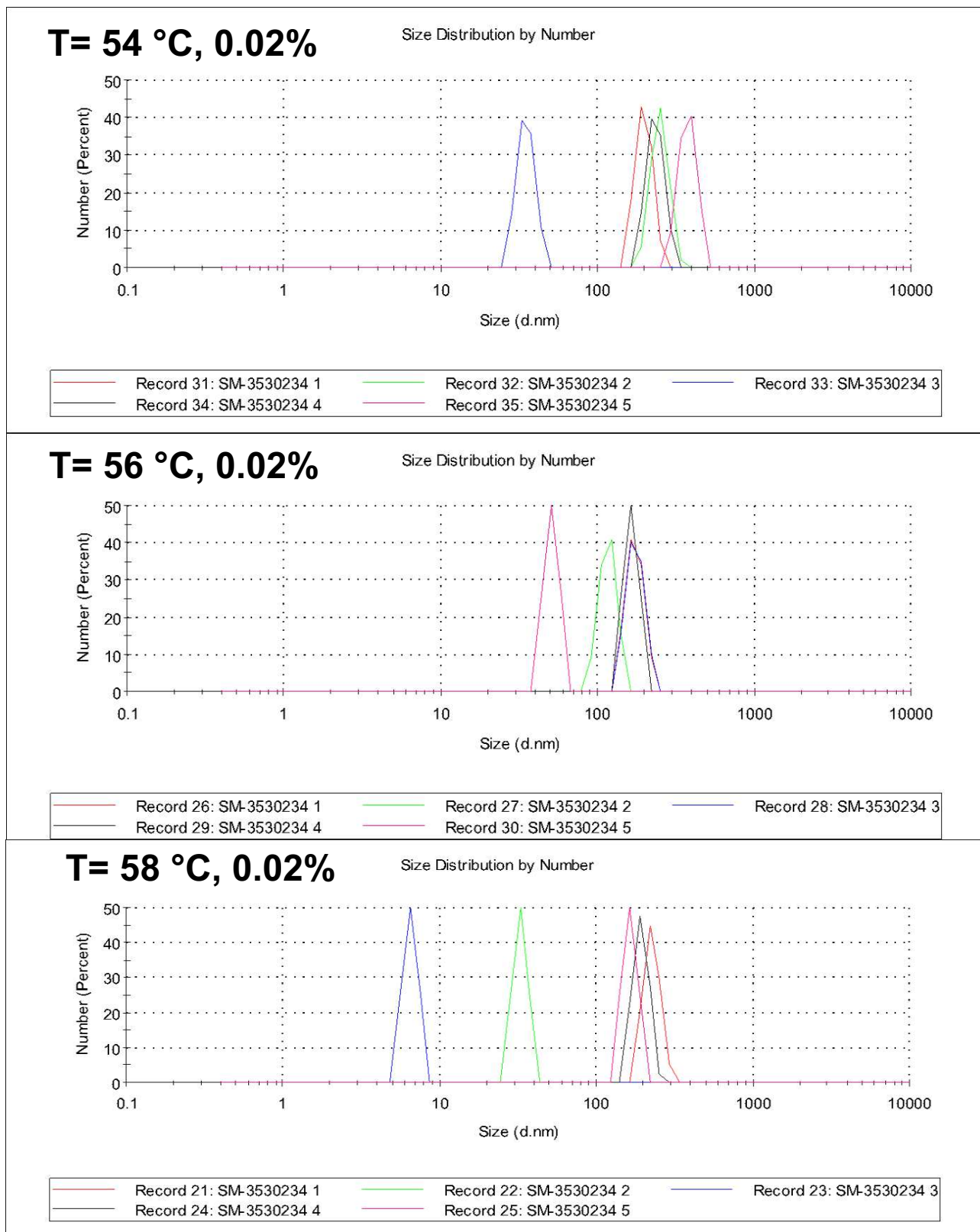
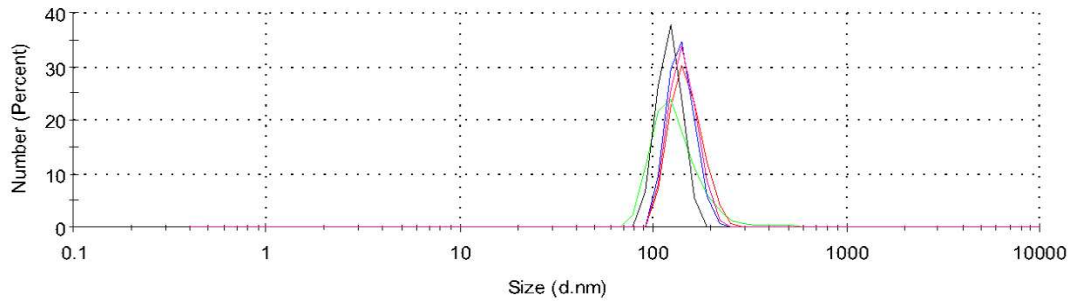


**Figure 4.5:** Dynamic light scattering results for a solution of 0.02% ceteth-10-phosphate solutions at 48, 50, 52, 54, 56, and 58 °C.

**T= 48 °C, 0.03%**

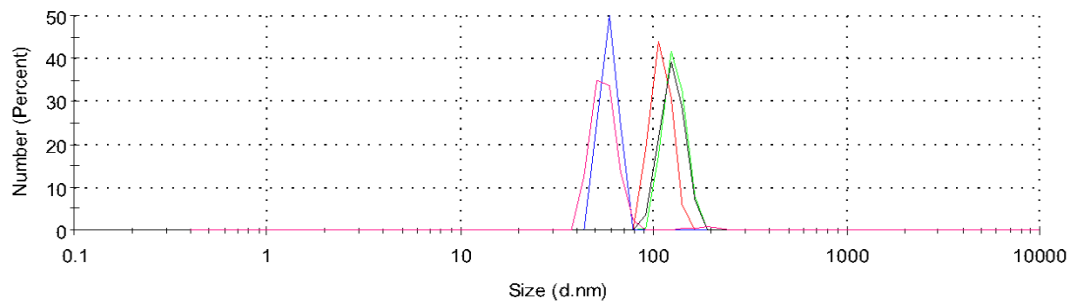
Size Distribution by Number



Record 116: SM-3530245 1	Record 117: SM-3530245 2	Record 118: SM-3530245 3
Record 119: SM-3530245 4	Record 120: SM-3530245 5	

**T= 50 °C, 0.03%**

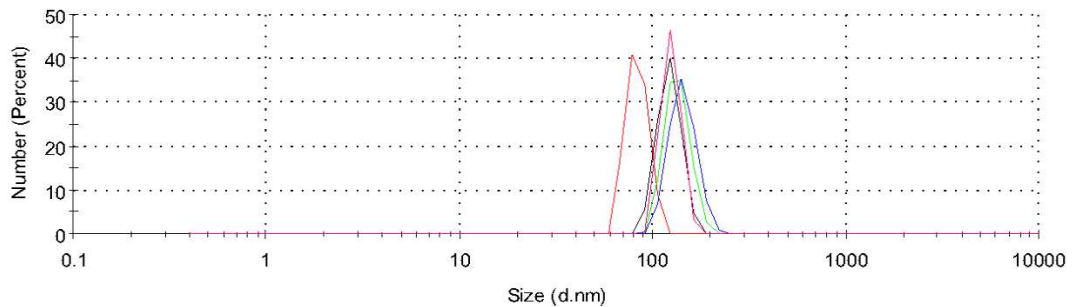
Size Distribution by Number



Record 111: SM-3530245 1	Record 112: SM-3530245 2	Record 113: SM-3530245 3
Record 114: SM-3530245 4	Record 115: SM-3530245 5	

**T= 52 °C, 0.03%**

Size Distribution by Number



Record 106: SM-3530245 1	Record 107: SM-3530245 2	Record 108: SM-3530245 3
Record 109: SM-3530245 4	Record 110: SM-3530245 5	

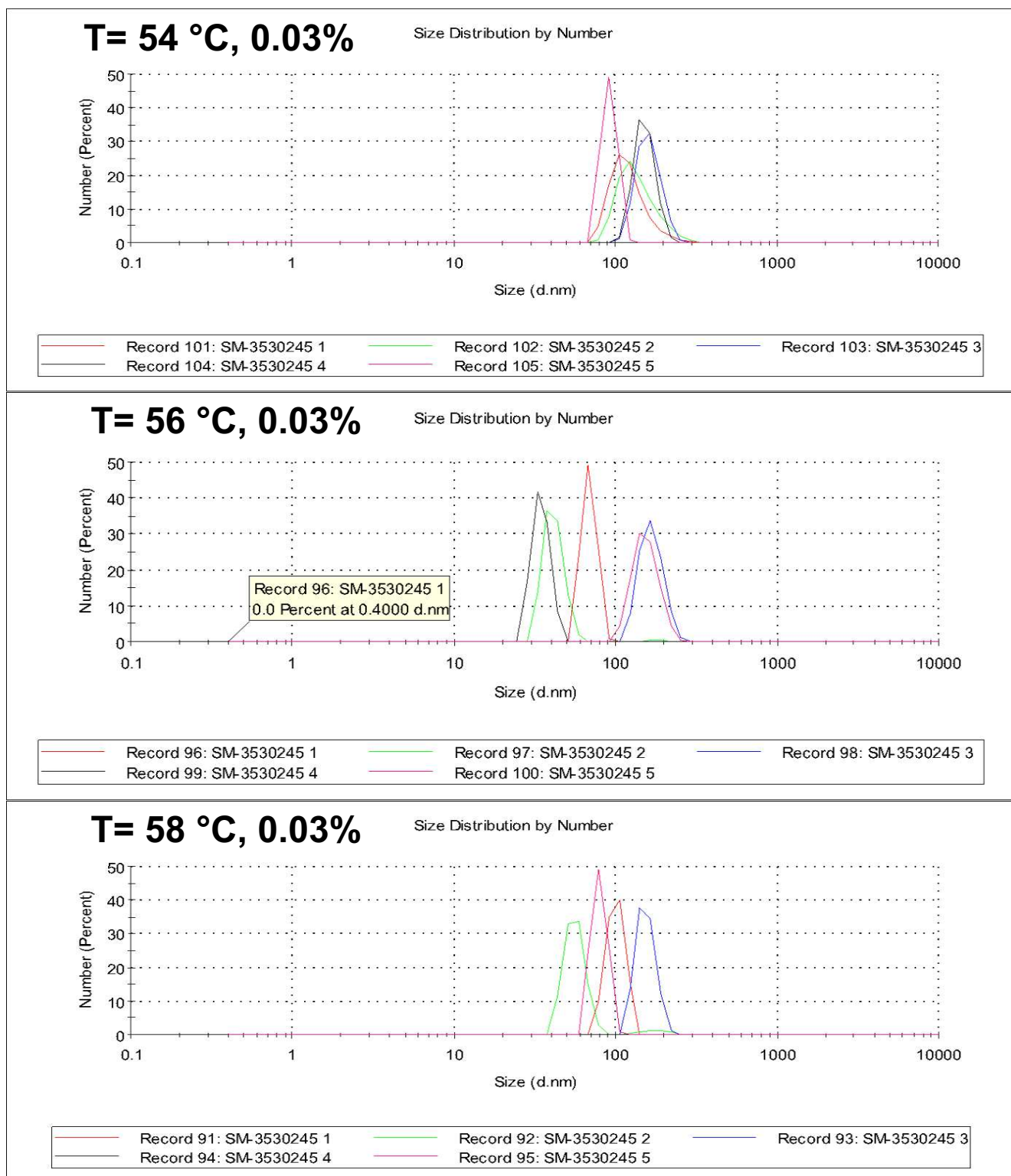


**Figure 4.6:** Dynamic light scattering results for a solution of 0.03% ceteth-10-phosphate solutions at 48, 50, 52, 54, 56, and 58 °C.

## 4.6 Discussion of Ceteth-10-Phosphate Results

The DLS results measuring the average size of reverse micelles in solution are discussed based on the concentration of solution. Given the lack of clear narrative that would point to a definitive Krafft temp determination, the results are discussed in tandem at the end of this section.

### *4.6.1 Solution of 0.01% Ceteth-10-Phosphate*

The DLS results of the various solutions of ceteth-10-phosphate are discussed by their respective concentrations. For the 0.01% ceteth-10-phosphate solution, micelle formation was evident at temperatures as low as 48 °C. The five scans collected at this temperature show reproducible size dispersity. The average hydrodynamic diameter at 48 °C is about 250 nm. However, as the experimental temperature was ramped up in 2 C increments, the size dispersity across the five experiments becomes less consistent. At 50 °C, the solution of 0.01% ceteth-10-phosphate appears to contain micelles that do not reflect the same size uniformity across the five experiments. Only three of the five experiments show size dispersities that mimic what was observed at 48 °C. The other experiments yielded average hydrodynamic diameters that were smaller (approximately 100nm and 60 nm, respectively). As temperatures was raised to 52 °C, the experiments yield even less consistent size results. At 54 -60 °C, the five experiments fail to show the consistency of size results first seen at 48 °C, though the average hydrodynamic diameter of any one experiment does not drop below 100 nm.

A closer look at the data does not reveal any evidence of hysteresis, as the replicate experiments that deviated from the median hydrodynamic diameter were neither the first replicates after changing temperature nor the last. This suggests that sample equilibration at the

new temperatures is not an immediate cause for explaining the reason some experiments show different sized micelles in solution.

#### *4.6.2 Solution of 0.02% ceteth-10-phosphate*

For the 0.02% ceteth-10-phosphate solution, micelle formation was evident at temperatures as low as 48 °C, but the five experiments again did not yield consistent sizes. At 48 °C, two of the experiments showed that the size distribution averaged less than 100 nm, but that some micelles of dramatically larger size (250 nm) were also present in solution as indicated by a tail in the peak. Other experiments at 50 and 52 °C also resulted in replicates whose size distributions displayed tailing behavior that revealed a minority population of much larger reverse micelles. At no temperature between 48 and 60 °C did the DLS experiments result in an experiment that yielded an average hydrodynamic diameter similar to more than one other experiment throughout the five replicates. In fact, at 54, 56, and 58 °C, some experiments resulted in experiments whose average hydrodynamic diameter result was between 30 and 50 nm.

#### *4.6.3 Solution of 0.03% ceteth-10-phosphate*

As with the other solutions of the 0.01% and 0.02% ceteth-10-phosphate, the 0.03% ceteth-10-phosphate was investigated at more granular temperatures to determine if a certain temperature induced a uniformly and predictably sized population of micelles. The results of the 0.03% ceteth-10-phosphate solution at 48 °C were similar to the results of the 0.03% ceteth-10-phosphate solution at 48 °C; all five replicate experiments yielded size distributions that reproduced the data of the previous scans. These five experiments all showed that the micelles

were about 150 nm in diameter. Unfortunately, moving to higher temperatures and collecting size data did not result in the same uniformity amongst replicate experiments. None of the other temperatures probed (50, 52, 54, 56, or 58 °C) resulted in scans that were similarly consistent in size results. At 54 °C, a few peaks centered about 100 nm begin to display tailing behavior suggesting a small population of micelles are much larger in size. At 58 °C, one experiment out of the five experiments also yielded this tailing behavior.

#### *4.6.4 Summary of Disparate Results*

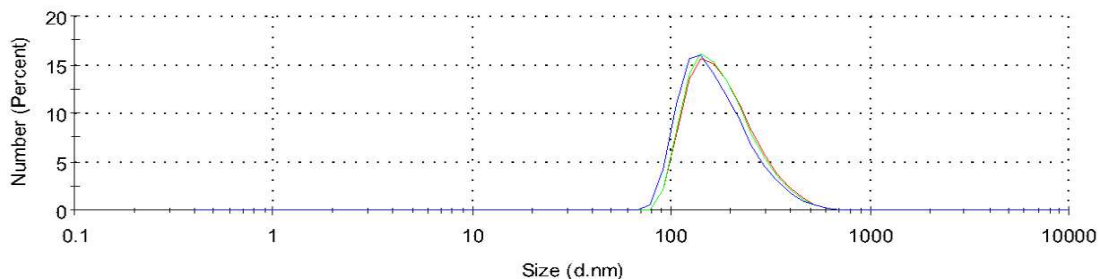
No definitive Krafft temperature determination of ceteth-10-phosphate could be made after considering all the experiments in tandem. As mentioned in the individual sections, a consistent set of DLS data suggesting a consistent hydrodynamic size was not achieved. Solution concentration did not significantly enhance the reproducibility of replicates either. However, we can still extract information from the disparate results collected at each temperature; namely, that if micelles of ceteth-10-phosphate are indeed forming spontaneously but at various sizes, that suggest some micelle stability is lost above 48 °C. Solutions were monitored visually between scans. No evidence such as a white opaque appearance was noted. Early studies at 20, 30 and 40 °C of 0.01% ceteth-10-phosphate showed that no micelle formation would result in multiple peaks centered about numerous values. Chaotic and unpredictable peak patterns at these low temperatures were not what was observed when scanning between 48 °C and 60 °C. Therefore, stable micelle formation can still be reasonably suggested, but predicting the size of the resultant micelle remains difficult beyond a rough range of 100-200 nm.

#### **4.7 Preliminary Dicetylphosphate Results**

A preliminary temperature ramp from 50 °C to 64 °C was conducted to evaluate micelle formation using the dicetylphosphate prepared to 0.01%. Figure 4.7 shows the grouped DLS results of this set of scans across these six temperatures. Scans were collected in both directions (low temp to high temp and vice versa) to investigate hysteresis effects.

**T= 50 °C, 0.01%**

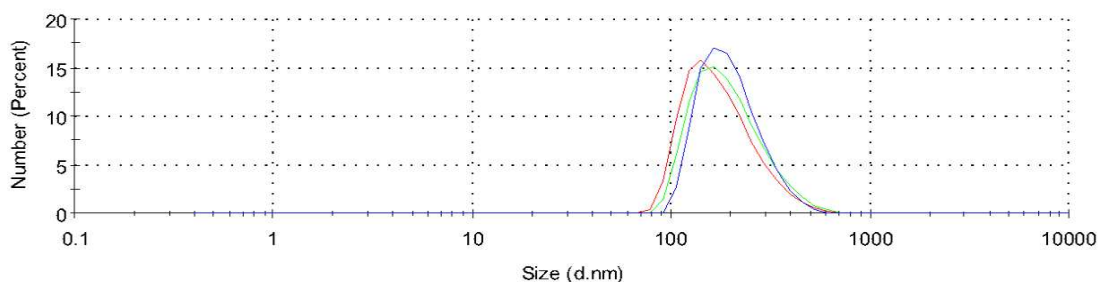
Size Distribution by Number



- Record 1: Dicetyl\_Phosphate\_temp50\_Mia\_17Feb2021 1
- Record 2: Dicetyl\_Phosphate\_temp50\_Mia\_17Feb2021 2
- Record 3: Dicetyl\_Phosphate\_temp50\_Mia\_17Feb2021 3

**T= 55 °C, 0.01%**

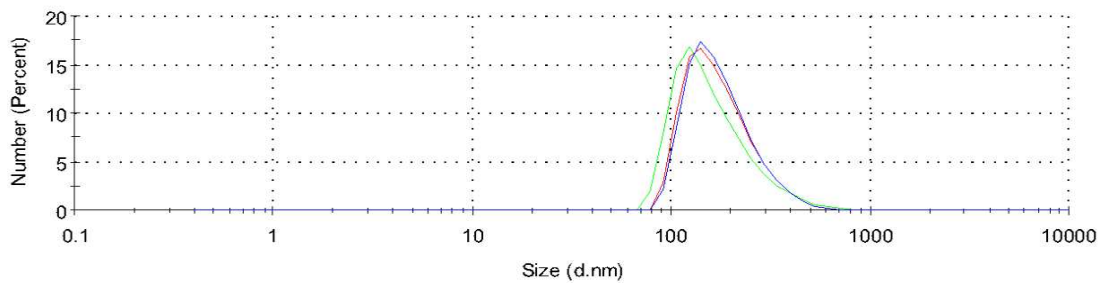
Size Distribution by Number



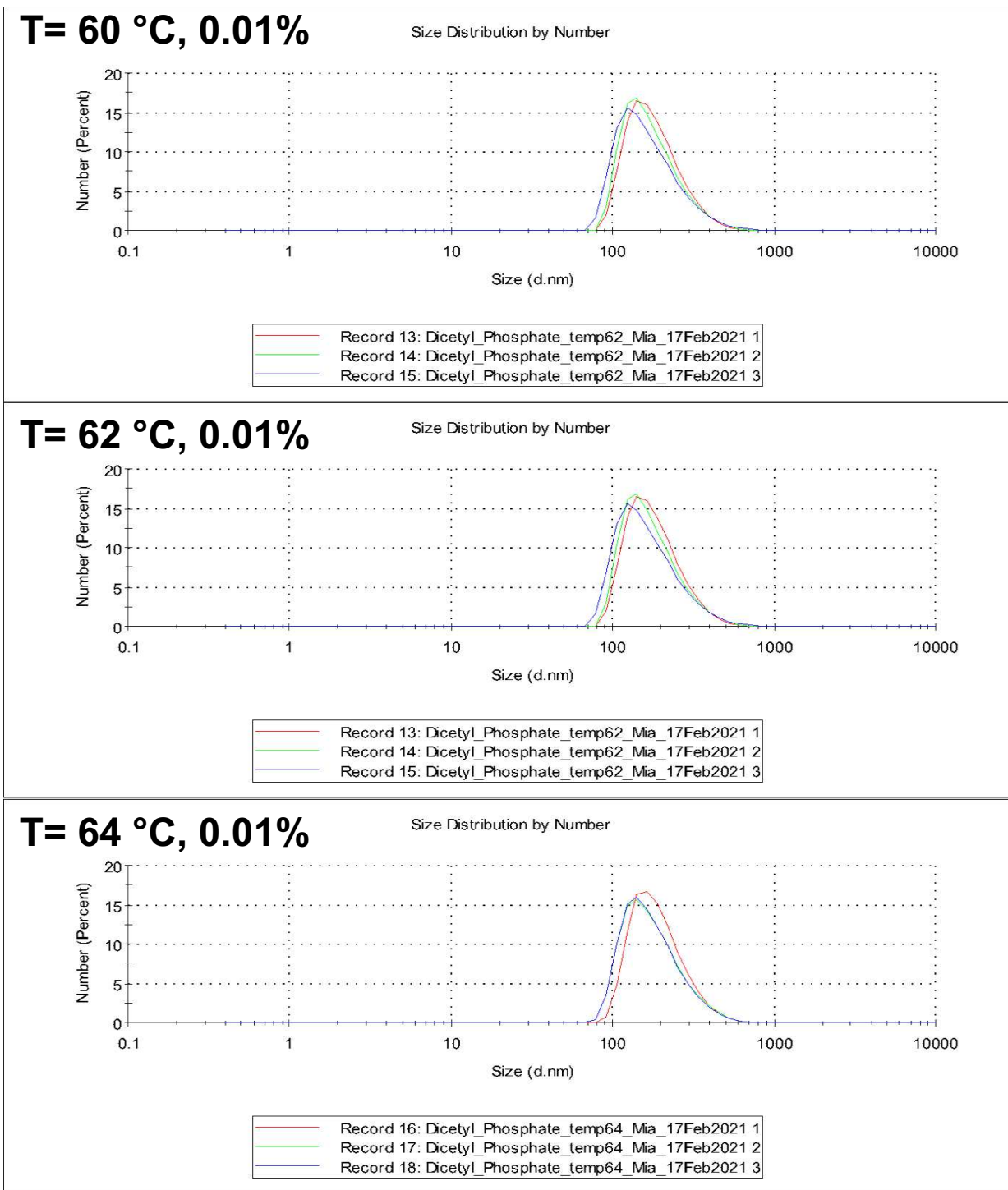
- Record 4: Dicetyl\_Phosphate\_temp55\_Mia\_17Feb2021 1
- Record 5: Dicetyl\_Phosphate\_temp55\_Mia\_17Feb2021 2
- Record 6: Dicetyl\_Phosphate\_temp55\_Mia\_17Feb2021 3

**T= 58 °C, 0.01%**

Size Distribution by Number

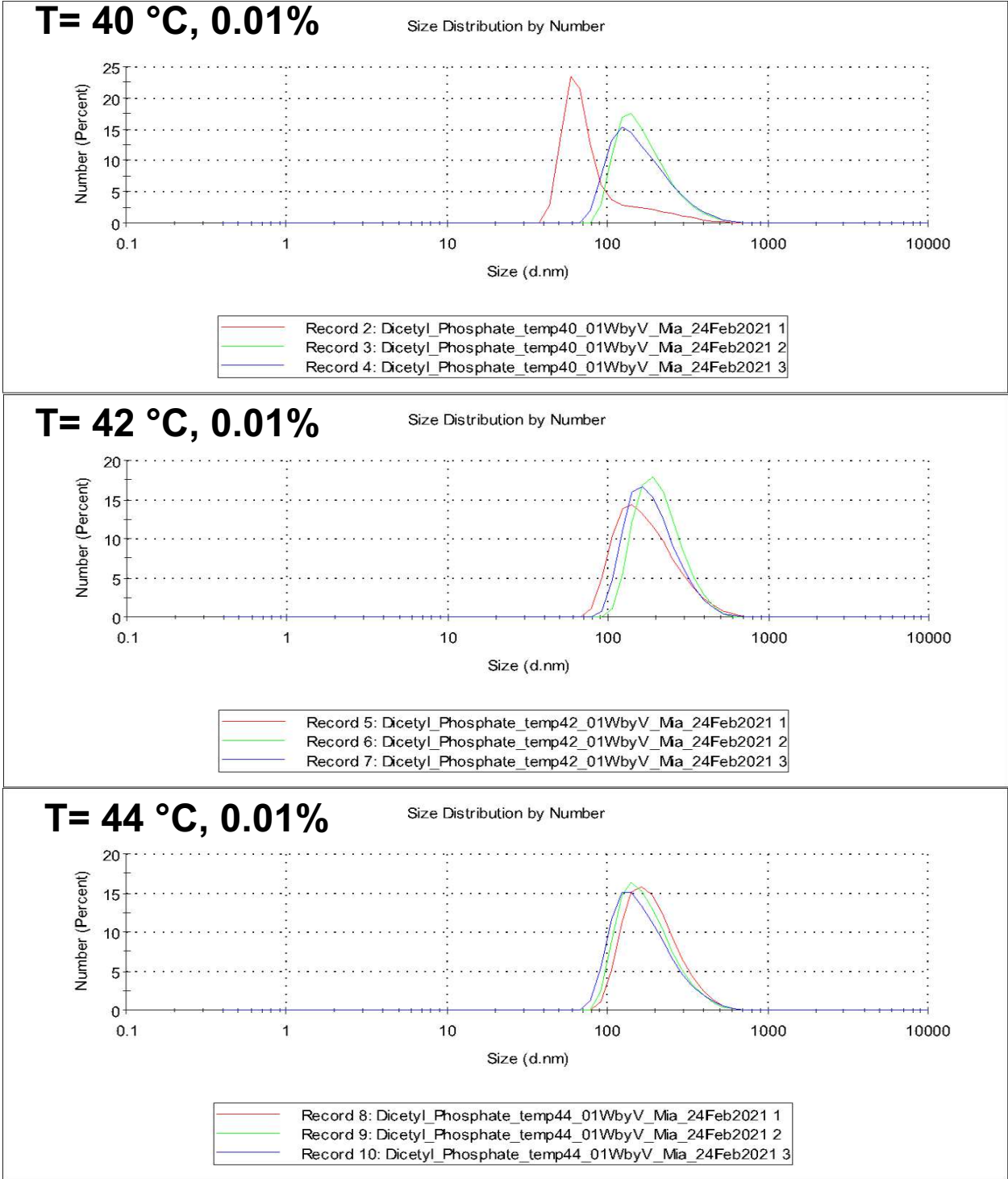


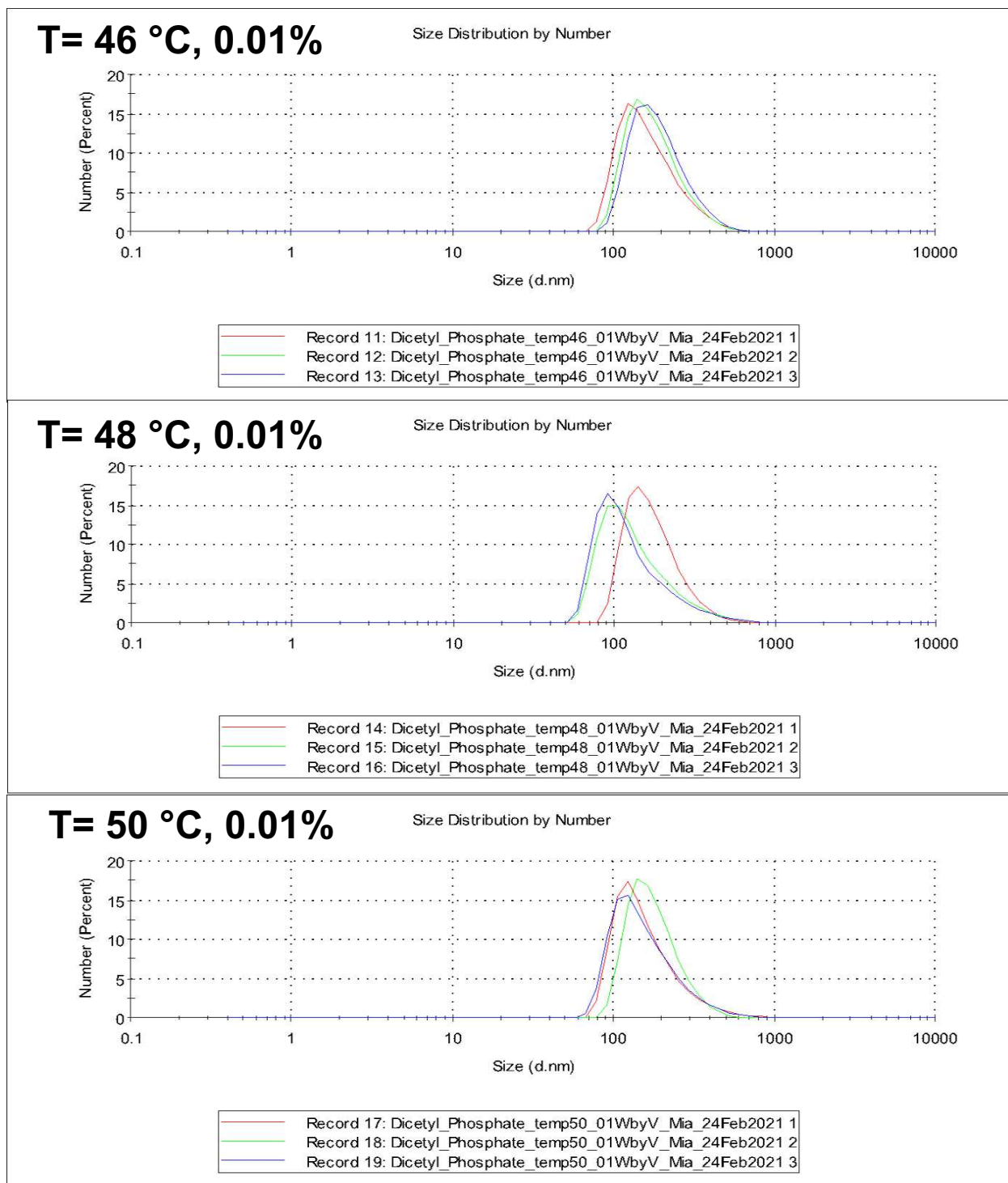
- Record 7: Dicetyl\_Phosphate\_temp58\_Mia\_17Feb2021 1
- Record 8: Dicetyl\_Phosphate\_temp58\_Mia\_17Feb2021 2
- Record 9: Dicetyl\_Phosphate\_temp58\_Mia\_17Feb2021 3



**Figure 4.7:** Dynamic light scattering results for a solution of 0.01% dicetyl phosphate solutions at 50, 55, 58, 60, 62, and 64 °C.

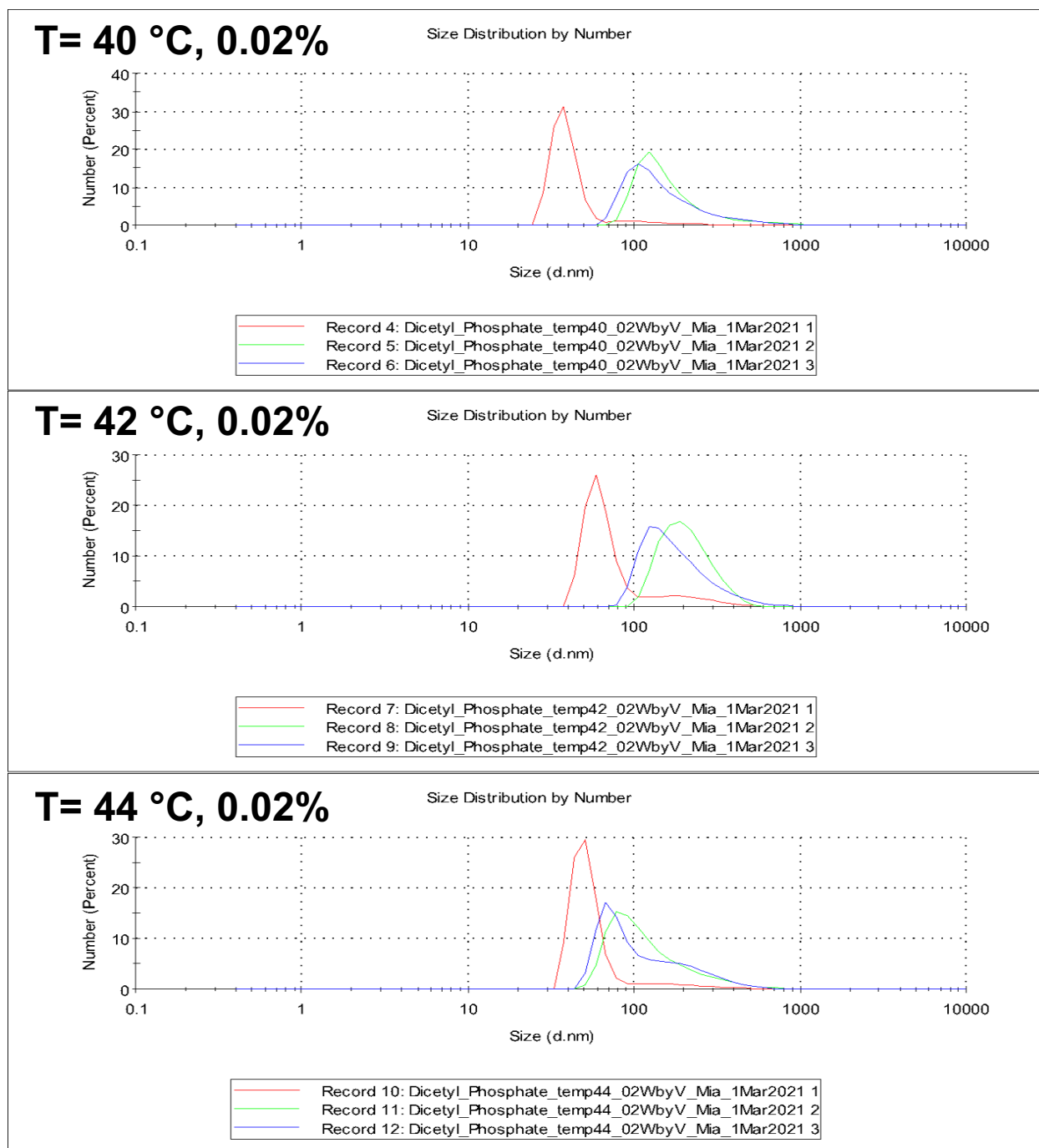
After collecting micellization data between 50 °C and 64 °C, a slightly lower temperature range was chosen to determine the Krafft Temperature. Figure 4.8 shows the grouped DLS results of this set of scans across a lower temperatures range between 40 °C and 50 °C.





**Figure 4.8:** Dynamic light scattering results for a solution of 0.01% dicetylphosphate at a lower range of temperatures: 40, 42, 44, 46, 48, and 50 °C.

Finally, a solution of 0.02% dicetylphosphate was prepared for DLS analysis. Figure 4.9 shows the grouped DLS results for scans collected between 40 °C and 50 °C.



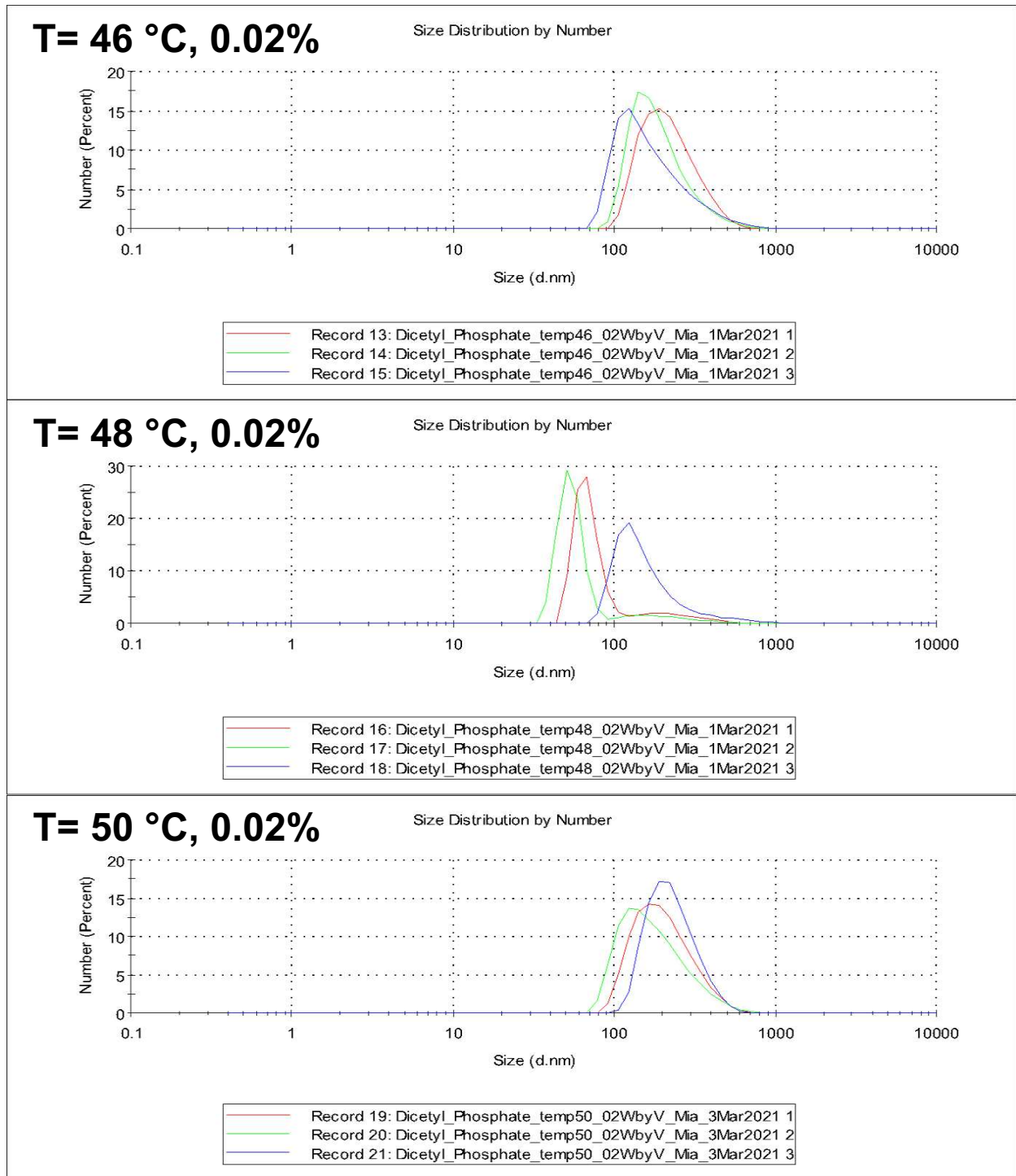


**Figure 4.9:** Dynamic light scattering results for a solution of 0.02% dicetylphosphate at 40, 42, 44, 46, 48, and 50 °C.

## 4.8 Discussion of Dicetylphosphate Results

The DLS measurements on solutions of dicetylphosphate were conducted by Mia Halliday. The results are discussed based on the concentration of the prepared dicetylphosphate solution.

### *4.8.1 Solution of 0.01% Dicetylphosphate Results*

The grouped spectra presented in Figure 4.7 suggest that the solution of 0.01% dicetylphosphate forms micelles between temperatures between 50 °C and 60 °C. The size distribution by number covers a larger range than the micelles formed from ceteth-10-phosphate. The average hydrodynamic diameter of 100-200 nm, however, was still similar to the results shown in Figure 4.4. As temperature was ramped up from the initial 50 °C, the size distribution remained consistent across all three scans. The expanded range of sizes was also consistent between 50 °C and 60 °C. Going up in temperature did not narrow the range of sizes or lead to a more gaussian distribution. Considering this stability, it is possible that the Krafft temperature of the 0.01% dicetylphosphate solution is lower than 50 °C.

The raw data presented in Figure 4.8 suggest that the Krafft temperature may lie in the temperature range between 40 °C and 50 °C. At 40 °C, the size distribution of the dicetylphosphate micelles is inconsistent between the three experiments. This is indicated by the experiment that resulted in micelles whose size distribution was well below 100 nm but still contained a minority population of larger micelles as indicated by the distribution's tails. However, raising the temperature to 42 °C resulted in data that showed a consistent average hydrodynamic diameter over three replicate experiments.

The rest of the experiments conducted at 44, 46, 48, and 50 °C resulted in size distributions that remained consistent between all experiments. At 48 °C, some size data suggests

that micelle formation trends towards smaller sizes, but the results still suggest that the Krafft temperature may reside between 40 °C and 42 °C.

#### *4.8.2 Solution of 0.02% Dicetylphosphate Results*

Scans of 0.02% dicetylphosphate between 40 °C and 50 °C suggested micelle formation resulted in inconsistent size distributions across the three replicates. Notably, the size distributions often showed tailing behavior that indicated small numbers of much larger micelles within solution. At 50 °C, the three replicate experiments began to reflect size distributions whose average hydrodynamic diameter was about 100-200 nm. Furthermore, good reproducibility between replicates suggested more stable and predictable micelle formation.

### **4.9 Conclusions**

The results and subsequent discussion presented here demonstrate a further need to continue the study of solutions of both surfactants to determine the Krafft temperature. A complementary technique, isothermal titration calorimetry (ITC) constitutes an ideal analytical technique to further this study. This is typically used to analyze intermolecular interactions such as binding events like enzyme kinetics. By measuring the heat of interaction between molecules, it also affords the researcher the ability to determine other thermodynamic parameters such as Gibbs energy, enthalpy, and entropy. This technique offers the most feasible path forward, though other techniques for determining Krafft temperature (or the complementary measurement of critical micelle concentration) such as Rayleigh interferometry,<sup>169</sup> conductivity,<sup>170</sup> or time resolved fluorescence quenching.<sup>170</sup>

## CHAPTER 5: CONCLUSIONS

The work presented here describes a breadth of impacts imparted by the nanoconfined reverse micelle system prepared with AOT and igeal CO-532 surfactants. The initial investigation of the glucose in reverse micelles demonstrated the possibility of hydrogen tunneling at temperatures above freezing. The departure from classical exchange in nanoconfined spaces is a testament to the unique environment that may also exist in the pocket of proteins or enzymes, ion channels, or even aquaporins in biology.<sup>171,172</sup> This has particularly specific implications in organisms that live and flourish in arctic biomes. In addition to their other well defined survival mechanisms, it is possible their survival in such extreme conditions is possible because of unseen adaptations occurring on the nanoscale within their cells or cell organelles.<sup>173</sup>

In the urea loaded reverse micelle systems, the research showed that a combination of low temperatures ( $\sim 275$  K) and nanoconfinement exacerbated the disrupting effect of urea as demonstrated by the huge increase in reverse micelles for the smallest  $w_0$  values of reverse micelles prepared. Because this effect was shown for a process as simple as the spontaneous formation of a reverse micelle interface of AOT,<sup>174</sup> it is likely the disruption effect extends to other interfaces as well. Even a common eukaryotic cell membrane involves a complex mosaic of different macromolecules to assemble and function properly, and our findings suggest that urea may be particularly disruptive to the organization of the cell membrane matrix on the nanoscale.<sup>175</sup>

Finally, observing that nanoconfinement of sodium fluoride in nanosized reverse micelles prepared with ionic and non-ionic surfactants may have far reaching implications regarding the study of ion gradients in human biology and physiology. Ion gradients are already a well known

part of important processes like the electron transport chain, which drives ATP synthase or ion pumps like the sodium/potassium pump. However, less well known are the ion gradients that form at the surface of entities like red blood cells.<sup>176</sup> Our work shows that an electrochemical potential could be created in nanosized spaces where there is aggregation of ions near an interface. In concert, the results of chapters one through three continue to demonstrate we cannot underestimate how size restriction affects basic chemical properties and kinetic behavior.

## REFERENCES

1. Crans, D. C. & Levinger, N. E. The Conundrum of pH in Water Nanodroplets: Sensing pH in Reverse Micelle Water Pools. *Acc. Chem. Res.* **45**, 1637–1645 (2012).
2. Baruah, B. *et al.* When Is Water Not Water? Exploring Water Confined in Large Reverse Micelles Using a Highly Charged Inorganic Molecular Probe. *J. Am. Chem. Soc.* **128**, 12758–12765 (2006).
3. Lee, J. K., Banerjee, S., Nam, H. G. & Zare, R. N. Acceleration of reaction in charged microdroplets. *Q. Rev. Biophys.* **48**, 437–44 (2015).
4. Street, T. O., Bolen, D. W. & Rose, G. D. A molecular mechanism for osmolyte-induced protein stability. *Proc. Natl. Acad. Sci.* **103**, 13997–14002 (2006).
5. Correa, N. M., Silber, J. J., Riter, R. E. & Levinger, N. E. Nonaqueous Polar Solvents in Reverse Micelle Systems. *Chem. Rev.* **112**, 4569–4602 (2012).
6. Piletic, I. R., Moilanen, D. E., Spry, D. B., Levinger, N. E. & Payer, M. D. Testing the core/shell model of nanoconfined water in reverse micelles using linear and nonlinear IR spectroscopy. *J. Phys. Chem. A* **110**, 4985–4999 (2006).
7. Moilanen, D. E., Fenn, E. E., Wong, D. & Fayer, M. D. Water dynamics in large and small reverse micelles: From two ensembles to collective behavior. *J. Chem. Phys.* (2009) doi:10.1063/1.3159779.
8. Riter, R. E., Willard, D. M. & Levinger, N. E. Water Immobilization at Surfactant Interfaces in Reverse Micelles. *J. Phys. Chem. B* (2002) doi:10.1021/jp973330n.
9. Lee, A. S. The glucose-regulated proteins: Stress induction and clinical applications. *Trends in Biochemical Sciences* (2001) doi:10.1016/S0968-0004(01)01908-9.

10. Miyawaki, O., Dozen, M. & Hirota, K. Cooperative hydration effect causes thermal unfolding of proteins and water activity plays a key role in protein stability in solutions. *J. Biosci. Bioeng.* (2016) doi:10.1016/j.jbiosc.2016.01.005.
11. Tannous, A., Pisoni, G. B., Hebert, D. N. & Molinari, M. N-linked sugar-regulated protein folding and quality control in the ER. *Seminars in Cell and Developmental Biology* (2015) doi:10.1016/j.semcdb.2014.12.001.
12. Ajit Varki, Richard D Cummings, Jeffrey D Esko, Hudson H Freeze, Pamela Stanley, Carolyn R Bertozzi, Gerald W Hart, and M. E. E. *et al. Essentials of Glycobiology, 2nd edition. Essentials of Glycobiology. Cold Spring Harbor (NY): Cold Spring Harbor Laboratory Print* (2009). doi:10.1016/S0962-8924(00)01855-9.
13. Wiederschain, G. Ya. Essentials of glycobiology. *Biochem. Mosc.* (2009) doi:10.1134/s0006297909090156.
14. Wiebenga-Sanford, B. P., DiVerdi, J., Rithner, C. D. & Levinger, N. E. Nanoconfinement's Dramatic Impact on Proton Exchange between Glucose and Water. *J. Phys. Chem. Lett.* **7**, 4597–4601 (2016).
15. Mittermaier, A. ZZ-Exchange. in *Encyclopedia of Biophysics* (ed. Roberts, G. C. K.) 2796–2797 (European Biophysical Societies' Association, 2013). doi:10.1007/978-3-642-16712-6\_354.
16. Wiebenga-Sanford, B. P., Diverdi, J., Rithner, C. D. & Levinger, N. E. Nanoconfinement's Dramatic Impact on Proton Exchange between Glucose and Water. *J. Phys. Chem. Lett.* **7**, 4597–4601 (2016).

17. Bagno, A., Rastrelli, F. & Scorrano, G. Detecting intermolecular NOEs by means of a novel DPFGE pulse sequence. Application to the solvation of carbohydrates in binary mixtures. *J. Magn. Reson.* **167**, 31–35 (2004).
18. Krishnamurthy, K. Hadamard excitation sculpting. *J. Magn. Reson.* **153**, 144–150 (2001).
19. Stott, K., Keeler, J., Van, Q. N. & Shaka, A. J. One-Dimensional NOE Experiments Using Pulsed Field Gradients. *J. Magn. Reson.* **125**, 302–324 (1997).
20. Van Geet, A. L. Calibration of the Methanol and Glycol Nuclear Magnetic Resonance Thermometers with a Static Thermistor Probe. *Anal. Chem.* **40**, 2227–2229 (1968).
21. Webb, B. *et al.* Temperature dependence of viscosity, relaxation times (T<sub>1</sub>, T<sub>2</sub>) and simulated contrast for potential perfusates in post-mortem MR angiography (PMMRA). *Int. J. Legal Med.* **131**, 739–749 (2017).
22. Tsukiashi, A. *et al.* Application of spin-crossover water soluble nanoparticles for use as MRI contrast agents. *Sci. Rep.* **8**, 33362–33366 (2018).
23. Harvey, J. M., Symons, M. C. R. & Naftalin, R. J. Proton magnetic resonance study of the hydration of glucose. *Nature* **261**, 435–436 (1976).
24. Tait, M. J., Suggett, A., Franks, F., Ablett, S. & Quickenden, P. A. Hydration of monosaccharides: A study by dielectric and nuclear magnetic relaxation. *J. Solut. Chem.* **1**, 131–151 (1972).
25. Hills, B. P. Multinuclear NMR studies of water in solutions of simple carbohydrates. *Mol. Phys.* **72**, 1099–1121 (1991).
26. Laage, D. & Hynes, J. T. A molecular jump mechanism of water reorientation. *Science* **311**, 32–35 (2006).

27. Zhang, Q., Wu, T. M., Chen, C., Mukamel, S. & Zhuang, W. Molecular mechanism of water reorientational slowing down in concentrated ionic solutions. *Proc. Natl. Acad. Sci. U. S. A.* **114**, 10023–10028 (2017).
28. Wiebenga-Sanford, B. P. *et al.* Sweet Confinement: Glucose and Carbohydrate Osmolytes in Reverse Micelles. *J. Phys. Chem. B* **122**, 9555–9566 (2018).
29. Meng, X. *et al.* Direct visualization of concerted proton tunnelling in a water nanocluster. *Nat. Phys.* **113**, 235–239 (2015).
30. Li, X. Z., Probert, M. I. J., Alavi, A. & Michaelides, A. Quantum nature of the proton in water-hydroxyl overlayers on metal surfaces. *Phys. Rev. Lett.* **104**, (2010).
31. Laage, D., Stirnemann, G., Sterpone, F., Rey, R. & Hynes, J. T. Reorientation and Allied Dynamics in Water and Aqueous Solutions. *Annu. Rev. Phys. Chem.* (2011) doi:10.1146/annurev.physchem.012809.103503.
32. Ceriotti, M. *et al.* Nuclear Quantum Effects in Water and Aqueous Systems: Experiment, Theory, and Current Challenges. *Chem. Rev.* **116**, 7529–7550 (2016).
33. Drechsel-Grau, C. & Marx, D. Collective proton transfer in ordinary ice: Local environments, temperature dependence and deuteration effects. *Physical Chemistry Chemical Physics* (2017) doi:10.1039/c6cp05679b.
34. Sattler, M. & Fesik, S. W. Use of deuterium labeling in NMR: Overcoming a sizeable problem. *Structure* **4**, 1245–9 (1996).
35. Karunakaran, C. *Spin resonance spectroscopy: Principles and applications. Spin Resonance Spectroscopy: Principles and applications* (Elsevier, 2018). doi:10.1016/C2016-0-04240-7.
36. Marshall, A. G. Calculation of NMR relaxation times for quadrupolar nuclei in the presence of chemical exchange. *J. Chem. Phys.* **52**, 2527–2534 (1970).

37. Ludwig, R. NMR relaxation studies in water-alcohol mixtures: the water-rich region. *Chem. Phys.* **195**, 329–337 (1995).
38. Schönhoff, M. NMR Methods for studies of organic adsorption layers. in *Studies in Interface Science* (Max Planck Institute, 2001). doi:10.1016/S1383-7303(01)80031-4.
39. Drechsel-Grau, C. & Marx, D. Quantum simulation of collective proton tunneling in hexagonal ice crystals. *Phys. Rev. Lett.* **112**, 148300–148302 (2014).
40. Suzuki, A. & Yui, H. Crystallization of confined water pools with radii greater than 1 nm in aot reverse micelles. *Langmuir* **30**, 7274–7282 (2014).
41. Van Horn, W. D., Ogilvie, M. E. & Flynn, P. F. Reverse micelle encapsulation as a model for intracellular crowding. *J. Am. Chem. Soc.* **131**, 8030–8039 (2009).
42. Klíčová, L., Muchová, E., Šebej, P., Slavíček, P. & Klán, P. Nature of CTAB/Water/Chloroform Reverse Micelles at Above- and Subzero Temperatures Studied by NMR and Molecular Dynamics Simulations. *Langmuir* **31**, 8284–8293 (2015).
43. Kamboj, R. *et al.* Effect of cationic head group on micellization behavior of new amide-functionalized surface active ionic liquids. *Phys. Chem. Chem. Phys.* **16**, 26040–26050 (2014).
44. Tuckerman, M. E., Marx, D., Klein, M. L. & Parrinello, M. On the quantum nature of the shared proton in hydrogen bonds. *Science* **275**, 817–820 (1997).
45. Perrin, C. L. Are short, low-barrier hydrogen bonds unusually strong? *Acc. Chem. Res.* **43**, 1550–7 (2010).
46. Shokri, A., Wang, Y., O’Doherty, G. A., Wang, X. Bin & Kass, S. R. Hydrogen-bond networks: Strengths of different types of hydrogen bonds and an alternative to the low barrier hydrogen-bond proposal. *J. Am. Chem. Soc.* **135**, 17919–17924 (2013).

47. Ishikita, H. & Saito, K. Proton transfer reactions and hydrogen-bond networks in protein environments. *J. R. Soc. Interface* **11**, 1742–53 (2014).
48. Cleland, W. W. & Kreevoy, M. M. Low-barrier hydrogen bonds and enzymic catalysis. *Science* **44**, 1–17 (1994).
49. Schiøtt, B., Iversen, B. B., Madsen, G. K. H., Larsen, F. K. & Bruice, T. C. On the electronic nature of low-barrier hydrogen bonds in enzymatic reactions. *Proc. Natl. Acad. Sci. U. S. A.* **95**, 12799–12802 (1998).
50. Dai, S. *et al.* Low-barrier hydrogen bonds in enzyme cooperativity. *Nature* **573**, 609–613 (2019).
51. Wand, A. J. Bringing disorder and dynamics in protein allostery into focus. *Proc. Natl. Acad. Sci. U. S. A.* **114**, 4278–4280 (2017).
52. Nucci, N. V., Pometun, M. S. & Wand, A. J. Site-resolved measurement of water-protein interactions by solution NMR. *Nat. Struct. Mol. Biol.* **18**, 245–249 (2011).
53. Barel, D. & Black, C. A. Effect of neutralization and addition of urea, sucrose, and various glycols on phosphorus absorption and leaf damage from foliar-applied phosphate. *Plant Soil* **52**, 515–525 (1979).
54. Krank, H. S. & Franks, F. Structural approach to the solvent power of water for hydrocarbons; Urea as a structure breaker. *J. Chem. Phys.* **48**, 4746–4757 (1968).
55. Graziano, G. Size and temperature dependence of hydrocarbon solubility in concentrated aqueous solutions of urea and guanidine hydrochloride. *Can. J. Chem.* **80**, 388–400 (2002).
56. Inoue, Y., Niiyama, D., Murata, I. & Kanamoto, I. Usefulness of Urea as a Means of Improving the Solubility of Poorly Water-Soluble Ascorbyl Palmitate. *Int. J. Med. Chem.* **2017**, 1–9 (2017).

57. Rossky, P. J. Protein denaturation by urea: Slash and bond. *Proc. Natl. Acad. Sci. U. S. A.* **105**, 16825–16826 (2008).
58. Bennion, B. J. & Daggett, V. The molecular basis for the chemical denaturation of proteins by urea. *Proc. Natl. Acad. Sci. U. S. A.* **100**, 5142–5147 (2003).
59. Thapa, U. & Ismail, K. Urea effect on aggregation and adsorption of sodium dioctylsulfosuccinate in water. *J. Colloid Interface Sci.* **406**, 172–177 (2013).
60. Kumar, S., Parveen, N. & Kabir-Ud-Din. Effect of urea addition on micellization and the related phenomena. *J. Phys. Chem. B* **108**, 9588–9592 (2004).
61. Zangi, R., Zhou, R. & Berne, B. J. Urea's action on hydrophobic interactions. *J. Am. Chem. Soc.* **131**, 1535–1541 (2009).
62. Kallies, B. Coupling of solvent and solute dynamics - Molecular dynamics simulations of aqueous urea solutions with different intramolecular potentials. *Phys. Chem. Chem. Phys.* **4**, 86–95 (2002).
63. Idrissi, A. *et al.* The effect of urea on the structure of water: A molecular dynamics simulation. *J. Phys. Chem. B* **114**, 4731–4738 (2010).
64. Choa, H. S. *et al.* Protein structural dynamics in solution unveiled via 100-ps time-resolved x-ray scattering. *Proc. Natl. Acad. Sci. U. S. A.* (2010) doi:10.1073/pnas.1002951107.
65. Stumpe, M. C. & Grubmüller, H. Aqueous urea solutions: Structure, energetics, and urea aggregation. *J. Phys. Chem. B* **111**, 6220–6228 (2007).
66. Caballero-Herrera, A., Nordstrand, K., Berndt, K. D. & Nilsson, L. Effect of urea on peptide conformation in water: Molecular dynamics and experimental characterization. *Biophys. J.* **89**, 842–857 (2005).

67. Soper, A. K., Castner, E. W. & Luzar, A. Impact of urea on water structure: A clue to its properties as a denaturant? *Biophys. Chem.* **105**, 649–666 (2003).
68. Kameda, Y. & Amo, Y. Partial Pair Correlation Functions of Highly Concentrated Aqueous Urea Solutions Determined by Neutron Diffraction with  $^{14}\text{N}/^{15}\text{N}$  and H/D Isotopic Substitution Methods. *Bull Chem Soc Jpn* **83**, 131–144 (2010).
69. Chitra, R. & Smith, P. E. Molecular association in solution: A Kirkwood-Buff analysis of sodium chloride, ammonium sulfate, guanidinium chloride, urea, and 2,2,2-trifluoroethanol in water. *J. Phys. Chem. B* **106**, 1491–1500 (2002).
70. Ohta, K., Tayama, J., Saito, S. & Tominaga, K. Vibrational Frequency Fluctuation of Ions in. *Acc. Chem. Res.* **45**, 1982–1991 (2012).
71. Hoccart, X. & Turrell, G. Raman spectroscopic investigation of the dynamics of urea-water complexes. *J. Chem. Phys.* **99**, 8498–8503 (1993).
72. Sharp, K. A., Madan, B., Manas, E. & Vanderkooi, J. M. Water structure changes induced by hydrophobic and polar solutes revealed by simulations and infrared spectroscopy. *J. Chem. Phys.* **114**, 1791–1796 (2001).
73. Grdadolnik, J. & Maréchal, Y. Urea and urea-water solutions - An infrared study. *J. Mol. Struct.* **615**, 177–189 (2002).
74. Knight, A. W., Kalugin, N. G., Coker, E. & Ilgen, A. G. Water properties under nano-scale confinement. *Sci. Rep.* **9**, 1–12 (2019).
75. Alba-Simionesco, C. *et al.* Effects of confinement on freezing and melting. *Journal of Physics Condensed Matter* 1–68 (2006) doi:10.1088/0953-8984/18/6/R01.
76. Takaiwa, D., Hatano, I., Koga, K. & Tanaka, H. Phase diagram of water in carbon nanotubes. *Proc. Natl. Acad. Sci. U. S. A.* **105**, 39–43 (2008).

77. Thostenson, E. T., Ren, Z. & Chou, T. W. Advances in the science and technology of carbon nanotubes and their composites: A review. *Compos. Sci. Technol.* **61**, 1899–1912 (2001).
78. Iijima, S. Helical microtubules of graphitic carbon. *Nature* **354**, 56–58 (1991).
79. Wilson-Kubalek, E. M., Brown, R. E., Celia, H. & Milligan, R. A. Lipid nanotubes as substrates for helical crystallization of macromolecules. *Proc. Natl. Acad. Sci. U. S. A.* **95**, 8040–5 (1998).
80. Ilgen, A. G. *et al.* Defining silica-water interfacial chemistry under nanoconfinement using lanthanides. *Environ. Sci. Nano* **8**, 432–443 (2021).
81. Kumarasinghe, R., Ito, T. & Higgins, D. A. Nanoconfinement and mass transport in silica mesopores: The role of charge at the single molecule and single pore levels. *Anal. Chem.* **92**, 1416–1423 (2020).
82. Chowdhury, S. R., Schmuhl, R., Keizer, K., Ten Elshof, J. E. & Blank, D. H. A. Pore size and surface chemistry effects on the transport of hydrophobic and hydrophilic solvents through mesoporous  $\gamma$ -alumina and silica MCM-48. *J. Membr. Sci.* **225**, 177–186 (2003).
83. Ding, Y. & Riediker, M. A system to create stable nanoparticle aerosols from Nanopowders. *J. Vis. Exp.* **2016**, (2016).
84. Palmer, N. J., Eskici, G. & Axelsen, P. H. Non-Equilibrium Mass Exchange in AOT Reverse Micelles. *J. Phys. Chem. B* **124**, 144–148 (2020).
85. Eskici, G. & Axelsen, P. H. The size of AOT reverse micelles. *J. Phys. Chem. B* **120**, 11337–11347 (2016).
86. Yamamoto, K., Ota, N. & Tanaka, Y. Nanofluidic Devices and Applications for Biological Analyses. *Anal. Chem.* **93**, 332–349 (2021).

87. Chakraborty, A., Sarkar, M. & Basak, S. Stabilizing effect of low concentrations of urea on reverse micelles. *J. Colloid Interface Sci.* **287**, 312–317 (2005).
88. Ceraulo, L., Dormond, E., Mele, A. & Turco Liveri, V. FT-IR and nuclear overhauser enhancement study of the state of urea confined in AOT-reversed micelles. *Colloids Surf. Physicochem. Eng. Asp.* **218**, 255–264 (2003).
89. Caponetti, E. *et al.* Structure of urea clusters confined in AOT reversed micelles. *Langmuir* **19**, 4913–4922 (2003).
90. Higgins, C. Urea and the clinical value of measuring blood urea concentration. *Acute Care Testing. Org* 1–6 (2016).
91. Miller, S. L., Wiebenga-Sanford, B. P., Rithner, C. D. & Levinger, N. E. Nanoconfinement Raises the Energy Barrier to Hydrogen Atom Exchange between Water and Glucose. *J. Phys. Chem. B* **125**, 3364–3373 (2021).
92. Gale, C. D., Derakhshani-Molayousefi, M. & Levinger, N. E. How to Characterize Amorphous Shapes: The Tale of a Reverse Micelle. *J. Phys. Chem. B* **126**, 953–963 (2022).
93. Afzal, S., Lone, M. S., Nazir, N. & Dar, A. A. PH Changes in the Micelle-Water Interface of Surface-Active Ionic Liquids Dictate the Stability of Encapsulated Curcumin: An Insight through a Unique Interfacial Reaction between Arenediazonium Ions and t-Butyl Hydroquinone. *ACS Omega* **6**, 14985–15000 (2021).
94. Finer, E. G., Franks, F. & Tait, M. J. Nuclear magnetic resonance studies of aqueous urea solutions. *J. Am. Chem. Soc.* **94**, 4424–4429 (1972).
95. Stabinska, J. *et al.* Proton exchange in aqueous urea solutions measured by water-exchange (WEX) NMR spectroscopy and chemical exchange saturation transfer (CEST) imaging in vitro. *Magn. Reson. Med.* **82**, 935–947 (2019).

96. Sinibaldi, R. *et al.* SANS/SAXS study of the BSA solvation properties in aqueous urea solutions via a global fit approach. *Eur. Biophys. J.* **37**, 673–681 (2008).
97. Negrão, S., Schmöckel, S. M. & Tester, M. Evaluating physiological responses of plants to salinity stress. *Ann. Bot.* **119**, 1–11 (2017).
98. Welles, L., Lopez-Vazquez, C. M., Hooijmans, C. M., van Loosdrecht, M. C. M. & Brdjanovic, D. Impact of salinity on the anaerobic metabolism of phosphate-accumulating organisms (PAO) and glycogen-accumulating organisms (GAO). *Appl. Microbiol. Biotechnol.* **98**, 7609–7622 (2014).
99. Radko, S. P., Stastna, M. & Chrambach, A. Size-Dependent Electrophoretic Migration and Separation of Liposomes by Capillary Zone Electrophoresis in Electrolyte Solutions of Various Ionic Strengths. *Anal. Chem.* **72**, 5955–5960 (2000).
100. Lawal, O. S. Functionality of African locust bean (*Parkia biglobosa*) protein isolate: effects of pH, ionic strength and various protein concentrations. *Food Chem.* **86**, 345–355 (2004).
101. Nobrega, J. A. & Rocha, F. R. P. Ionic Strength Effect on the Rate of Reduction of Hexacyanoferrate(III) by Ascorbic Acid: A Flow Injection Kinetic Experiment. *J. Chem. Educ.* **74**, 560 (1997).
102. Lee, K. H., Ryu, H. S. & Rhee, K. C. Protein solubility characteristics of commercial soy protein products. *J. Am. Oil Chem. Soc.* **80**, 85–90 (2003).
103. Luo, Z.-X., Xing, Y.-Z., Ling, Y.-C., Kleinhammes, A. & Wu, Y. Electroneutrality breakdown and specific ion effects in nanoconfined aqueous electrolytes observed by NMR. *Nat. Commun.* **6**, 6358 (2015).

104. Zhou, K. & Xu, Z. Nanoconfinement-Enforced Ion Correlation and Nanofluidic Ion Machinery. *Nano Lett.* **20**, 8392–8398 (2020).
105. Diao, Y. & Espinosa-Marzal, R. M. Molecular insight into the nanoconfined calcite–solution interface. *Proc. Natl. Acad. Sci.* **113**, 12047–12052 (2016).
106. Urano, R., Pantelopulos, G. A., Song, S. & Straub, J. E. Characterization of dynamics and mechanism in the self-assembly of AOT reverse micelles. *J. Chem. Phys.* **149**, 144901 (2018).
107. Eskici, G. & Axelsen, P. H. The Size of AOT Reverse Micelles. *J. Phys. Chem. B* **120**, 11337–11347 (2016).
108. Palmer, N. J., Eskici, G. & Axelsen, P. H. Non-Equilibrium Mass Exchange in AOT Reverse Micelles. *J. Phys. Chem. B* **124**, 144–148 (2020).
109. Van Horn, W. D., Ogilvie, M. E. & Flynn, P. F. Use of reverse micelles in membrane protein structural biology. *J. Biomol. NMR* **40**, 203–211 (2008).
110. Chang, G.-G., Huang, T.-M. & Hung, H.-C. Reverse Micelles as Life-Mimicking Systems. 12.
111. Zhou, D., Wei, Q., Wang, S., Li, X. & Bian, H. Counterion Effect on Vibrational Relaxation and the Rotational Dynamics of Interfacial Water and an Anionic Vibrational Probe in the Confined Reverse Micelles Environment. *J. Phys. Chem. Lett.* **10**, 176–182 (2019).
112. Faeder, J. & Ladanyi, B. M. Molecular Dynamics Simulations of the Interior of Aqueous Reverse Micelles. *J. Phys. Chem. B* **104**, 1033–1046 (2000).
113. Baryames, C. P., Teel, M. & Baiz, C. R. Interfacial H-Bond Dynamics in Reverse Micelles: The Role of Surfactant Heterogeneity. *Langmuir* **35**, 11463–11470 (2019).

114. Chowdhary, J. & Ladanyi, B. M. Molecular Dynamics Simulation of Aerosol-OT Reverse Micelles. *J. Phys. Chem. B* **113**, 15029–15039 (2009).
115. Smith, A. M., Lee, A. A. & Perkin, S. The Electrostatic Screening Length in Concentrated Electrolytes Increases with Concentration. *J. Phys. Chem. Lett.* **7**, 2157–2163 (2016).
116. Gebbie, M. A., Dobbs, H. A., Valtiner, M. & Israelachvili, J. N. Long-range electrostatic screening in ionic liquids. *Proc. Natl. Acad. Sci.* **112**, 7432–7437 (2015).
117. Ridley, R. E., Fathi-Kelly, H., Kelly, J. P., Vasquez, V. R. & Graeve, O. A. Predicting the size of salt-containing aqueous Na-AOT reverse micellar water-in-oil microemulsions with consideration for specific ion effects. *J. Colloid Interface Sci.* **586**, 830–835 (2021).
118. Ridley, R. E., Fathi-Kelly, H., Kelly, J. P., Vasquez, V. R. & Graeve, O. A. Predicting Destabilization in Salt-Containing Aqueous Reverse Micellar Colloidal Systems. *ACS Earth Space Chem.* **5**, 2223–2232 (2021).
119. Piletic, I. R., Moilanen, D. E., Spry, D. B., Levinger, N. E. & Fayer, M. D. Testing the Core/Shell Model of Nanoconfined Water in Reverse Micelles Using Linear and Nonlinear IR Spectroscopy. *J. Phys. Chem. A* **110**, 4985–4999 (2006).
120. Danielson, M. A. & Falke, J. J. Use of  $^{19}\text{F}$  NMR to Probe Protein Structure and Conformational Changes. *Annu. Rev. Biophys. Biomol. Struct.* **25**, 163–195 (1996).
121. Hinterholzinger, F. M., Rühle, B., Wuttke, S., Karaghiosoff, K. & Bein, T. Highly sensitive and selective fluoride detection in water through fluorophore release from a metal-organic framework. *Sci. Rep.* **3**, 2562 (2013).

122. Isbester, P. K., Brandt, J. L., Kestner, T. A. & Munson, E. J. High-Resolution Variable-Temperature  $^{19}\text{F}$  MAS NMR Spectroscopy of Vinylidene Fluoride Based Fluoropolymers. *Macromolecules* **31**, 8192–8200 (1998).
123. Thorarinsdottir, A. E., Gaudette, A. I. & Harris, T. D. Spin-crossover and high-spin iron(II) complexes as chemical shift  $^{19}\text{F}$  magnetic resonance thermometers. *Chem. Sci.* **8**, 2448–2456 (2017).
124. Fathi, H., Kelly, J. P., Vasquez, V. R. & Graeve, O. A. Ionic Concentration Effects on Reverse Micelle Size and Stability: Implications for the Synthesis of Nanoparticles. *Langmuir* **28**, 9267–9274 (2012).
125. Stahla, M. L. *et al.*  $^1\text{H}$  NMR Studies of Aerosol-OT Reverse Micelles with Alkali and Magnesium Counterions: Preparation and Analysis of MAOTs. *Langmuir* **24**, 6027–6035 (2008).
126. National Library of Medicine. Hydrofluoric Acid. (2010).
127. Malinowski, E. R., Knapp, P. S. & Feuer, B. NMR Studies of Aqueous Electrolyte Solutions. I. Hydration Number of NaCl Determined from Temperature Effects on Proton Shift. *J. Chem. Phys.* **45**, 4274–4279 (1966).
128. Fenn, E. E., Wong, D. B. & Fayer, M. D. Water dynamics at neutral and ionic interfaces. *Proc. Natl. Acad. Sci.* **106**, 15243–15248 (2009).
129. Shang, W. *et al.* Shape and Size Controlled Synthesis of MOF Nanocrystals with the Assistance of Ionic Liquid Microemulsions. *Langmuir* **29**, 13168–13174 (2013).
130. Hendon, C. H., Rieth, A. J., Korzyński, M. D. & Dincă, M. Grand Challenges and Future Opportunities for Metal–Organic Frameworks. *ACS Cent. Sci.* **3**, 554–563 (2017).

131. Donovan, A. J., Kalkowski, J., Smith, S. A., Morrissey, J. H. & Liu, Y. Size-Controlled Synthesis of Granular Polyphosphate Nanoparticles at Physiologic Salt Concentrations for Blood Clotting. *Biomacromolecules* **15**, 3976–3984 (2014).
132. Sebastian, L. & Gopalakrishnan, J. Lithium ion mobility in metal oxides: a materials chemistry perspective Based on a lecture delivered at the international symposium “Materials for Energy: Batteries and Fuel Cells”, November 2002, Madrid, Spain. *J. Mater. Chem.* **13**, 433–441 (2003).
133. Alikin, D. O. *et al.* Characterization of  $\text{LiMn}_2\text{O}_4$  cathodes by electrochemical strain microscopy. *Appl. Phys. Lett.* **108**, 113106 (2016).
134. Prakash, G. K. S. *et al.* Nafion-Ru: A Sustainable Catalyst for Selective Hydration of Nitriles to Amides. *Asian J. Org. Chem.* **1**, 146–149 (2012).
135. Jo, C., Pugal, D., Oh, I.-K., Kim, K. J. & Asaka, K. Recent advances in ionic polymer–metal composite actuators and their modeling and applications. *Prog. Polym. Sci.* **38**, 1037–1066 (2013).
136. Heitner-Wirguin, C. Recent advances in perfluorinated ionomer membranes: structure, properties and applications. *J. Membr. Sci.* **120**, 1–33 (1996).
137. Spry, D. B., Goun, A., Glusac, K., Moilanen, D. E. & Fayer, M. D. Proton Transport and the Water Environment in Nafion Fuel Cell Membranes and AOT Reverse Micelles. *J. Am. Chem. Soc.* **129**, 8122–8130 (2007).
138. Saito, Y., Takeda, S., Nakadate, J., Sasaki, T. & Cho, T. Factors Determining Ionic Mobility in Ion Migration Pathways of Polypropylene (PP) Separator for Lithium Secondary Batteries. *J. Phys. Chem. C* **123**, 21888–21895 (2019).

139. Kreibig, S. D. Autonomic nervous system activity in emotion: A review. *Biol. Psychol.* **84**, 394–421 (2010).
140. Wiebenga-Sanford, B. P. *et al.* Sweet Confinement: Glucose and Carbohydrate Osmolytes in Reverse Micelles. *J. Phys. Chem. B* **122**, 9555–9566 (2018).
141. Muñoz-Santiburcio, D., Wittekindt, C. & Marx, D. Nanoconfinement effects on hydrated excess protons in layered materials. *Nat. Commun.* **4**, 2349 (2013).
142. Nakama, Y. Surfactants. in *Cosmetic Science and Technology* 231–244 (Elsevier, 2017). doi:10.1016/B978-0-12-802005-0.00015-X.
143. Li, Z., Williams, A. L. & Rood, M. J. Influence of Soluble Surfactant Properties on the Activation of Aerosol Particles Containing Inorganic Solute. *J. Atmospheric Sci.* **55**, 1859–1866 (1998).
144. Nakama, Y. Surfactants. in *Cosmetic Science and Technology* 231–244 (Elsevier, 2017). doi:10.1016/B978-0-12-802005-0.00015-X.
145. Lin, B., McCormick, A. V., Davis, H. T. & Strey, R. Solubility of sodium soaps in aqueous salt solutions. *J. Colloid Interface Sci.* **291**, 543–549 (2005).
146. Stehle, R. *et al.* An enzyme containing microemulsion based on skin friendly oil and surfactant as decontamination medium for organo phosphates: Phase behavior, structure, and enzyme activity. *J. Colloid Interface Sci.* **413**, 127–132 (2014).
147. Mattei, M., Kontogeorgis, G. M. & Gani, R. A comprehensive framework for surfactant selection and design for emulsion based chemical product design. *Fluid Phase Equilibria* **362**, 288–299 (2014).
148. Jain, S. & Bates, F. S. On the Origins of Morphological Complexity in Block Copolymer Surfactants. *Science* **300**, 460–464 (2003).

149. Lourith, N. & Kanlayavattanakul, M. Natural surfactants used in cosmetics: glycolipids. *Int. J. Cosmet. Sci.* **31**, 255–261 (2009).
150. Kogan, A. & Garti, N. Microemulsions as transdermal drug delivery vehicles. *Adv. Colloid Interface Sci.* **123–126**, 369–385 (2006).
151. Kitamoto, D., Morita, T., Fukuoka, T., Konishi, M. & Imura, T. Self-assembling properties of glycolipid biosurfactants and their potential applications. *Curr. Opin. Colloid Interface Sci.* **14**, 315–328 (2009).
152. Mohd. Yasir, Som, I. & Bhatia, K. Status of surfactants as penetration enhancers in transdermal drug delivery. *J. Pharm. Bioallied Sci.* **4**, 2 (2012).
153. Tsai, P.-C. & Ding, W.-H. Determination of alkyltrimethylammonium surfactants in hair conditioners and fabric softeners by gas chromatography–mass spectrometry with electron-impact and chemical ionization. *J. Chromatogr. A* **1027**, 103–108 (2004).
154. Gavazzoni Dias, M. F. R. Pro and Contra of Cleansing Conditioners. *Skin Appendage Disord.* **5**, 131–134 (2019).
155. Falk, N. A. Surfactants as Antimicrobials: A Brief Overview of Microbial Interfacial Chemistry and Surfactant Antimicrobial Activity. *J. Surfactants Deterg.* jsde.12293 (2019) doi:10.1002/jsde.12293.
156. Viscardi, G. *et al.* Synthesis and Surface and Antimicrobial Properties of Novel Cationic Surfactants. *J. Org. Chem.* **65**, 8197–8203 (2000).
157. Vagias, A., Suszynski, W. L., Davis, H. T. & McCormick, A. V. Krafft Temperature of Cesium Dodecylsulfate Solutions at High Concentration. *J. Chem. Eng. Data* **62**, 1623–1627 (2017).

158. Łuczak, J., Jungnickel, C., Joskowska, M., Thöming, J. & Hupka, J. Thermodynamics of micellization of imidazolium ionic liquids in aqueous solutions. *J. Colloid Interface Sci.* **336**, 111–116 (2009).
159. Ropers, M. H., Czichocki, G. & Brezesinski, G. Counterion Effect on the Thermodynamics of Micellization of Alkyl Sulfates. *J. Phys. Chem. B* **107**, 5281–5288 (2003).
160. Khan, H. *et al.* Effect of glycerol with sodium chloride on the Krafft point of sodium dodecyl sulfate using surface tension. *J. Colloid Interface Sci.* **538**, 75–82 (2019).
161. Summerton, E. *et al.* Nuclear magnetic resonance and small-angle X-ray scattering studies of mixed sodium dodecyl sulfate and N,N-dimethyldodecylamine N-oxide aqueous systems performed at low temperatures. *J. Colloid Interface Sci.* **535**, 1–7 (2019).
162. Parmar, A., Aswal, V. K. & Bahadur, P. Interaction between the ionic liquids 1-alkyl-3-methylimidazolium tetrafluoroborate and Pluronic® P103 in aqueous solution: A DLS, SANS and NMR study. *Spectrochim. Acta. A. Mol. Biomol. Spectrosc.* **97**, 137–143 (2012).
163. Dharaiya, N. & Bahadur, P. Phenol induced growth in Triton X-100 micelles: Effect of pH and phenols' hydrophobicity. *Colloids Surf. Physicochem. Eng. Asp.* **410**, 81–90 (2012).
164. Sachin, K. M., Karpe, S. A., Singh, M. & Bhattarai, A. Self-assembly of sodium dodecylsulfate and dodecyltrimethylammonium bromide mixed surfactants with dyes in aqueous mixtures. *R. Soc. Open Sci.* **6**, 181979 (2019).
165. R. Dorshow, J. Briggs, C. A. Bunton, D.F. Nicoli. Dynamic light scattering from cetyltrimethylammonium bromide micelles. Intermicellar interactions at low ionic strengths. *J. Phys. Chem.* **86**, 2388–2395 (1982).

166. Ren, B., Gao, Y., Lu, L., Liu, X. & Tong, Z. Aggregates of alginates binding with surfactants of single and twin alkyl chains in aqueous solutions: Fluorescence and dynamic light scattering studies. *Carbohydr. Polym.* **66**, 266–273 (2006).
167. Edward, J. T. Molecular volumes and the Stokes-Einstein equation. *J. Chem. Educ.* (2009) doi:10.1021/ed047p261.
168. Cruz Barrios, E. & Annunziata, O. Determination of Critical Micelle Concentration from the Diffusion-Driven Dilution of Micellar Aqueous Mixtures. *Langmuir* **37**, 2855–2862 (2021).
169. Manojlovic, J. The Krafft temperature of surfactant solutions. *Therm. Sci.* **16**, 631–640 (2012).
170. Tcacenco, C. M., Zana, R. & Bales, B. L. Effect of the Nature of the Counterion on the Properties of Anionic Surfactants. 5. Self-Association Behavior and Micellar Properties of Ammonium Dodecyl Sulfate. *J. Phys. Chem. B* **109**, 15997–16004 (2005).
171. Cao, C. & Long, Y.-T. Biological Nanopores: Confined Spaces for Electrochemical Single-Molecule Analysis. *Acc. Chem. Res.* **51**, 331–341 (2018).
172. Kohen, A. & Klinman, J. P. Hydrogen tunneling in biology. *Chem. Biol.* **6**, R191–R198 (1999).
173. Senoo, H. *et al.* Accumulation of Vitamin A in the Hepatic Stellate Cell of Arctic Top Predators. *Anat. Rec. Adv. Integr. Anat. Evol. Biol.* **295**, 1660–1668 (2012).
174. Miller, S. L. & Levinger, N. E. Urea Disrupts the AOT Reverse Micelle Structure at Low Temperatures. *Langmuir* **38**, 7413–7421 (2022).
175. Das, A. & Mukhopadhyay, C. Urea-Mediated Protein Denaturation: A Consensus View. *J. Phys. Chem. B* **113**, 12816–12824 (2009).

176. Fernandes, H. P., Cesar, C. L. & Barjas-Castro, M. de L. Electrical properties of the red blood cell membrane and immunohematological investigation. 5.

## APPENDIX 1: SUPPLEMENTAL INFORMATION- EXCHANGE DYNAMICS OF GLUCOSE IN REVERSE MICELLES

**Co-Author Attribution and Description of work Distribution:** Selection of the EXSY pulse sequence and customization of general settings were determined by Benjamin Wiebenga-Sanford and Chris Rithner. Chris Rithner consulted on instrumentation trouble shooting and temperature dependent measurements. Dr. Joseph DiVerdi is acknowledged as being especially crucial in discussions linking the kinetic model to the physical phenomena occurring during the EXSY NMR measurement. All NMR, DLS, and DSC figures were collected and prepared independently by Samantha Miller with the satellite support of the Analytical Research Core staff at Colorado State University. Co-Author and PI Nancy Levinger aided in the preparation, editing, and submission of the manuscript.

**Description of EXSY experiment:** The EXSY NMR experiments were conducted on a Varian 500 MHz Spectrometer with both a TRIAX and HFCN probe using a variable temperature controller. The EXSY NMR experiment was queued under the common experiments tab and labelled “NOESY1D.” This action immediately prompts the inclusion of a 1D  $^1\text{H}$  NMR pulse sequence necessary for defining the range (in Hz) of the water peak. Manually define the range of the excitation by clicking the button “set box cursor” and typing in “cr=” and “dr=” into the Varian command prompt. Note that values are understood to be in Hz unless “p” immediately follows the numerical values that follow the equal sign. The console displays the range you have assigned with the presence of two light blue lines around the chosen area. Ensure these are sufficiently encompassing the range of the water peak.

To define the mixing array of the 1D NOESY (EXSY) NMR experiment, type “MixN” into the Varian dialog box. The values chosen on this console are understood to be in seconds by the console. The length of the array defined should match the left number in the box “length.” This should automatically update after manually defining values. Clicking close will automatically save the new mixing time array. This can be double checked by simply reopening the mixing array by typing in “mixN” again. After defining the mixing array, the only other settings that need to be adjusted are turning off the ZQ filter (unclick this box) and adjusting power and gain if desired. Ensure you run a “mix n=0” spectrum by clicking the box next to this feature. It will ask you to define the number of scans for this spectrum. Choose eight unless you are worried about S/N, in which case you should chose 16. Power and gain should be modulated according to desired S/N. Run a preliminary, independent 1D <sup>1</sup>H NMR spectrum on the sample to assess the quality of the spectra. Generally, the S/N did not begin to suffer until hitting five degrees celcius. You will not be able to pause the experiment after the automatic 1D <sup>1</sup>H NMR that queues without resetting the EXSY NMR experimental conditions. Record the values of power, gain, and the lock signal should spectral quality need improvement after your EXSY experiment is processed and analyzed.

### Custom Matlab Code for extracting $k_1$ :

```
function [fitresult, gof] = createFit(X2, Y2)
%CREATEFIT(X2,Y2)
% Create a fit.
%
% Data for 'alpha-glucose_temp25_int.vs.int_with_errors_1' fit:
%   X Input : X2
%   Y Output: Y2
% Output:
%   fitresult : a fit object representing the fit.
%   gof : structure with goodness-of fit info.
%
% See also FIT, CFIT, SFIT.
```

```
%% Fit: 'untitled fit 1'.
% first define x and y variable arrays
```

```
X2= [0
0.002
0.01
0.05
0.07
0.1
0.2
0.4
0.6
0.8
1
1.5
2
2.5
]
```

```
Y2= [24.14
464.27
683.145
1304.49
1443.845
1528.58
1422.145
1023.815
732.2
511.785
365.87
154.74
64.23
26.31
]
```

```
err = [1.99
47.16
70.54
151.01
172.77
193.61
180.74
129.14
```

```

88.61
56.06
40.21
14.71
8.20
0.85];

[xData, yData] = prepareCurveData( X2, Y2 );

% Set up fittype and options.
ft = fittype( 'a*(exp(-1*b*X2)-exp(-1*c*X2))*(b/(c-b))+d', 'independent',
'X2', 'dependent', 'y' );
opts = fitoptions( 'Method', 'NonlinearLeastSquares' ); %chose fitting type
opts.Display = 'Off';
opts.Lower = [1500 33.92 1.701 -Inf]; %this defines the lower fitting
constraints
opts.StartPoint = [1800 68 1.9 0.934]; %this defines the initial guesses
opts.Upper = [Inf Inf Inf 2.2]; %this defines the upper fitting constraints

% Fit model to data in x and y arrays.
[fitresult, gof] = fit( xData, yData, ft, opts );

% Plot fitted line with data in x and y arrays.
figure( 'Name', 'untitled fit 1' );
h = plot( fitresult, xData, yData ); %this creates the plot

hold on
errorbar(X2,Y2,err, '.', 'MarkerSize',28) %this adds the error bars
legend( h, 'Y2 vs. X2', 'untitled fit 1', 'Location', 'NorthEast' ); %this
plots the legend

% Label axes
xlabel X2
ylabel Y2
grid on

```

## Custom Matlab Code for Normalization and subsequent stacked plotting:

```
% Normalized Integrated Intensity versus mixing time
% This graph will plot multiple temperatures against each other
% Begin by defining the X and Y values for each temperature
% These plots correspond to the beta anomer
% Must keep "[xData, yData]= "

% Create Fit of Temp 30 Data

X1= [0
0.002
0.01
0.05
0.07
0.1
0.2
0.4
0.6
0.8
1
1.5
2
2.5
]

Y1= [53.77
783.97
1323.85
1944.91
1954.62
1858.93
1647.07
1217.09
914.07
668.30
496.43
232.55
115.88
70.14
]

[xData, yData] = prepareCurveData( X1, Y1 );

% Create Fit for Temp 25 Data

X2= [0
0.002
0.01
0.05
0.07
0.1
0.2
0.4
0.6
0.8
```

```

1
1.5
2
2.5
]

Y2= [38.83
931.58
1337.90
2247.86
2370.28
2389.76
2088.97
1486.48
1051.12
741.51
538.26
227.79
93.32
41.27
]

[x2Data, y2Data] = prepareCurveData( X2, Y2 );

% Create Fit for Temp 0 Data

X7= [0
0.002
0.01
0.05
0.07
0.1
0.2
0.4
0.6
0.8
1
1.5
2
2.5
]

Y7= [1.73
250.30
367.57
795.09
942.06
1141.36
1360.00
1154.29
799.40
515.45
335.99
111.04
46.61
17.52
]

```

```

[x7Data, y7Data] = prepareCurveData( X7, Y7 );

% Define Fit for Temp -15 Data

X9= [0
0.002
0.01
0.05
0.07
0.1
0.2
0.4
0.6
0.8
1
1.5
2
2.5
]

Y9= [7.51
57.28
130.00
301.48
387.37
470.43
593.97
540.46
386.76
262.32
178.74
78.15
50.71
22.55
]

[x9Data, y9Data] = prepareCurveData( X9, Y9 );

%% NORMALIZATION
% Now normalize the data where I(max)=1 using the table columns

N = normalize(T, 'norm', Inf, 'DataVariables', {'Temp30', 'Temp25', 'Temp15'})

%% DEFINE ALL THE FITS
% This tells Matlab what equation to fit to each set of data
% The same equation is used for each data set since it's the same system
% This can be copied from "file>generate code" in cftool

%Set up fittype and options. Temp 30
ft = fittype( 'a*(exp(-1*b*X1)-exp(-1*c*X1))*(b/(c-b))+d', 'independent',
'X1', 'dependent', 'y' );
opts = fitoptions( 'Method', 'NonlinearLeastSquares' ); %this is the type
of fit
opts.Display = 'Off';
opts.StartPoint = [2100 80 1.459 13]; %initial guesses

```

```

    opts.Upper = [Inf Inf Inf 14]; %limits to initial guesses and resultant
fits

% Set up fittype and options. Temp 25
ft = fittype( 'a*(exp(-1*b*X2)-exp(-1*c*X2))*(b/(c-b))+d', 'independent',
'X2', 'dependent', 'y' );
    opts = fitoptions( 'Method', 'NonlinearLeastSquares' );
    opts.Display = 'Off';
    opts.Lower = [2645 111 1.514 -19];
    opts.StartPoint = [2645 111 1.514 -19.31];

% Set up fittype and options. Temp 0
ft = fittype( 'a*(exp(-1*b*X7)-exp(-1*c*X7))*(b/(c-b))+d', 'independent',
'X7', 'dependent', 'y' );
    opts = fitoptions( 'Method', 'NonlinearLeastSquares' );
    opts.Display = 'Off';
    opts.Lower = [-Inf -Inf 2.15 -Inf];
    opts.StartPoint = [1500 10 2.2 1];
    opts.Upper = [Inf Inf Inf 2.03];

% Set up fittype and options. Temp -15
ft = fittype( 'a*(exp(-1*b*X9)-exp(-1*c*X9))*(b/(c-b))+d', 'independent',
'X9', 'dependent', 'y' );
    opts = fitoptions( 'Method', 'NonlinearLeastSquares' );
    opts.Display = 'Off';
    opts.StartPoint = [800 5.1 0.9572 0.485375648722841];
    opts.Upper = [Inf 6.531 Inf 17.81];

%% Fit model to data.
% This part is also copied from the autogenerated code
% HOWEVER, you must add extra numbers to ensure you get different fit results
% For example fitresult became "fitresult2" and xData became "x2Data"

[fitresult, gof] = fit( xData, yData, ft, opts );
[fitresult2, gof2] = fit( x2Data, y2Data, ft, opts );
[fitresult7, gof7] = fit( x7Data, y7Data, ft, opts );
[fitresult9, gof9] = fit( x9Data, y9Data, ft, opts );

%% Plot fit with data.
% This section creates the actual plots, as labeled
% Each plot must call upon correct fitresult or wrote data will be on wrong
plot!

hold on; %typing hold on makes sure it stays on same graph when printed
figure( 'Name', 'untitled fit 1' );
    h = plot( fitresult, xData, yData ); %temp 30C

hold on
    h = plot( fitresult2, x2Data, y2Data ); %temp 25C

hold on
    h = plot( fitresult7, x7Data, y7Data ); %temp 0C

hold on
    h = plot( fitresult9, x9Data, y9Data ); %temp -15C

```

```
% Label axes
xlabel ('Mixing time (s)')
ylabel ('Integrated intensity')
grid on %the legend will print
hold off
```

**Table S1.2**

A table summarizing  $k_1$  and  $k_2$  rate constants and associated uncertainties for chemical exchange and subsequent spin-lattice relaxation of glucose hydroxyl groups. Values represent the average of three independent measurements. Because we cannot unequivocally assign the peaks to the specific position, peaks 3,4 down and 3,4 up are associated with hydroxyl groups at the 3 and 4 position on glucose.

Temp (K)	$\alpha$ -D-glucose		$\beta$ -D-glucose	
	$k_1$ (s <sup>-1</sup> )	$k_2$ (s <sup>-1</sup> )	$k_1$ (s <sup>-1</sup> )	$k_2$ (s <sup>-1</sup> )
304.15	85.7 ( $\pm$ 28.2)	1.2 ( $\pm$ 0.3)	125.3 ( $\pm$ 26.3)	1.2 ( $\pm$ 0.3)
298.15	51.1 ( $\pm$ 10.2)	1.2 ( $\pm$ 0.3)	89.5 ( $\pm$ 19.6)	1.3 ( $\pm$ 0.4)
288.15	14.7 ( $\pm$ 3.5)	1.8 ( $\pm$ 0.4)	23.9 ( $\pm$ 8.8)	1.9 ( $\pm$ 0.3)
283.15	11.1 ( $\pm$ 3.9)	1.9 ( $\pm$ 0.3)	14.8 ( $\pm$ 3.1)	1.9 ( $\pm$ 0.4)
273.15	8.9 ( $\pm$ 3.0)	1.9 ( $\pm$ 0.3)	13.9 ( $\pm$ 3.3)	1.9 ( $\pm$ 0.4)
268.15	8.1 ( $\pm$ 2.2)	1.9 ( $\pm$ 0.3)	7.5 ( $\pm$ 3.0)	2.1 ( $\pm$ 0.6)
264.15	6.8 ( $\pm$ 1.3)	1.8 ( $\pm$ 0.4)	5.9 ( $\pm$ 1.1)	2.2 ( $\pm$ 0.5)
258.15	7.2 ( $\pm$ 1.7)	1.9 ( $\pm$ 0.3)	5.8 ( $\pm$ 0.7)	2.4 ( $\pm$ 0.6)
252.15	5.5 ( $\pm$ 1.5)	2.7 ( $\pm$ 0.7)	5.5 ( $\pm$ 0.7)	2.3 ( $\pm$ 0.5)

**Table S1.3:**

Reported  $R^2$  values obtained after linearly fitting Arrhenius plots of temperature dependent exchange behavior for glucose loaded reverse micelles.

<b>Single Linear Fit</b>	
Single Linear Fit ( $\alpha$ -glucose)	0.913
Single Linear Fit ( $\beta$ -glucose)	0.901
<b>Two Part Linear Fit (<math>\alpha</math>-glucose)</b>	
High temperature Regime	0.987
Low temperature Regime	0.976
<b>Two Part Linear Fit (<math>\beta</math>-glucose)</b>	
High temperature Regime	0.999
Low temperature Regime	0.981

**Table S1.4:**

Various size distributions of  $w_0=10$  reverse micelles loaded with glucose at a 1 to 30 glucose to water ratio at different temperatures. Plot demonstrates that size of reverse micelles is temperature dependent. Average size increases as temperature increases. This suggests that water forms the stiff hydrogen bonds within the reverse micelle that may lead to an expansion of the reverse micelle core. However, the “increase” in average diameter could also be due to the increase in polydispersity, as indicated by the greater value for FWHM.

<b>Temp (K)</b>	<b>Hydrodynamic Diameter (nm)</b>
303	4.53
298	4.73
293	5.41
288	5.43
283	6.11
275	7.24

## APPENDIX 2: IMPACT OF UREA ON REVERSE MICELLE SYSTEMS

**Co-Author Attribution and Description of work Distribution:** All NMR, DLS, and figures were collected and prepared independently with the satellite support of the Analytical Research Core staff at Colorado State University. Co-Author and PI Nancy Levinger aided in the preparation, editing, and submission of the manuscript.

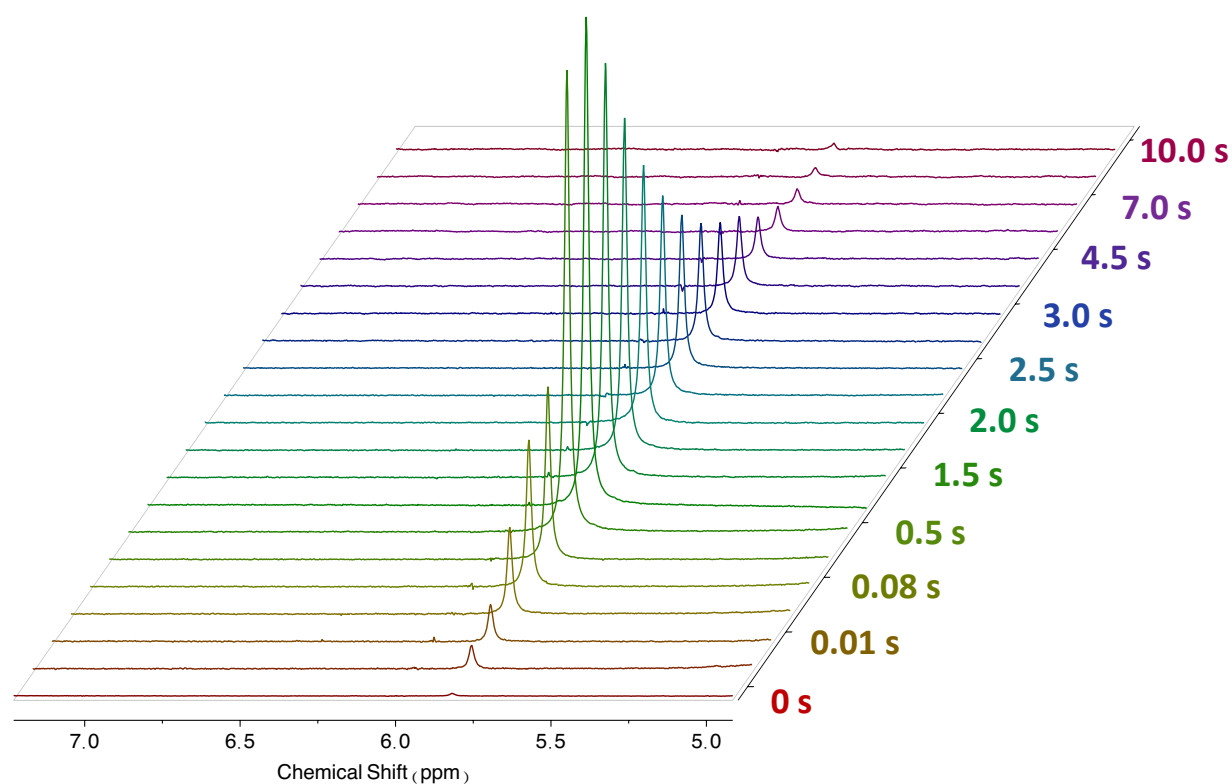


**Figure S2.1:** Stacked EXSY spectra collected at 298 K for 2 M urea in  $w_0=10$  reverse micelles. Mixing time is indicated to the right of the spectra. The initial increase in the featured urea NH peak represents the swift process of exchange that begins to slow after reaching a maxim exchange rate around 1.5 seconds.

**Table S2.2:** Data tables demonstrating raw integration values and the associated residual areas. The percentage values show that the area not captured by the fit consistently makes up than less than 5% of the overall area.

Trace: max	Temp K	Area, H2O (raw)	Area, Urea (raw)	Ratio (urea:H <sub>2</sub> O)	Residual, H2O (raw)	Residual, Urea (raw)	%error	%Error
$w_0=10$ RMs	298	95744.12	869.69	0.01	41.43	0.01	0.043	0.000
	273	818.72	85.04	0.10	0.17	0.00	0.000	0.000
$w_0=15$ RMs	298	96683.46	3102.64	0.03	2284.34	0.57	0.024	0.000
	273	322732	34128.52	0.11	66.04	2.40	0.000	0.000
$w_0=20$ RMs	298	102594.90	3011.95	0.03	2167.91	0.43	2.113	0.014
	273	319652	31021.68	0.10	62.56	1.73	0.020	0.006

**Figure S2.2:** 2D <sup>1</sup>H-NOESY NMR spectra for  $w_0=15$  AOT reverse micelles encapsulating 2 M aqueous urea at (A) 298 K and (B) 275 K. The dotted rectangles emphasize the expected crosspeak indicative of a water-urea interaction. Cross peaks indicating an interaction between the AOT headgroups and urea are noticeable absent.

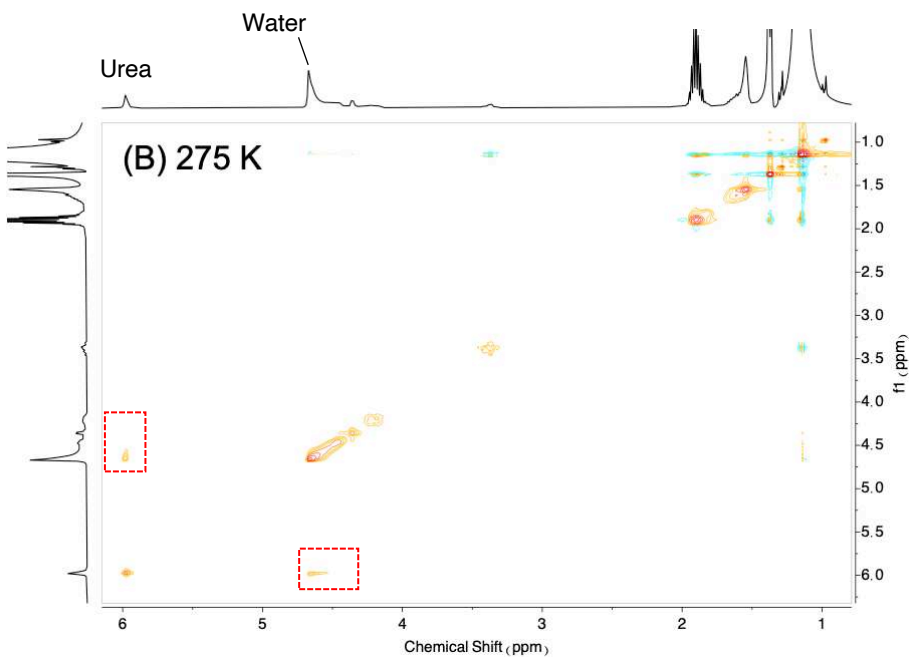
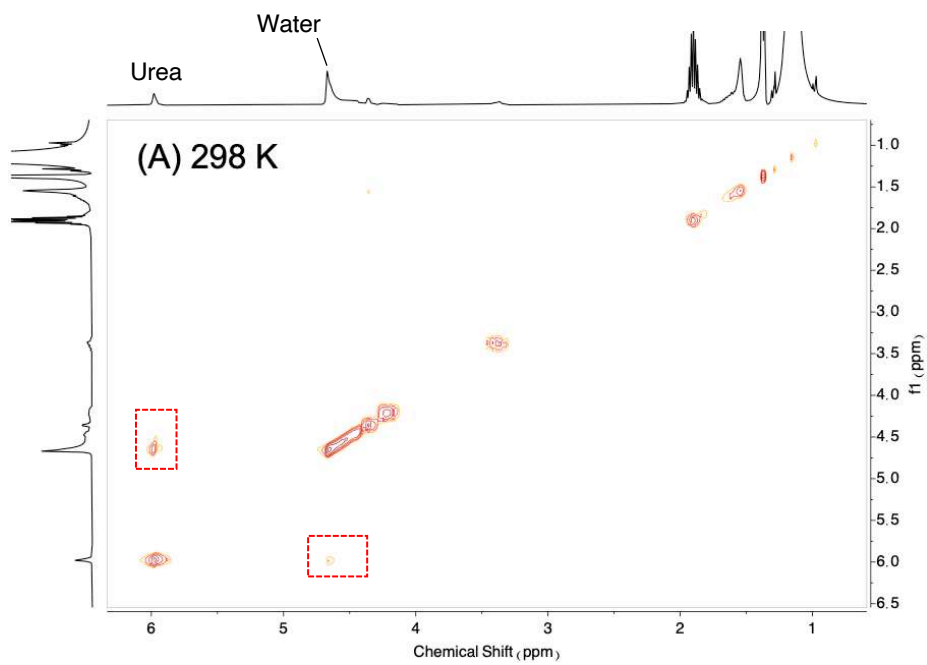
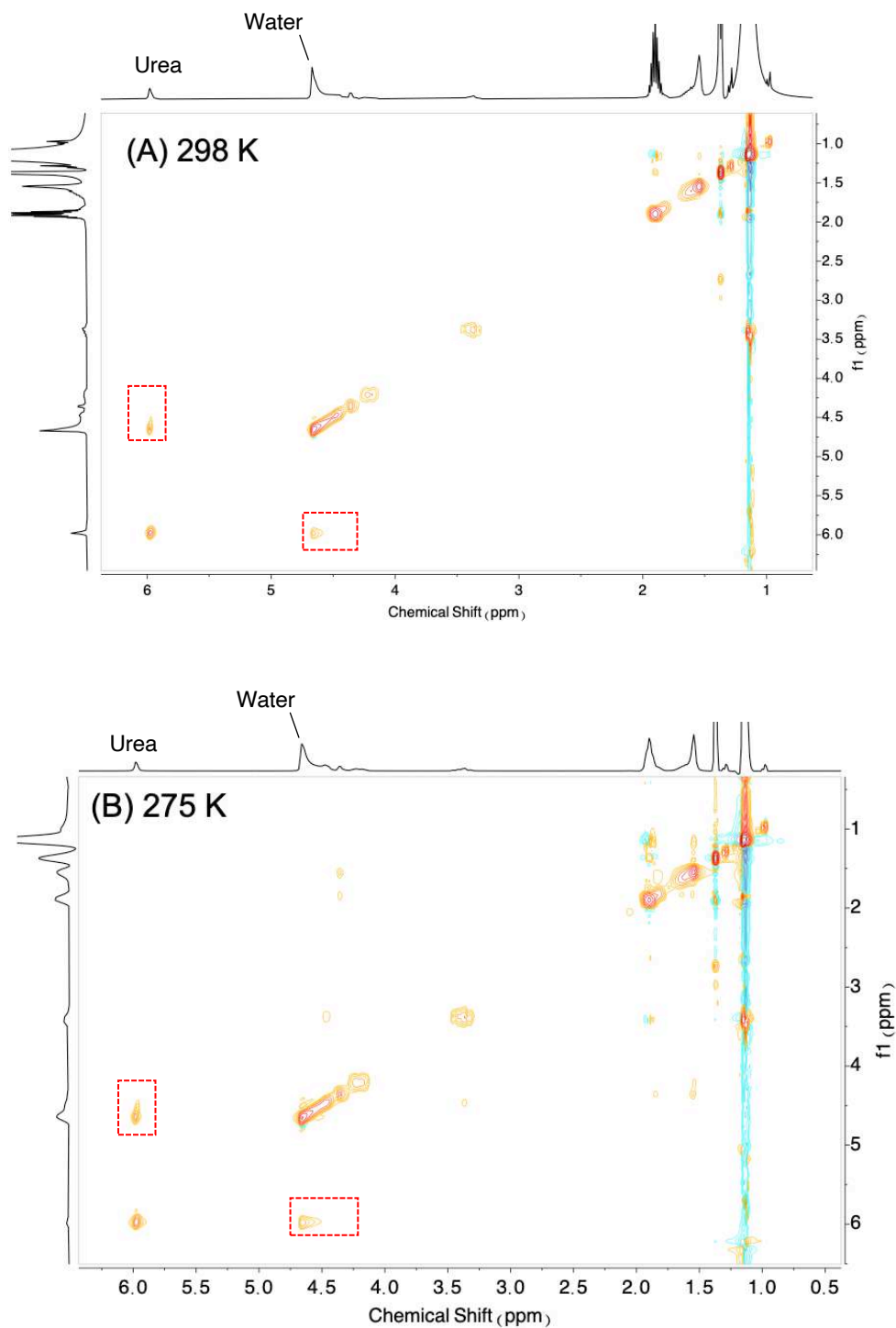


**Figure S2.3:** 2D  $^1\text{H}$ -NOESY NMR spectra for  $w_0=20$  AOT reverse micelles encapsulating 2 M aqueous urea at (A) 298 K and (B) 275 K. The dotted rectangles emphasize the expected crosspeak indicative of a water-urea interaction. Cross peaks indicating an interaction between the AOT headgroups and urea are noticeable absent.



### APPENDIX 3: IMPACT OF UREA ON REVERSE MICELLE SYSTEMS

**Co-Author Attribution and Description of work Distribution:** All  $^1\text{H}$  and  $^{19}\text{F}$  NMR data was collected by Ernestas Gaidamauskas and Ataf Ali Altaf, as guided by Debbie Crans. They initiated the project, collecting the preliminary DLS results and prepared all associated samples and figures. Final DLS data was collected by Sam Miller. The first manuscript was written and finalized by Nancy Levinger and Sam Miller.

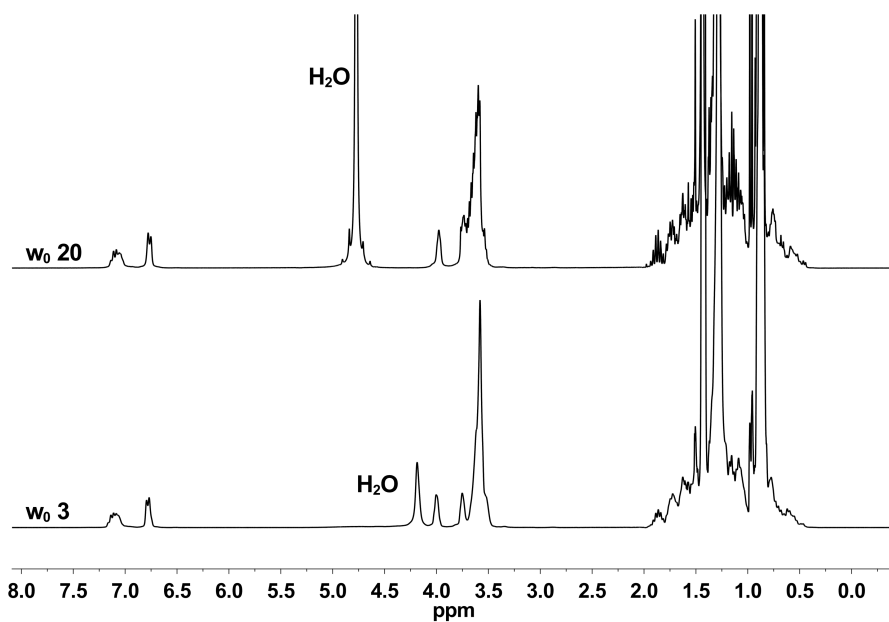


**Figure S3.1:** Stacked  $^1\text{H}$  NMR spectra of  $w_0 = 3$  and  $w_0 = 20$  in reverse micelle solutions of igepal CO-520. Solutions were prepared from the 0.2 M NaF (pH 6.9) and 0.3 M igepal CO-520 solution in cyclohexane.

## APPENDIX 4: CHARACTERIZING NOVEL SURFACTANTS

**Attribution and Description of Project Origin:** Preliminary determination of Krafft temperature was conducted by David Osborne of Arcutis Therapeutics. Dry samples of ceteth-10-phosphate and dicetylphosphate and funding for project related expenses were provided by David Osborne and his research division. Data collection on the DLS instrument was conducted and analyzed by Samantha Miller under the guidance of Nancy Levinger. Supporting experiments on the DLS instrument to investigate new temperature ranges were done by Mia Halliday.

## APPENDIX 5: GUIDE TO ABBREVIATIONS

NMR- Nuclear magnetic resonance spectroscopy

EXSY NMR- Exchange spectroscopy nuclear magnetic resonance

NOESY NMR- Nuclear Overhauser effect nuclear magnetic resonance

WEX NMR- Water exchange nuclear magnetic resonance

RM- Reverse micelle

AOT- Aerosol organic trapper (common name), or bis-(2-ethylhexyl) sulfosuccinate sodium salt

DLS- Dynamic light scattering

DSC- Differential scanning calorimetry

CTAB- Cetyltrimethylammonium bromide

CMC- Critical micelle concentration

ITC- Isothermal titration calorimetry